Title

Modified Gaussian Renormalized Fluctuation Theory for Electrolytes at Interfaces

Author

Agrawal, Nikhil R.

Publication Date

2024

Peer reviewed|Thesis/dissertation

Modified Gaussian Renormalized Fluctuation Theory for Electrolytes at Interfaces

By

Nikhil R. Agrawal

A dissertation submitted in partial satisfaction of the

requirements for the degree of

Doctor of Philosophy

in

Chemical Engineering

in the

Graduate Division

of the

University of California, Berkeley

Committee in charge:

Professor Rui Wang, Chair
Professor David T. Limmer
Professor Kranthi K. Mandadapu
Professor Clayton J. Radke

Summer 2024

Modified Gaussian Renormalized Fluctuation Theory for Electrolytes at Interfaces

Abstract

Modified Gaussian Renormalized Fluctuation Theory for Electrolytes at Interfaces

By

Nikhil R. Agrawal

Doctor of Philosophy in Chemical Engineering

University of California, Berkeley

Professor Rui Wang, Chair

One outstanding challenge in the physical chemistry of electrolyte solutions is to quantitatively describe the structure and properties of electrical double layers in systems with high surface charges, high ion valencies, high salt concentrations, and spatially varying dielectric permittivity. The classical mean-field Poisson-Boltzmann (PB) theory is physically intuitive and numerically soluble, however, its usage is limited to dilute monovalent salts at low surface charges as it does not account for three essential factors: ion-ion correlations, dielectric variation, and excluded volumes of ions and solvent molecules. A theory addressing these limitations is crucial for understanding many fundamental electrolyte solution phenomena, such as the vapor-liquid interface in ionic fluids, overcharging and charge inversion, repulsion between oppositely charged surfaces, and attraction between like-charged surfaces, among many others. In this thesis, a new electrolyte solution theory is developed that addresses the limitations of the mean-field Poisson-Boltzmann (PB) theory. The validity of this theory is demonstrated by explaining the aforementioned phenomena in a self-consistent and rigorous manner.

Going beyond mean-field PB to accurately quantify spatially varying ion-ion correlations, dielectric permittivity, and excluded volume effect is a numerically implausible task. The reason is the need to resolve the electrostatic correlation function at two very different length scales, one associated with ion size (short-range) and the other associated with interface thickness (long-range). Contemporary ways to solve this dual-length scale problem are using a phenomenological approach, a non-local density functional-based approach, or Integral equation-based theories. While phenomenological models have often failed to satisfy well-established Debye-Hückel theory in the bulk, the integral equation-based approach, and non-local density functional-based approach use unphysical approximations and non-generalizable weighting functions to reduce the computational cost of this dual-length scale problem. Here, we present a self-consistent field theory entitled, "Modified Gaussian Renormalized Fluctuation Theory" to overcome the limitations of existing beyond mean-field PB

approaches. The main contribution of this work is the introduction of a self-consistent scheme to decompose the correlation function into a short-range contribution associated with the local electrostatic environment and a long-range contribution accounting for the spatially varying ionic strength and dielectric permittivity. This decomposition step makes the dual-length scale problem numerically tractable in a thermodynamically rigorous way. We also account for the excluded volume effect of ions and solvent molecules by including the incompressibility constraint in the partition function. Additionally, we demonstrate the complete numerical method for solving the resultant non-linear equations. We introduce a novel Sturm-Liouville theory-inspired approach that analytically handles the Dirac delta function in the differential equation of electrostatic correlation function, allowing us to employ highly efficient spectral methods.

For the problem of vapor-liquid interface in ionic fluids, in the case of symmetric salts, both the coexistence curve and the interfacial tension predicted by our theory are in quantitative agreement with simulation data reported in the literature. We also provide the first theoretical prediction of interfacial structure for asymmetric salt, highlighting the importance of capturing local charge separation. Next, we elucidate the underlying dependence of overcharging and charge inversion on the electrostatic coupling by varying surface charge, counterion valency, salt concentration and dielectric contrast. Consistent with simulations, three characteristic regimes corresponding to weak, moderate, and strong coupling are identified. Important features like the inversion of zeta potential, crowding, and ionic layering at the surface are successfully captured. For weak coupling, there is no overcharging. In the moderate coupling regime, overcharging increases with surface charge. Finally, in the strong coupling regime, ionic crowding and saturation in overcharging are observed. Our theory predicts non-monotonic dependence of charge inversion on multivalent salt concentration as well as the addition of monovalent salt, in quantitative agreement with experiments.

We also capture the counter-intuitive phenomena of like-charge attraction and opposite-charge repulsion in multivalent salt solutions and explain their relationship with overcharging. Our theory predicts that the strength of opposite-charge repulsion monotonically increases with salt concentration whereas the strength of like-charge attraction behaves non-monotonically. The addition of monovalent salt to a multivalent salt solution is found to decrease the strength of both opposite-charge repulsion and like-charge attraction. Akin to overcharging, opposite-charge repulsion and like-charge attractions are also outcomes of the heightened ion-ion correlation effect in multivalent ions and there is no inherent causal relationship between overcharging and these two phenomena. Our theoretical predictions for the double layer forces are consistent with the observations reported in experiments and simulations. The thesis concludes by discussing the limitations of our theory and future avenues of research.

To my mother and father,
Rama and Rameshwar Agrawal

Contents

List of Figures

List of Symbols

$\Delta P_{\text{channel}}$ Pressure difference across channel

$\Delta\psi_{\text{G}}$ Galvani electrostatic Potential difference

$\delta_{v,l}$ Interfacial width in vapor(v) and liquid phase (l)

ϵ Scaled dielectric permittivity

η Incompressibility field

γ Interfacial tension

γ^* Scaled interfacial tension

$\hat{c}_{\pm,s}$ Particle density operators for cations (+), anions (−), and solvent (s)

$\hat{G}$ Hankel transform of electrostatic or ion-ion correlation function

$\hat{G}_{\text{O}}$ Hankel transform of free-space electrostatic or ion-ion correlation function

$\hat{G}_{\text{S}}$ Hankel transform of short-range electrostatic or ion-ion correlation function

κ Debye-Hückel wave vector

$\lambda_{\pm,s}$ Fugacities for cations (+), anions (−), and solvent (s)

$\mathcal{H}$ Electrostatic Hamiltonian

$\mathcal{W}$ Grand free energy

μ_{ep} Electrophoretic mobility

$\mu_{\pm,s}$ Electrochemical potentials of cations (+), anions (−), and solvent (s)

ν Bulk viscosity of water

Ω Grand canonical partition function

Ω_{ref} Reference grand canonical partition function

ϕ	Instantaneous Electrostatic Potential
ψ	Mean electrostatic Potential
ψ_ζ	Zeta Potential
ρ	Charge density
ρ_{fix}	Fixed charge density
σ	Surface charge density
σ_{app}	Apparent charge density
σ_{ov}	Degree of overcharging
τ	Charging variable
ε	Dielectric permittivity
ε_{P}	Dielectric permittivity of plate
ε_{S}	Dielectric permittivity of solvent
Ξ	Electrostatic coupling parameter
$a_\pm$	Cation (+) and anion (−) born radius
C	Coulomb operator
c^*	Scaled concentration
$c_{\pm,s}$	Concentrations of cations (+), anions (−), and solvent (s)
D	Separation distance between two charged plates
e	Electronic/elementary charge
G	Electrostatic or ion-ion correlation function
G_{b}	Electrostatic or ion-ion correlation function in the bulk
G_{L}	Long-range electrostatic or ion-ion correlation function
G_{O}	Free-space electrostatic or ion-ion correlation function
G_{S}	Short-range electrostatic or ion-ion correlation function
H	Nanochannel height

$h_{\pm}$	Charge distribution function for cation (+) and anion (−)
I	Ionic strength
k	Boltzmann constant
l_{b}	Bjerrum length
P	Disjoining pressure between two charged plates
P_{b}	Bulk osmotic pressure
$q_{\pm}$	Cation (+) and anion (−) valency
r	position vector
S	Streaming current
T	Temperature
T_{c}	Critical temperature
u	Fluid velocity
u_{∞}	Fluid velocity far away from colloidal particle
$u_{\pm,\mathrm{S}}$	Short range self energy of cation (+) and anion (−)
$u_{\pm}$	Self energy of cation (+) and anion (−)
$v_{\pm,s}$	Excluded volumes of cations (+), anions (−), and solvent (s)
w	Nanochannel width

Acknowledgments

First and foremost, I would like to thank my advisor, Rui Wang, for giving me the best possible project any graduate student could hope for. The amount I have learned in the last six years has surpassed all expectations I had before joining the Ph.D. program. I am deeply grateful for his continuous guidance and support, especially for the flexibility he has shown over the years in accommodating the strong differences we have in terms of our personalities and perspectives on handling research problems, as well as other challenges throughout my Ph.D. After Rui, if someone has made the biggest contribution to this thesis, it is Prof. Carlo Carraro. Carlo noticed the similarities between the differential equation for our electrostatic correlation function and Green's Function of the Sturm-Liouville Equation, which helped us develop a highly efficient numerical method to solve our theory. This new method played a key role in getting the results that shape this thesis.

I am also immensely grateful to my dissertation committee members, Prof. Kranthi K. Mandadapu, Prof. David T. Limmer, and Prof. Clayton Radke for their insightful comments on my work throughout my Ph.D. Their courses on transport phenomena, statistical mechanics, and interfacial science have made invaluable contribution towards development of this thesis. The value of my countless discussions with Kranthi cannot be overstated. I am deeply thankful to David for organizing the Pitzer Center seminar series and the Berkeley Statistical Mechanics meeting. The research talks at these two forums are by far the best seminars I have ever attended at Berkeley or anywhere else. I will always consider myself fortunate to have had the opportunity to learn from Prof. Radke's vast experience.

I am also thankful for the fellowship of the Wang group members: Chao Duan, Chao Fang, Zachary Lipel, Luofu Liu, Takashi Yokokura, Ian Woolsey, and Ravtej Kaur. Each one of them, in one way or another, is both a better human being and a better scientist than I am, and their influence has helped me grow in both areas. A big thanks to the Mandadapu group as well—Yannick Omar, Ahmad Alkadri, Clay Batton, Muhammad Hasyim, and Cory Hargus—for helping out with numerous issues throughout my work in the Pitzer Center. A special shout-out to Dimitrios Fraggedakis; during my final years at Berkeley, I knew I could rely on his counsel for both academic and non-academic issues.

During my Ph.D., I also had the opportunity to work at the Flatiron Institute in New York and Lawrence Livermore National Laboratory. I am grateful to Dr. Adam R. Lamson and Dr. Amit Samanta for giving me the chance to learn something new and for providing a much-needed break from my Ph.D. project. It was at the Flatiron Institute's Biophysical Modeling Summer School where I was introduced to *Dedalus*, the spectral methods solver on which the code for our theory is based. A big thanks to Dr. Keaton J. Burns of MIT, Dr. Adam R. Lamson, Vicente Gómez Herrera of the Flatiron Institute, and Dr. Brato Chakrabarti of Flatiron and ICTS, Bengaluru, for their assistance in setting up our differential equations in *Dedalus*.

I would also like to acknowledge the support and guidance of Prof. Bryan McCloskey, Prof. Karthik Shekhar, Prof. Nitash Balsara, and Prof. Aditi Krishnapriyan. Many thanks to Carlet Altamirano, Polly Ng, and the personnel at the Berkeley International Office for

their administrative help throughout my stay at Berkeley. Carlet's constant support made my life much easier as I navigated the Ph.D. program as the first student in the Wang group.

Last but not least, I would like to thank my friends and family. I could never thank my parents enough for helping me become the person I am today. Being the youngest of all my cousins, I am especially grateful for the lessons they imparted from their successes and failures throughout my life. In particular, I want to thank my cousins in the Bay Area: Purva and Aman Agrawal, and Aditi and Amar Ojha. Having family members nearby made life easier and more comfortable in a new country, especially when I broke my ankle. I would also like to acknowledge the friendships I made along the way: Josie Hendrix, Kartavya Sharma, Yannick, Ahmad, Dimitrios, George Makrygiorgos, Tzu-Yang Huang, and Gnocchi (Josie's dog). Finally, a big thanks to my friends in India and elsewhere, Ameya Dubey, Mihir Dhalia, Akash Singh, Siddhartha Pradeep, Swapnil Sharma and Mayank Tanwar, your support and companionship have made this journey memorable and fulfilling.

Chapter 1

Introduction and Overview

The thermodynamic behavior of ions near an interface determines structural and dynamic properties of a wide range of molecular systems, including but not limited to electrochemistry[1], colloidal science[2], soft matter[3], and biophysics[4]. This interface, referred to as the electrical double layer, plays a key role in deciding the rate of transport of ions and redox reactions in electrochemical devices like batteries and supercapacitors[5–7]. In colloidal science, understanding the nature of electrostatic forces between two surfaces is crucial to explain self-assembly of particles[8, 9], cement formation[10], papermaking[11], food processing[12], and surface patterning[13]. Meanwhile, in soft matter and biophysics, the identity and amount of ions in the environment determine the morphology of polyelectrolyte brushes[14, 15], protein stability and assembly[16–21], as well as transport through biological channels[22–26]. Thus, discerning the underlying physics behind the equilibrium and non-equilibrium characteristics of electrical double layers is crucial for designing modern devices and processes across scientific domains.

The evolution of position and momentum of ions inside an electrical double layer is governed by physical and chemical forces active in the system. Chemical forces depend on the identity of ions and solvent molecules and include factors like hydrophobicity and polarizability. On the other hand, physical forces are universal and include coulombic interactions between a pair of ions or an ion and surface charges or hardsphere interactions between ions and solvent molecules. The importance of these forces in the system is decided by the temperature, for instance, if the temperature is very high the ions can simply drift away from each other with minimal effect from the coulombic forces. A straightforward way to develop a coarse-grained theoretical model for electrical double layers is to account for these universal physical forces from first principles and then phenomenologically add the contribution of chemical forces. One such theory incorporating only the effect of physical forces is the classical mean-field Poisson-Boltzmann (PB) theory described by the non-dimensionalized equations given below

$$-\nabla \cdot [\epsilon(\mathbf{r})\nabla\psi(\mathbf{r})] = \rho_{\text{fix}}(\mathbf{r}) + q_+c_+(\mathbf{r}) - q_-c_-(\mathbf{r}) \tag{1.1}$$

$$c_\pm(\mathbf{r}) = \lambda_\pm \exp\left[\mp q_\pm \psi(\mathbf{r})\right] \tag{1.2}$$

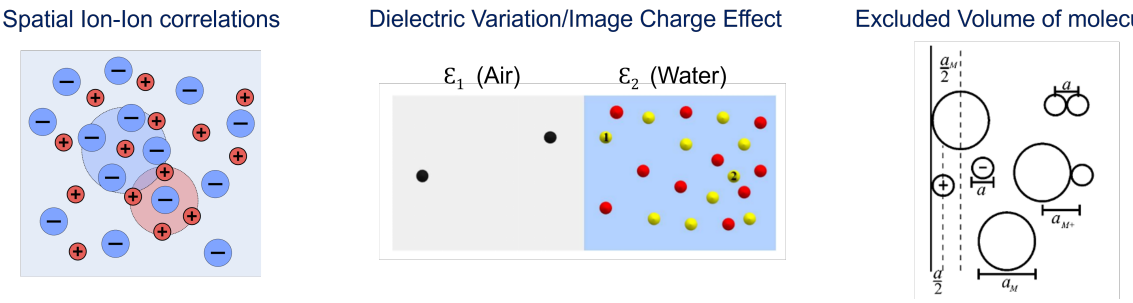

Figure 1.1: Schematics depicting the three missing factors in mean-field Poisson-Boltzmann theory. a) Spatial ion-ion correlations. Image by Roland Mattern. b) Air-water interface depicting dielectric contrast effect. Image adapted with permission from J. Chem. Phys. 144, 134902 (2016). c) Excluded volume interactions between ions, solvent, and surface. Image adapted with permission from J. Phys. Chem. B 108, 22, 7286–7296 (2004).

where ψ in the mean electrostatic potential, ρ_{fix} is the fixed charge density in the system, ϵ is the scaled dielectric permittivity, and $c_{\pm}$, $q_{\pm}$, $\lambda_{\pm}$ are concentrations, valencies and fugacities of the ions, respectively. All these variables, and those defined later in this thesis, are non-dimensionalized unless stated otherwise. The above mean-field PB equations are physically intuitive and numerically solvable[27]. However, the applicability of these equations, whether linearized or not, is limited to systems with low ion valencies, low surface charges, dilute solutions, and uniform dielectric media[4]. This limitation of PB is because of its inability to account for three essential factors: ion-ion correlations, dielectric variation, and excluded volumes of ions and solvent. A schematic depicting these three missing factors is shown in Figure 1.1. Due to the electrostatic Coulomb force, each positive ion tends to be surrounded preferentially by negative ions and vice versa, leading to spatial correlations in the arrangement of ions. These spatial ion-ion correlations are particularly important with multivalent electrolytes and concentrated solutions. The mean-field PB theory incorrectly assumes that the thermal motion completely dominates the electrostatic forces and the ions are essentially randomly positioned around each other without any preference[28]. This theory also fails to capture the effect of dielectric contrast. For instance, in the case of an air-water interface, the right-hand side of Eq. 1.1 becomes identically zero in the air phase, forcing the gradient of ψ to be zero there as well. This zero-gradient condition nullifies any information about the dielectric permittivity of air that could have been incorporated via Gauss's Law at the surface. Furthermore, PB does not account for excluded volumes of molecules leading to an infinite accumulation of ions in the double layer. The problem of capturing the above missing factors becomes even more challenging because the effects of ion-ion correlations, dielectric permittivity, and excluded volumes are spatially varying within the double layer. Unlike bulk solutions, where the structure is completely isotropic, the interface can be highly anisotropic. The goal of this thesis is to develop and demonstrate a new coarse-grained theory for electrical double layers that can account for the missing

physics in mean-field PB in a self-consistent and rigorous manner. Such a theory is critical to understanding many fundamental electrolyte solution phenomena such as vapor-liquid interface in ionic fluids[29], overcharging and charge inversion[30], repulsion between oppositely charged surfaces[31, 32], an attraction between like-charged surfaces[33], and polyelectrolyte swelling and relaxation[15], among many others[4]. Self-consistency in a theory is desirable to capture all these phenomena in a single framework.

Over the years, numerous beyond mean-field PB theories have been developed[34–62]. We will discuss some of the most significant ones here. One of the first attempts to capture electrostatic correlations and excluded volume effect was to use the Ornstein-Zernike (OZ) equation as in Integral equation-based theories (IETs)[34–36, 42, 43]. Depending upon the system, different closures are used to calculate the correlation functions, the most common models use hypernetted-chain closure (HNC) and the mean-spherical approximation (MSA) closure. A major issue with IETs is that the complete solution of the integral equations in the inhomogeneous interface is numerically intractable. Hence, to solve the double layer problem, the functional form of the ion-ion correlation in the inhomogeneous interface is often approximated to be the same as in the bulk. Such local density approximations can lead to physically unrealistic solutions[54, 63]. Furthermore, as will be discussed in detail later in this thesis, IETs have failed to capture certain key ion correlation-induced phenomena[64]. Another approach that uses the OZ equation to calculate the electrostatic correlation function is the classical density functional theory (cDFT) developed by Gillespie et al.[54, 57]. However, this approach relies on perturbing the free energy around a chosen reference ion concentration profile to calculate the free energy of the interface. These reference concentration profiles are determined using density weighting functions that are tailored to a specific system, reducing the generalizability of the method. Such weighting functions also do not provide a physically intuitive description of the electrical double layer[63, 65]. Moreover, there does not exist any OZ equation-based formalism that can capture the effect of continuously varying dielectric permittivity on the structure of a double layer, the best these approaches can do is to capture the effect of dielectric contrast between two mediums of uniform dielectric permittivity[66].

Shklovskii and coworkers developed the Strongly Correlated Liquid (SCL) theory to capture the effect of ion-ion correlations near a charged surface[44, 67]. Inspired by one-component plasma physics, Perel and Shklovskii assumed the presence of a two-dimensional condensed layer of counterions on the charged surface existing in the form of a Wigner crystal (WC) lattice. The WC lattice at the surface was connected to the outside diffused layer described by mean-field PB[68]. However, the WC lattice picture is valid only in the zero-temperature limit or the so-called infinite electrostatic coupling limit. The electrostatic coupling here is defined as the relative strength of coulombic forces to the thermal forces. Furthermore, SCL only accounts for ion-ion correlations at the surface. The mean-field PB level description away from the surface does not allow SCL to capture the spatially varying ion correlation and excluded volume effect in the diffuse layer and the bulk.

Bazant and coworkers[53, 69] constructed a phenomenological free energy expression by writing the correlation contribution in terms of gradients of electrostatic potential and an

associated correlation length parameter. Recently, Gupta et al.[50] added a screening potential to the Boltzmann factor to account for ion correlations. This screening potential was also expressed in terms of the electrostatic potential gradient without any phenomenological parameter. For the models of Bazant et al.[53, 69], and Gupta et al.[50], although excluded volume effects have been included, the gradient of electrostatic potential vanishes in bulk and thus these theories were unable to capture any correlation contribution to the bulk free energy. Hence, like SCL theory these two theories also cannot recapture the Debye-Hückel theory in the bulk which is known to be exact in the weak coupling limit. Since the interface and the bulk are in equilibrium, the incorrect description of the bulk leads to an inaccurate description of the interface, and these theories fail to capture key characteristics of many ion-correlation induced phenomena.

A number of field theories have also been developed to address the shortcomings of mean-field PB[52, 70–74], the foundational work being done by Netz and Orland [38–41]. The first step in the derivation of these theories is to write the grand canonical partition function of the surface plus electrolyte solution using the electrostatic Hamiltonian. This Hamiltonian is written in terms of the interaction between two particle density fields via the coulomb operator. In the next step, the interaction term between the two-particle density fields is converted into the interaction between an electrostatic potential field and one particle density field using the Hubbard-Stratonovich transformation. The final step of estimating the partition function can be done in two ways, one of them being a perturbative approach which involves performing a loop expansion around the saddle point[39]. This saddle point of the partition function essentially gives the mean-field PB theory. The second way is a variational approach where the partition function is bounded using the Gibbs-Feynman-Bogoliubov inequality and a chosen reference state[41]. This reference state is often assumed to be the one in which the instantaneous electrostatic potential, whose mean is $\psi(\boldsymbol{r})$, is Gaussian distributed. Such a variational description is hence often referred to as the "Gaussian fluctuation theory" for electrolyte solutions. The word "fluctuation" here represents the fluctuations in the electrostatic potential caused by the constant motion of the mobile ions as a result of coulombic and thermal forces. These Gaussian fluctuations are mathematically quantified by the correlation function $G(\boldsymbol{r}, \boldsymbol{r'})$. This G, from an equivalent particle perspective, accounts for the spatially varying ion-ion correlation and dielectric variation in the system. A major advantage of such field theory-based description is it makes it straightforward to incorporate electrolyte solution physics into other field-theoretical formulations, such as self-consistent field theory (SCFT) for polymers or the Poisson-Nernst-Planck equation (PNP) for electrokinetic flows.

Although thermodynamically rigorous and self-consistent, all the above field-theoretic formulations for electrolyte solutions use an unphysical point-charge model for ions which overestimates the ion-ion correlation effect. To remedy this, the finite spread of ionic charge was systematically included in these field theories by Z.-G. Wang[75]. The finite charge spread model also eliminates divergence issues from the self-energy term of the ions, resulting in the "renormalization" of the fluctuation contribution to the free energy. Therefore, the theory was titled the Gaussian Renormalized Fluctuation theory. However, the inclusion of

the finite-charge spread introduces an additional complexity of dealing with the dual-length scale problem associated with the numerical calculation of the ion-ion correlation contribution to the free energy. The electrostatic correlation function G now needs to be evaluated at both the length scale of the interface as well as the length scale of the ion. This thesis entitled, "Modified Gaussian Renormalized Fluctuation Theory for Electrolytes at Interfaces" builds upon Z.-G. Wang's work and solves this dual-length scale problem by introducing a self-consistent scheme to decompose the correlation function into a short-range contribution associated with the local electrostatic environment and a long-range contribution accounting for the spatially varying ionic strength and dielectric permittivity. Furthermore, we account for the excluded volume effect of ions and solvent molecules by including the incompressibility constraint in the partition function. In the next chapter, the complete derivation of the Modified Gaussian Renormalized Fluctuation Theory with a particular focus on the decomposition scheme for the electrostatic correlation function is presented. We also discuss the complete numerical method for solving the resultant non-linear equations, alongside a novel Sturm-Liouville theory-inspired approach for calculating the electrostatic correlation function. This method analytically handles the Dirac delta function in the differential equation of G, allowing us to employ highly efficient spectral methods.

To demonstrate the validity and understand the scope and limitations of our theory several fundamental ion correlation-induced phenomena are studied in this thesis. In Chapter 3, we study the classical problem of vapor-liquid interface in ionic fluids. Analogous to vapor-liquid phase equilibrium in real gases, ionic salts dissolved in a solvent can also undergo phase separation into a high ion density 'liquid' and a low density 'vapor' phase because of coulombic interactions[29, 76–79]. Despite the progress in explaining the bulk thermodynamics of this phenomena, the interfacial behavior remain less addressed. Bresme and coworkers[80–82] performed molecular simulations to study this interface, including the density profile and interfacial tension. However, applying simulation methods away from the critical temperature is difficult due to the very low density of the vapor phase. A coarse-grained theory like ours provides valuable insights into these systems.

In Chapter 4, we model the long-standing challenge of overcharging and charge inversion in electrical double layers with multivalent salts. Overcharging is the phenomenon of over-accumulation of counterions in the double layer which may lead to a reversal in the sign of electrophoretic mobility of colloidal particles or in the direction of ionic current in electro-osmotic flows [30, 83]. This reversal in the sign of diffuse plane potential is usually known as charge inversion. In multivalent salt solutions, this excess accumulation is made feasible by ion-ion correlations[31]. Here, using the Modified Gaussian Renormalized Fluctuation Theory, the underlying dependence of overcharging on the electrostatic coupling is elucidated by varying surface charge, counterion valency, salt concentration, and dielectric contrast. Theoretical predictions of double layer structure are compared with results from molecular simulations, and experimental electrophoretic mobility and streaming current measurements.

Another very important aspect to study is the electrostatic force between two charged surfaces mediated by a salt solution. In the classical Derjaguin-Landau-Verwey-Overbeek (DLVO) framework[2], this electrostatic force is described by the mean-field PB theory.

Consistent with physical intuition, mean-field PB predicts a repulsive force between two like-charged surfaces and an attractive force between two oppositely charged surfaces at all separation distances. However, numerous experimental and simulation studies have reported attraction between like-charged surfaces[33, 84–90] and repulsion between oppositely charged surfaces[31, 32, 91–98] in the presence of multivalent salts. The origin of these counter-intuitive phenomena is the electrostatic correlation between ions[32, 87]. In Chapters 5 and 6, we investigate the phenomena of repulsion between two oppositely charged surfaces and attraction between like-charged surfaces, respectively, and discuss their relationship with overcharging. The effects of spatially varying ion correlations on the structure of overlapping double layers and their free energy are self-consistently accounted for. We particularly focus on the strength of repulsive and attractive force as a function of salt concentration, as these characteristics are closely related to the phenomena of reentrant condensation in colloids [85, 99, 100]. Theoretical predictions are validated against data from Monte-Carlo simulations with only electrostatic and hard-sphere interactions.

The phenomena of vapor-liquid coexistence, overcharging, opposite-charge repulsion, and like-charge attraction were chosen, as these are predominantly dictated by electrostatic and excluded volume interactions between ions and solvent molecules. Hence, they were ideal problems to test our theory. However, like any coarse-grained model, our theory, besides having its advantages, also has its drawbacks. In the final chapter, we will discuss the advances made in electrolyte solution theory through this thesis, as well as the limitations encountered in the application of our model to various scenarios. We will explore potential avenues for future research, addressing the need for refinement and expansion of our theoretical framework. Additionally, we will reflect on the broader implications of our findings within the fields of soft matter and biophysics and propose directions for future work.

Chapter 2

Modified Gaussian Renormalized Fluctuation Theory

2.1 Introduction

In this chapter, we derive the Modified Gaussian Renormalized Fluctuation Theory to describe the behavior of electrolyte solutions with spatially varying ion-ion correlations, dielectric permittivity, and excluded volume effect. The system consists of an immobile fixed charge density $\rho_{\text{fix}}(\boldsymbol{r})$, and mobile cations and anions with valencies q_+ and q_-, respectively. The fixed charges and the mobile ions exist together in a medium with the dielectric function given by $\varepsilon(\boldsymbol{r})$. Instead of using the point-charge model to describe the ions, we employ a more realistic description by accounting for finite charge spread by using a short-range charge distribution function $h_\pm(\boldsymbol{r}-\boldsymbol{r}_i)$ for the i$^{\text{th}}$ ion centered at $\boldsymbol{r}_i$. The introduction of finite charge distribution over the point-charge model avoids overestimation of the ion-ion correlation effect. Compared to the earlier work from Z.-G. Wang and coworkers[75, 101, 102], there are two major additions incorporated in this "modified" theory. First, the excluded volumes of the ions and solvent molecules, $v_\pm$ and v_{s}, are systematically included in the grand canonical partition function to avoid the over-accumulation of ions in the interface. Second, the electrostatic correlation function is decoupled into a short-range contribution associated with the local electrostatic environment and a long-range contribution accounting for the spatially varying ionic strength and dielectric permittivity. In the following sections, we first present the derivation of a set of self-consistent equations for the dimensionless electrostatic potential ψ, ion concentration $c_\pm$, self-energy of ions $u_\pm$, correlation function G, and the incompressibility field η. Next, we simplify these equations for the case of homogeneous bulk solution as well as the inhomogeneous interface. To solve for the correlation function in the interface, we then introduce the above-mentioned decoupling procedure. Finally, we present the numerical method to solve these equations for the case of planar symmetric interfaces where the electrostatic potential and ion concentrations only vary in one direction. In principle, this numerical method is also applicable to symmetrically charged cylindrical and

spherical surfaces. Furthermore, though the theory and numerical methods are illustrated by using a single salt as an example, they can be easily generalized to solutions containing multiple salts, i.e., electrolyte mixtures.

2.2 Derivation of the self-consistent field equations

We start the derivation by defining the electrostatic Hamiltonian $\mathcal{H}$ for the above mentioned electrolyte solution system as

$$\mathcal{H} = \frac{e^2}{2} \int d\boldsymbol{r} d\boldsymbol{r'} \rho(\boldsymbol{r}) C(\boldsymbol{r}, \boldsymbol{r'}) \rho(\boldsymbol{r'}) \tag{2.1}$$

where $C(\boldsymbol{r}, \boldsymbol{r'})$ is the Coulomb operator given by

$$-\nabla.[\epsilon(\boldsymbol{r}) \nabla C(\boldsymbol{r}, \boldsymbol{r'})] = \delta(\boldsymbol{r} - \boldsymbol{r'}) \tag{2.2}$$

$\epsilon(\boldsymbol{r}) = kT\varepsilon_0 \varepsilon(\boldsymbol{r})/e^2$ is the scaled permittivity with ε_0 the vacuum permittivity and e as the elementary charge. The total charge density $\rho(\boldsymbol{r})$ at any position $\boldsymbol{r}$ in the system is given by

$$\rho(\boldsymbol{r}) = \rho_{\text{fix}}(\boldsymbol{r}) + \int d\boldsymbol{r'} \left[q_+ h_+(\boldsymbol{r} - \boldsymbol{r'}) \hat{c}_+(\boldsymbol{r'}) - q_- h_-(\boldsymbol{r} - \boldsymbol{r'}) \hat{c}_-(\boldsymbol{r'}) \right] \tag{2.3}$$

where $\hat{c}_\pm(\boldsymbol{r}) = \sum_{i=1}^{n_\pm} \delta(\boldsymbol{r} - \boldsymbol{r}_i)$ is the particle density operator for the ions. The grand canonical partition function Ω for the system can then be written as

$$\begin{aligned} \Omega = \sum_{n_+=0}^{\infty} \sum_{n_-=0}^{\infty} \sum_{n_\text{s}=0}^{\infty} \frac{\mathrm{e}^{\mu_+ n_+} \mathrm{e}^{\mu_- n_-} \mathrm{e}^{\mu_\text{s} n_\text{s}}}{n_+! n_-! n_\text{s}! v_+^{n_+} v_-^{n_-} v_\text{s}^{n_\text{s}}} \int \prod_{i=1}^{n_+} d\boldsymbol{r}_i \prod_{j=1}^{n_-} d\boldsymbol{r}_j \prod_{k=1}^{n_\text{s}} d\boldsymbol{r}_k \\ \times \prod_{\boldsymbol{r}} \delta \left[1 - v_+ \hat{c}_+(\mathbf{r}) - v_- \hat{c}_-(\mathbf{r}) - v_\text{s} \hat{c}_\text{s}(\mathbf{r}) \right] \exp(-\beta \mathcal{H}) \end{aligned} \tag{2.4}$$

where $\mu_\pm$ and μ_s denote the chemical potentials of the ions and solvent, respectively. The functional delta is introduced to impose the local incompressibility constraint. As will become evident in the following steps, the choice of grand canonical partition function is for mathematical convenience. Next, we apply the Hubbard-Stratonovich transformation and identity transformation on Equation 2.4. This introduces a electrostatic potential field variable $\phi(\boldsymbol{r})$, coupled with $\rho(\boldsymbol{r})$ and a field variable $\xi(\boldsymbol{r})$ to enforce the incompressibility constraint, which yields

$$\Omega = \frac{1}{Z_0} \int D\phi \int D\xi \exp\left\{ -L[\phi, \xi] \right\} \tag{2.5}$$

where $D\phi$ and $D\xi$ represent functional integrals over field $\phi(\boldsymbol{r})$ and $\xi(\boldsymbol{r})$. The "action" L above is of the following form

$$L \coloneqq \int d\boldsymbol{r} \left[\frac{1}{2} \epsilon (\nabla \phi)^2 + i \rho_{\text{fix}} \phi - \lambda_+ \mathrm{e}^{-i\hat{h}_+ \phi - i v_+ \xi} - \lambda_- \mathrm{e}^{i\hat{h}_- \phi - i v_- \xi} - \lambda_\text{s} e^{-i v_\text{s} \xi} - i\xi \right] \tag{2.6}$$

with $\lambda_\pm = \mathrm{e}^{\mu_\pm}/v_\pm$ and $\lambda_\mathrm{s} = \mathrm{e}^{\mu_\mathrm{s}}/v_\mathrm{s}$ as the fugacity of the ions and solvent, respectively. The short-hand notation $\hat{h}_\pm\phi$ stands for local spatial averaging of ϕ by the charge distribution function: $\hat{h}_\pm\phi = \int d\boldsymbol{r}' h_\pm(\boldsymbol{r}'-\boldsymbol{r})\phi(\boldsymbol{r}')$. Z_0 in Equation 2.5 is the normalizing factor expressed as

$$Z_0 = \int D\phi \exp\left[-\frac{1}{2}\int d\boldsymbol{r}\epsilon(\nabla\phi)^2\right] = [\det \boldsymbol{C}]^{1/2} \tag{2.7}$$

The integral over ξ in Equation 2.5 is solved using the saddle point approximation. A new variable $\eta = i\xi^*$, with ξ^* denoting the saddle point value of ξ, is introduced. Following expression for the incompressibility field η can be derived from the saddle point condition of $\frac{\partial L}{\partial \xi} = 0$

$$v_+\lambda_+\mathrm{e}^{-i\hat{h}_+\phi - v_+\eta} + v_-\lambda_-\mathrm{e}^{i\hat{h}_-\phi - v_-\eta} + v_\mathrm{s}\lambda_\mathrm{s}e^{-v_\mathrm{s}\eta} - 1 = 0 \tag{2.8}$$

The partition function Ω can then be simplified to

$$\Omega = \frac{1}{Z_0}\int D\phi \exp\left\{-\int d\boldsymbol{r}\left[\frac{1}{2}\epsilon(\nabla\phi)^2 + i\rho_\mathrm{fix}\phi - \lambda_+\mathrm{e}^{-i\hat{h}_+\phi - v_+\eta} - \lambda_-\mathrm{e}^{i\hat{h}_-\phi - v_-\eta} - \lambda_\mathrm{s}e^{-v_\mathrm{s}\eta} - \eta\right]\right\} \tag{2.9}$$

The action L is now a functional of ϕ only. To capture the fluctuation of the electrostatic potential, a variational procedure to calculate r.h.s. of Equation 2.9 is carried out using the Gibbs-Feynman-Bogoliubov bound for the grand free energy, W. Using this bound, W can be evaluated by

$$W = -\ln\Omega \leq -\ln\Omega_\mathrm{ref} + \langle L[\phi] - L_\mathrm{ref}[\phi]\rangle_\mathrm{ref} \tag{2.10}$$

$\langle\cdots\rangle_\mathrm{ref}$ represents the average taken in the reference ensemble. The reference action L_ref is chosen to be of the Gaussian form centered around the mean potential $-i\psi$,

$$L_\mathrm{ref} \coloneqq \frac{1}{2}\int d\boldsymbol{r}d\boldsymbol{r}'[\phi(\boldsymbol{r}) + i\psi(\boldsymbol{r})]G^{-1}(\boldsymbol{r},\boldsymbol{r}')[\phi(\boldsymbol{r}') + i\psi(\boldsymbol{r}')] \tag{2.11}$$

where G^{-1} is the inverse of the function G, which describes the correlation between two point charges located at $\boldsymbol{r}$ and $\boldsymbol{r}'$. It is worth mentioning that by taking the saddle-point approximation for ϕ instead of the variational calculation shown above, the steric PB theory derived by Borukhov et al.[103] is recovered. Moreover, if the functional delta in Equation 2.4 is also removed, then we get back to the standard mean-field PB theory without the ion-ion correlation and excluded volume effect of molecules.

Gaussian reference action leads to analytical expressions for all the terms on the r.h.s. of Equation 2.10. We refer interested readers to the relevant literature for the detailed derivation [41, 75, 104]. The lower bound of the free energy is obtained by minimizing W with respect to both the mean potential ψ and the correlation function G, which results in the following two equations

$$-\nabla\cdot[\epsilon(\boldsymbol{r})\nabla\psi(\boldsymbol{r})] = \rho_\mathrm{fix}(\boldsymbol{r}) + q_+\lambda_+\mathrm{e}^{-q_+\psi - u_+ - v_+\eta} - q_-\lambda_-\mathrm{e}^{q_-\psi - u_- - v_-\eta} \tag{2.12}$$

$$-\nabla_{\boldsymbol{r}'}.[\epsilon(\boldsymbol{r}')\nabla_{\boldsymbol{r}'}G(\boldsymbol{r}',\boldsymbol{r}'')] + 2I(\boldsymbol{r}')G(\boldsymbol{r}',\boldsymbol{r}'') = \delta(\boldsymbol{r}'-\boldsymbol{r}'') \tag{2.13}$$

where $2I(\boldsymbol{r}') = \left(q_+^2 c_+(\boldsymbol{r}') + q_-^2 c_-(\boldsymbol{r}')\right)$ is the local ionic strength. The expressions for the concentration of cations, anions, and solvent can be calculated by taking the partial derivative of W with respect to the chemical potentials $\mu_{\pm,\mathrm{s}}$ as follows

$$c_\pm(\boldsymbol{r}) = \lambda_\pm \exp\left[\mp q_\pm \psi(\boldsymbol{r}) - u_\pm(\boldsymbol{r}) - v_\pm \eta(\boldsymbol{r})\right] \tag{2.14}$$

$$c_\mathrm{s}(\boldsymbol{r}) = \lambda_s \exp\left[-v_s \eta(\boldsymbol{r})\right] \tag{2.15}$$

$u_\pm$ above denotes the self-energy of cations and anions,

$$u_\pm(\boldsymbol{r}) \coloneqq \frac{1}{2}\int d\boldsymbol{r}' d\boldsymbol{r}'' h_\pm(\boldsymbol{r}'-\boldsymbol{r}) G(\boldsymbol{r}',\boldsymbol{r}'') h_\pm(\boldsymbol{r}''-\boldsymbol{r}) \tag{2.16}$$

The equations for the concentrations of ions and solvent molecules allow us to rewrite the incompressibility condition given by Equation 2.8 as

$$v_+ c_+(\boldsymbol{r}) + v_- c_-(\boldsymbol{r}) + v_\mathrm{s} c_\mathrm{s}(\boldsymbol{r}) = 1 \tag{2.17}$$

The above condition ensures the total volume fraction of ions and solvent molecules is equal to 1. Making use of Equations 2.15 and 2.17, an expression for η can be obtained as

$$\eta(\boldsymbol{r}) = \frac{\mu_\mathrm{s}}{v_\mathrm{s}} - \frac{1}{v_\mathrm{s}}\ln[1 - v_+ c_+(\boldsymbol{r}) - v_- c_-(\boldsymbol{r})] \tag{2.18}$$

Equations 2.12-2.18 are the key equations to perform a self-consistent calculation of the mean electrostatic potential $\psi(\boldsymbol{r})$, the correlation function $G(\boldsymbol{r}',\boldsymbol{r}'')$, the self-energy of ions $u_\pm(\boldsymbol{r})$, the ion concentration $c_\pm(\boldsymbol{r})$ and the incompressibility field $\eta(\boldsymbol{r})$. Particularly, the correlation function describes the interaction between the ion and its ionic atmosphere, which manifests itself in the self-energy of ions appearing in the Boltzmann factor. The self-energy can be spatially varying, which captures the inhomogeneous nature of the ion-ion correlation effect. Based on the variational conditions (Equations 2.12 and 2.13), the equilibrium grand free energy can be calculated using the charging method[102]:

$$\begin{aligned}\mathcal{W} = &\int d\boldsymbol{r}\left[\frac{1}{2}\psi\left(\rho_\mathrm{fix} - q_+c_+ + q_-c_-\right) - c_+ - c_- + \frac{\ln(1-c_+v_+-c_-v_-) - (1-c_+v_+-c_-v_-)}{v_\mathrm{s}}\right] \\ &+\frac{1}{2}\int d\boldsymbol{r}\int d\boldsymbol{r}'\int d\boldsymbol{r}''\int_0^1 d\tau[G(\boldsymbol{r}',\boldsymbol{r}'',\tau) - G(\boldsymbol{r}',\boldsymbol{r}'')]\left[\sum_{i=+,-} q_i^2 c_i h_i(\boldsymbol{r}'-\boldsymbol{r}) h_i(\boldsymbol{r}''-\boldsymbol{r})\right]\end{aligned} \tag{2.19}$$

where the last term in the first line of the r.h.s of the above equation comes from the incompressibility constraint. The second line is the contribution from the fluctuation of the electrostatic field with τ being a "charging" variable. $\tau = 0$ corresponds to the case when

all the ions in the system are neutral and have zero charge and $\tau = 1$ implies that all ions are fully charged to their valencies. The differential equation for $G(\mathbf{r}', \mathbf{r}'', \tau)$ is given by

$$-\nabla_{\mathbf{r}'}.[\epsilon(\mathbf{r}')\nabla_{\mathbf{r}'}G(\mathbf{r}', \mathbf{r}'', \tau)] + 2\tau I(\mathbf{r}')G(\mathbf{r}', \mathbf{r}'', \tau) = \delta(\mathbf{r}' - \mathbf{r}'') \tag{2.20}$$

$G(\mathbf{r}', \mathbf{r}'', \tau = 0)$ represents the free space G without any mobile charged particles and $G(\mathbf{r}', \mathbf{r}'', \tau = 1)$ is the correlation function when all ions are charged, as in Eq. 2.13.

2.3 Bulk thermodynamics

We apply the theory to the bulk solution where the ion distribution, dielectric permittivity, and electrostatic potential are uniform. The chemical potential of ions $\mu_\pm$ is determined from the bulk ion concentration using Equation (2.14)

$$\mu_\pm = \mp q_\pm \psi_\mathrm{b} + u_{\pm,\mathrm{b}} + \ln c_{\pm,\mathrm{b}} v_\pm + v_\pm \eta_\mathrm{b} \tag{2.21}$$

where the subscript b represents the value of the corresponding quantities in the bulk. On the other hand, as solvent molecules are uncharged their chemical potential is simply given by

$$\mu_\mathrm{s} = \ln c_{\mathrm{s,b}} v_\mathrm{s} + v_\mathrm{s} \eta_\mathrm{b} \tag{2.22}$$

To calculate the bulk self-energy $u_{\pm,\mathrm{b}}$ of ions, the bulk correlation function G_b needs to be evaluated. In the homogeneous bulk, Equation (2.13) leads to the following Debye-Hückel (DH) analytical solution for G_b

$$G_\mathrm{b}(\boldsymbol{r'}, \boldsymbol{r''}) = \frac{\mathrm{e}^{-\kappa_\mathrm{b}|\boldsymbol{r'}-\boldsymbol{r''}|}}{4\pi\epsilon_\mathrm{b}|\boldsymbol{r'}-\boldsymbol{r''}|} \tag{2.23}$$

where κ_b and ϵ_b are non dimensional Debye-Hückel screening wave vector and scaled permittivity in the bulk. In this thesis, for mathematical convenience we consider charge distribution function $h_\pm$ to be of the following Gaussian form,

$$h_\pm(\boldsymbol{r} - \boldsymbol{r'}) = \left(\frac{1}{2a_\pm}\right)^{3/2} \exp\left[\frac{-\pi(\boldsymbol{r} - \boldsymbol{r'})^2}{2a_\pm^2}\right] \tag{2.24}$$

Substituting Equations (2.23) and (2.24) into (2.16) leads to the following analytical expression of the bulk self-energy $u_{\pm,\mathrm{b}}$

$$u_{\pm,\mathrm{b}} = \frac{q_\pm^2}{8\pi\epsilon_\mathrm{b} a_\pm} - \frac{q_\pm^2}{8\pi\epsilon_\mathrm{b}}\kappa_\mathrm{b} \exp\left(\frac{(a_\pm\kappa_\mathrm{b})^2}{\pi}\right) \mathrm{erfc}\left(\frac{a_\pm\kappa_\mathrm{b}}{\sqrt{\pi}}\right) \tag{2.25}$$

The first term on the r.h.s is the Born solvation energy and the second term is the contribution from the ion-ion correlation. The above equation also automatically defines the variable $a_\pm$

as the Born radius of the ions. In the point-charge limit the second term in Eq. 2.25 reduces to $-\frac{q_\pm^2\kappa_\mathrm{b}}{8\pi\epsilon_\mathrm{b}}$, which is also ion correlation contribution to chemical potential in the Debye-Hückel limit.

Using the bulk solution conditions in Equation 2.19 we get the following expression for the bulk pressure (osmotic)

$$P_\mathrm{b} = c_{+,\mathrm{b}} + c_{-,\mathrm{b}} + c_{\mathrm{s,b}} + \eta_\mathrm{b} - \frac{1}{2}\int d\boldsymbol{r'}\int d\boldsymbol{r''}\int_0^1 d\tau[G_\mathrm{b}(\boldsymbol{r'},\boldsymbol{r''},\tau) - G_\mathrm{b}(\boldsymbol{r'},\boldsymbol{r''})] \times\left[\sum_{i=+,-} q_i^2 c_{i,\mathrm{b}} h_i(\boldsymbol{r'}-\boldsymbol{r}) h_i(\boldsymbol{r''}-\boldsymbol{r})\right] \tag{2.26}$$

The DH form of G_b is not surprising as the original DH theory is a Gaussian fluctuation level theory and here also in the last section we chose a Gaussian form for the reference action. Besides the addition of the excluded volume effect, the key difference between our theory and the DH theory is the charge distribution function h to avoid overestimation of the ion-ion correlation contribution to the self-energy term. This finite-charge distribution also removes numerical divergence issues from the self-energy term and hence the title of the theory has the phrase "renormalized fluctuation" in it. Additionally, unlike the DH theory which was only derived for the bulk, in the next section we describe how our theory accounts for ion-ion correlations in the interface as well.

2.4 Interfacial thermodynamics

Next, we apply the theory to the interface. The electrochemical potential for the ions in the interface is given by

$$\mu_\pm(\boldsymbol{r}) = \mp q_\pm\psi(\boldsymbol{r}) + u_\pm(\boldsymbol{r}) + \ln c_\pm(\boldsymbol{r})v_\pm + v_\pm\eta(\boldsymbol{r}) \tag{2.27}$$

To solve for the electrostatic potential and ion distribution, spatially varying self-energy $u_\pm(\boldsymbol{r})$ is needed. However, to calculate $u_\pm(\boldsymbol{r})$, the correlation function $G(\boldsymbol{r'},\boldsymbol{r''})$ needs to be resolved at two very different length scales: the length scale of the ion and that of the interface. The length scale of the interface is usually a few orders of magnitude larger than the ion size. Given that the grid spacing for the numerical discretization is determined by the shorter length scale of the ions, attempting to resolve features at the interface length scale would necessitate an extremely large number of grid points. Since it is computationally inefficient to invert large matrices, getting an accurate numerical solution for $G(\boldsymbol{r'},\boldsymbol{r''})$ and hence $u_\pm(\boldsymbol{r})$ becomes practically intractable. This dual-length scale issue was the one that was alluded to in the Introduction chapter and can be dealt with using a decomposition scheme that we describe below. To calculate $u_\pm$ at any position $\boldsymbol{r}$, the total correlation function is decoupled into the short-range contribution (subscript 'S') associated with the ion size and long-range contribution (subscript 'L') associated with the interface thickness

as

$$G(\boldsymbol{r'}, \boldsymbol{r''}) = G_{\mathrm{S}}(\boldsymbol{r'}, \boldsymbol{r''}, \boldsymbol{r}) + G_{\mathrm{L}}(\boldsymbol{r'}, \boldsymbol{r''}, \boldsymbol{r}) \tag{2.28}$$

The contribution of the local electrostatic environment to $u_{\pm}(\boldsymbol{r})$ is included through G_{S}, whereas the long-range component G_{L} accounts for spatially varying ionic strength and dielectric permittivity. Hence, the differential equation for G_{S} is constructed from Equation (2.13) by replacing the spatially varying ionic strength and dielectric permittivity with their local counterparts $\epsilon(\boldsymbol{r})$ and $I(\boldsymbol{r})$, which yields

$$-\epsilon(\boldsymbol{r})\nabla^2_{\boldsymbol{r'}} G_{\mathrm{S}}(\boldsymbol{r'}, \boldsymbol{r''}, \boldsymbol{r}) + 2I(\boldsymbol{r}) G_{\mathrm{S}}(\boldsymbol{r'}, \boldsymbol{r''}, \boldsymbol{r}) = \delta(\boldsymbol{r'} - \boldsymbol{r''}) \tag{2.29}$$

Since, $\epsilon(\boldsymbol{r})$ and $I(\boldsymbol{r})$ are independent of the differential variable $\boldsymbol{r'}$ in the above equation, G_{S} has a Debye-Hückel style analytical form similar to G_{b},

$$G_{\mathrm{S}}(\boldsymbol{r'}, \boldsymbol{r''}, \boldsymbol{r}) = \frac{\mathrm{e}^{-\kappa(\boldsymbol{r})|\boldsymbol{r'} - \boldsymbol{r''}|}}{4\pi\epsilon(\boldsymbol{r})|\boldsymbol{r'} - \boldsymbol{r''}|} \tag{2.30}$$

For G_{L}, combining Equations (2.13), (2.28) and (2.29) gives

$$-\nabla_{\boldsymbol{r'}}.[\epsilon(\boldsymbol{r'})\nabla_{\boldsymbol{r'}} G_{\mathrm{L}}(\boldsymbol{r'}, \boldsymbol{r''}, \boldsymbol{r})] + 2I(\boldsymbol{r'}) G_{\mathrm{L}}(\boldsymbol{r'}, \boldsymbol{r''}, \boldsymbol{r}) = S(\boldsymbol{r'}, \boldsymbol{r''}, \boldsymbol{r}) \tag{2.31}$$

where the non-local source term S is

$$S(\boldsymbol{r'}, \boldsymbol{r''}, \boldsymbol{r}) = \nabla_{\boldsymbol{r'}}.((\epsilon(\boldsymbol{r'}) - \epsilon(\boldsymbol{r}))\nabla_{\boldsymbol{r'}} G_{\mathrm{S}}(\boldsymbol{r'}, \boldsymbol{r''}, \boldsymbol{r})) - 2(I(\boldsymbol{r'}) - I(\boldsymbol{r}))G_{\mathrm{S}}(\boldsymbol{r'}, \boldsymbol{r''}, \boldsymbol{r}) \tag{2.32}$$

It can be seen from the above source term that G_{L} accounts for all the non-local electrostatic effects associated with the spatially-varying ionic strength and dielectric permittivity, where the local values $I(\boldsymbol{r''})$ and $\epsilon(\boldsymbol{r''})$ are taken as the reference. S becomes zero as $\boldsymbol{r'}$ approaches $\boldsymbol{r''}$, which indicates that G_{L} does not include any local contribution and is also free of the divergence problem. It is also important to note that although G_{S} and G_{L} are functions of $\boldsymbol{r}$, the total correlation function G is not a function of $\boldsymbol{r}$. This is because of the construction of $G_{\mathrm{L}}(\boldsymbol{r'}, \boldsymbol{r''}, \boldsymbol{r})$ as $G(\boldsymbol{r'}, \boldsymbol{r''}) - G_{\mathrm{S}}(\boldsymbol{r'}, \boldsymbol{r''}, \boldsymbol{r})$. For every position $\boldsymbol{r}$ where the self-energy is calculated, we evaluate G_{S} and G_{L} which are dependent on $\boldsymbol{r}$ but their sum G does not depend on $\boldsymbol{r}$.

Based on the above decomposition scheme, we get the following expression for self-energy

$$u_{\pm}(\boldsymbol{r}) = \frac{q^2_{\pm}}{2}\left[\int_{\boldsymbol{r'}, \boldsymbol{r''}} h_{\pm} G_{\mathrm{S}} h_{\pm} + \int_{\boldsymbol{r'}, \boldsymbol{r''}} h_{\pm} G_{\mathrm{L}} h_{\pm}\right] \tag{2.33}$$

To further simplify the above equation, we need to look at the physical meaning of self-energy. $u_{\pm}(\boldsymbol{r})$ is essentially the work needed to gather the constituting charges of the test ion from infinity to position $\boldsymbol{r}$ in the presence of a given electrostatic environment. This work depends on the charge spread of the ion $h_{\pm}$ as shown in Equation 2.16. However, the charge spread on the ion will only be crucial to the electrostatic forces originating in the

close neighborhood of the test ion. The first term on the r.h.s of the above equation is the short-range component of the self-energy $u_{\pm,\mathrm{S}}(\boldsymbol{r})$ and can be evaluated analytically from Equations (2.24) and (2.30)

$$u_{\pm,\mathrm{S}}(\boldsymbol{r}) = \frac{q_\pm^2}{8\pi\epsilon(\boldsymbol{r})a_\pm} - \frac{q_\pm^2\kappa(\boldsymbol{r})}{8\pi\epsilon(\boldsymbol{r})}\exp\left(\frac{a_\pm^2\kappa(\boldsymbol{r})^2}{\pi}\right)\mathrm{erfc}\left(\frac{a_\pm\kappa(\boldsymbol{r})}{\sqrt{\pi}}\right) \tag{2.34}$$

In contrast, the electrostatic effects acting from far away are insensitive to the details of the charge distribution; or equivalently, the test ion can be taken as a point charge, $h_\pm(\boldsymbol{r'}-\boldsymbol{r}) = \delta_\pm(\boldsymbol{r'}-\boldsymbol{r})$. Thus the second term in Equation (2.33) now becomes

$$u_\pm(\boldsymbol{r}) = u_{\pm,\mathrm{S}}(\boldsymbol{r}) + \frac{q_\pm^2}{2}G_\mathrm{L}(\boldsymbol{r},\boldsymbol{r},\boldsymbol{r}) \tag{2.35}$$

The long-range self-energy in the above equation is evaluated from the same point correlation function $G_\mathrm{L}(\boldsymbol{r},\boldsymbol{r},\boldsymbol{r})$. The reason this decomposition is self-consistent because in the bulk solution, G_L becomes zero and $u_{\pm,\mathrm{S}}(\boldsymbol{r})$ matches $u_{\pm,\mathrm{b}}$ as given in Eq. 2.25. No other combination of G_S and G_L can recover the analytical form of the self energy in the bulk.

With the above decomposition scheme, we only need to resolve G_L at a single length scale associated with the interface thickness, thus making the numerical calculation tractable[105]. In the extreme case where the interface thickness is comparable to the ion size, we can directly discretize the correlation function using a single grid size and the above decomposition procedure is not necessary. However, for simplicity, all the results shown in this thesis are obtained using this decomposition scheme.

Although, in principle, one can directly solve for G_L using Equation 2.31, the existence of the complex S term makes the procedure a little cumbersome. Fortunately, we can further transform the Equation 2.35 by rewriting G_L using the functions G and G_S as shown below

$$u_\pm(\boldsymbol{r}) = u_{\pm,\mathrm{S}}(\boldsymbol{r}) + \frac{q_\pm^2}{2}\lim_{\boldsymbol{r'},\boldsymbol{r''}\to\boldsymbol{r}}\left(G(\boldsymbol{r'},\boldsymbol{r''}) - G_\mathrm{S}(\boldsymbol{r'},\boldsymbol{r''},\boldsymbol{r})\right) \tag{2.36}$$

We next define the free space correlation function $G_\mathrm{O}(\boldsymbol{r'},\boldsymbol{r''},\boldsymbol{r})$ using local $\epsilon(\boldsymbol{r})$ as

$$-\epsilon(\boldsymbol{r})\nabla^2_{\boldsymbol{r'}}G_\mathrm{O}(\boldsymbol{r'},\boldsymbol{r''},\boldsymbol{r}) = \delta(\boldsymbol{r'}-\boldsymbol{r''}) \tag{2.37}$$

Adding and subtracting G_O to Equation 2.36 yields

$$u_\pm(\boldsymbol{r}) = u_{\pm,\mathrm{S}}(\boldsymbol{r}) + \frac{q_\pm^2}{2}\lim_{\boldsymbol{r'},\boldsymbol{r''}\to\boldsymbol{r}}\left(G - G_\mathrm{O}\right) + \frac{q_\pm^2}{2}\lim_{\boldsymbol{r'},\boldsymbol{r''}\to\boldsymbol{r}}\left(G_\mathrm{O} - G_\mathrm{S}\right) \tag{2.38}$$

Solving for the limit in the third term leaves us with the following simplified expression for the total self-energy $u_\pm(\boldsymbol{r})$

$$u_\pm(\boldsymbol{r}) = u_{\pm,\mathrm{S}}(\boldsymbol{r}) + \frac{q_\pm^2\kappa(\boldsymbol{r})}{8\pi\epsilon(\boldsymbol{r})} + \frac{q_\pm^2}{2}\lim_{\boldsymbol{r'},\boldsymbol{r''}\to\boldsymbol{r}}\left(G - G_\mathrm{O}\right) \tag{2.39}$$

In the following sections, we present the simplified equations for symmetric planar interfaces and discuss the numerical method to solve these equations, particularly focusing on a new Sturm–Liouville theory-inspired approach we have developed to evaluate the electrostatic correlation.

2.5 Equations for symmetric planar interfaces

We now apply the theory to the case of symmetric planar interfaces, examples of which include a salt solution in contact with uniformly charged infinite plates or an interface between coexisting vapor and liquid phases in ionic fluids. A planar interface is also a very good approximation for electrical double layers near charged nanochannels, parallel plate capacitors, or even large spherical particles. Without loss of generalization, we assume z to be the direction normal to the interface, which makes the electrostatic potential ψ and ion concentration $c_\pm$ to be a function of the coordinate z. The fixed charge density $\rho_{\text{fix}}(z)$ now contains any uniformly charged plates in the system. For such planar interfaces, equations 2.12 -2.14, 2.18, 2.19, 2.37, and 2.39 become

$$-\nabla.[\epsilon(z)\nabla\psi(z)] = \rho_{\text{fix}}(z) + q_+c_+(z) - q_-c_-(z) \tag{2.40}$$

$$c_\pm(z) = \lambda_\pm \exp[\mp q_\pm\psi(z) - u_\pm(z) - v_\pm\eta(z)] \tag{2.41}$$

$$u_\pm(z) = u_{\pm,\text{S}}(z) + \frac{q_\pm^2\kappa(z)}{8\pi\epsilon(z)} + \frac{q_\pm^2}{2}\lim_{\boldsymbol{r}',\boldsymbol{r}''\to\boldsymbol{r}}(G - G_{\text{O}}) \tag{2.42}$$

$$-\nabla_{\boldsymbol{r}'}.[\epsilon(z')\nabla_{\boldsymbol{r}'}G(\boldsymbol{r}',\boldsymbol{r}'')] + 2I(z')G(\boldsymbol{r}',\boldsymbol{r}'') = \delta(\boldsymbol{r}'-\boldsymbol{r}'') \tag{2.43}$$

$$-\epsilon(z)\nabla^2_{\boldsymbol{r}'}G_{\text{O}}(\boldsymbol{r}',\boldsymbol{r}'',z) = \delta(\boldsymbol{r}'-\boldsymbol{r}'') \tag{2.44}$$

$$\eta(z) = \frac{\mu_{\text{s}}}{v_{\text{s}}} - \frac{1}{v_s}\ln[1 - v_+c_+(z) - v_-c_-(z)] \tag{2.45}$$

$$\begin{aligned}\mathcal{W} = &\int dz\left[\frac{1}{2}\psi\left(\rho_{\text{fix}} - q_+c_+ + q_-c_-\right) - c_+ - c_- + \frac{\ln(1-c_+v_+-c_-v_-) - (1-c_+v_+-c_-v_-)}{v_{\text{s}}}\right]\\ &+\frac{1}{2}\int dz\int d\boldsymbol{r}'\int d\boldsymbol{r}''\int_0^1 d\tau[G(\boldsymbol{r}',\boldsymbol{r}'',\tau) - G(\boldsymbol{r}',\boldsymbol{r}'')]\left[\sum_{i=+,-}q_i^2c_i(z)h_i(\boldsymbol{r}'-\boldsymbol{r})h_i(\boldsymbol{r}''-\boldsymbol{r})\right]\end{aligned} \tag{2.46}$$

Depending upon the system's characteristics, different boundary conditions (BCs) are possible for ψ. In the bulk solution, we have a Dirichlet boundary condition, $\psi = \psi_{\text{b}}$. This condition also gives fugacity $\lambda_\pm$ in terms of bulk salt concentrations, self-energy, and η from Equation 2.41. BCs for ψ next to a plate with surface charge density $\bar{\sigma}$ can be written from Eq. 2.40 as $\vec{n}\cdot[\![\epsilon\nabla\psi]\!]_S = \bar{\sigma}$, where $[\![\bullet]\!]_S$ represents the jump in $\bullet$ across the surface S.

2.5.1 The three-level iterative algorithm

Equations 2.40, 2.43, and 2.44 are coupled non-linear equations which we solve using a three-level iterative algorithm. We begin the k^{th} iteration step with ψ^k, $c_\pm^k$, $u_\pm^k$, and η^k stored in memory. ψ^{k+1} is then numerically calculated by solving the following

$$-\frac{d}{dz}\left(\epsilon(z)\frac{d\psi^{k+1}(z)}{dz}\right) = \sum_{i=+,-} iq_i\lambda_i\exp[-u_i^k(z) - v_i\eta^k(z)]\exp[-iq_i\psi^{k+1}(z)] \tag{2.47}$$

After substituting $u_{\pm}^{k}$ and η^{k} in the first exponent term on the right-hand side, the above implicit non-linear equation in ψ^{k+1} can be solved with a straightforward Newton-Raphson scheme, the initial guess for which will be ψ^{k}. Next using ψ^{k+1}, $u_{\pm}^{k}$, η^{k} and Equation 2.41, updated concentrations values can be evaluated

$$\bar{c}_{\pm}^{k+1}(z) = \lambda_{\pm} \exp[\mp q_{\pm}\psi^{k+1}(z) - u_{\pm}^{k}(z) - v_{\pm}\eta^{k}(z)] \tag{2.48}$$

However, since these equations involve exponential non-linearities which are highly prone to instability, we mix $\bar{c}^{k+1}$ with old $c_{\pm}^{k}$ using a mixing ratio $m \ \leq 1$, to get $c_{\pm}^{k+1}$ as follows

$$c_{\pm}^{k+1} = m\bar{c}_{\pm}^{k+1} + (1-m)c_{\pm}^{k} \tag{2.49}$$

From $c_{\pm}^{k+1}$, we can get updated $u_{\pm}$ and η as

$$u_{\pm}^{k+1}(z) = u_{\pm,\mathrm{S}}^{k+1}(z) + \frac{q_{\pm}^{2}\kappa^{k+1}(z)}{8\pi\epsilon(z)} + \frac{q_{\pm}^{2}}{2}\lim_{\boldsymbol{r}',\boldsymbol{r}''\to\boldsymbol{r}}(G^{k+1} - G_{\mathrm{O}}) \tag{2.50}$$

$$-\nabla_{\boldsymbol{r}'}.[\epsilon(z')\nabla_{\boldsymbol{r}'}G^{k+1}(\boldsymbol{r}',\boldsymbol{r}'')] + 2I^{k+1}(z')G^{k+1}(\boldsymbol{r}',\boldsymbol{r}'') = \delta(\boldsymbol{r}'-\boldsymbol{r}'') \tag{2.51}$$

$$\eta^{k+1}(z) = \frac{\mu_{\mathrm{s}}}{v_{\mathrm{s}}} - \frac{1}{v_{s}}\ln[1 - v_{+}c_{+}^{k+1}(z) - v_{-}c_{-}^{k+1}(z)] \tag{2.52}$$

The stop criterion for this iteration scheme is

$$\sum_{i=+,-}\frac{\|\bar{c}_{i}^{k+1} - c_{i}^{k}\|_{2}}{\|c_{i}^{k}\|_{2}} < \delta \tag{2.53}$$

where $\| \bullet \|_{2}$ represents L-2 or Euclidean norm and δ is some preset small positive number. The above scheme is a three-level iterative algorithm. The lowest level of iterative procedure gives the solution to the implicit non-linear problem in Equation 2.47 for given $u_{\pm}^{k}$, and η^{k}. The next step which requires iteration is the evaluation of G^{k} for given $c_{\pm}^{k}$ using Equation 2.51. In section 2.5.3, we describe how Equation 2.51 can be solved more efficiently by converting it into an implicit non-linear problem. The third and highest level of iteration is over $c_{\pm}$, the convergence criterion for which is given in Equation 2.53. The first and third levels of the algorithm has two modifications compared to the original version of Xu and Maggs[105] two-level algorithm. The first modification is the introduction of a mixing rule for old and new $c_{\pm}$, as outlined in Equation 2.49. The second one is using Equation 2.53 as convergence criterion instead of $\max|\psi^{k+1} - \psi^{k}| < \delta$. As stated above the mixing rule is used to improve stability, whereas the choice of Equation 2.53 ensures that the convergence criterion is not sensitive to the value of the mixing ratios m. Additionally, as a side note, it is important to highlight that $\epsilon(z)$ is often expressed as a function of the volume fraction of ions and solvent. For such dielectric permittivity models, ϵ will change with every iteration step. This feature can be straightforwardly incorporated into this algorithm by replacing $\epsilon(z)$ with $\epsilon^{k}(z)$ in Equation 2.47, and with $\epsilon^{k+1}(z)$ in equations 2.50 and 2.51.

Furthermore, in the case where all the ions and solvent molecules have the same excluded volumes, i.e., $v_+ = v_- = v_s$, using equation 2.17, equations 2.47 and 2.48 can be rewritten as

$$-\frac{d}{dz}\left(\epsilon(z)\frac{d\psi^{k+1}(z)}{dz}\right) = \frac{\sum_{i=+,-} iq_i\lambda_i \exp[-u_i^k(z)]\exp[-iq_i\psi^{k+1}(z)]}{1 + v_+\lambda_+ \exp[-q_+\psi^k(z) - u_+^k(z)] + v_-\lambda_- \exp[q_-\psi^k(z) - u_-^k(z)]} \tag{2.54}$$

$$\bar{c}_\pm^{k+1}(z) = \frac{\lambda_\pm \exp[\mp q_\pm\psi^k(z) - u_\pm^k(z)]}{1 + v_+\lambda_+ \exp[-q_+\psi^k(z) - u_+^k(z)] + v_-\lambda_- \exp[q_-\psi^k(z) - u_-^k(z)]} \tag{2.55}$$

The above manipulations offer two advantages. Firstly, since the incompressibility factor η is evaluated at the $k+1$ iteration level, we get faster convergence. Secondly, we can now use higher values for the mixing ratio m without facing the risk of encountering negative values in the argument of the logarithmic function. This second benefit becomes of great consequence when solving for extremely high surface charge densities or ion sizes, where a very high volume fraction of ions is expected near the surface. In general, it is advisable to first solve the entire set of self-consistent equations using the same excluded volumes for all types of molecules and then use that solution as an initial guess to solve the problem with the true values of excluded volumes. In general, the solution of mean-field PB or the Modified Gaussian Renormalized Fluctuation Theory for a different parameter set can be used as the initial guesses, ψ^0, and $c_\pm^0$. From $c_\pm$, η can be calculated directly from the Equation 2.45. The method for calculation of $u_\pm$ from equations 2.42 - 2.44, which is also the rate-limiting step in the three-level iterative algorithm, is described in the following subsections.

2.5.2 Fourier decomposition of the correlation function G

To obtain the self-energy $u_\pm(z)$, we need to solve the correlation functions G and G_O in the entire domain. In the case of symmetric planar interfaces, it is advantageous to work in cylindrical coordinates (R, θ, z). Using cylindrical coordinates, $G(\boldsymbol{r'}, \boldsymbol{r''})$ can be written as $G(\rho', z', z'')$, where we have removed the θ' coordinate from notation because of symmetry and assumed the axis of the coordinate to pass through $\boldsymbol{r''}$, i.e., $R'' = 0$. In terms of Cartesian coordinates x' and y', $R' = \sqrt{x'^2 + y'^2}$. Next, from the definition of Hankel transform

$$G(R', z', z'') = \frac{1}{2\pi}\int_0^\infty s ds J_0(sR')\hat{G}(s, z', z'') \tag{2.56}$$

where J_0 is the zeroth order Bessel function and s is the frequency mode. Using the above expression, Equation 2.43 can be written as

$$-\frac{d}{dz'}\left(\epsilon(z')\frac{d\hat{G}(s, z', z'')}{dz'}\right) + \epsilon(z')(\kappa^2(z') + s^2)\hat{G}(s, z', z'') = \delta(z' - z'') \tag{2.57}$$

$\kappa(z') = [2I(z')/\epsilon(z')]^{1/2}$ is the inverse of the local Debye screening length. Similarly, after applying Hankel transform on G_O, Equation 2.44 becomes

$$-\epsilon(z)\frac{\partial^2\hat{G}_O(s, z', z'')}{\partial z'^2} + \epsilon(z)s^2\hat{G}_O(s, z', z'') = \delta(z' - z'') \tag{2.58}$$

$\hat{G}_{\mathrm{O}}$ has an analytical solution given by

$$\hat{G}_{\mathrm{O}}(s, z', z'') = \frac{\mathrm{e}^{-s|z'-z''|}}{2\epsilon(z)s} \tag{2.59}$$

Since, to calculate $u_{\pm}(z)$ we only need G and G_{O} in the limit $\boldsymbol{r}', \boldsymbol{r}'' \to \boldsymbol{r}$, i.e. $R' = 0$ and $z' = z'' = z$, one can write the last term in Equation 2.42 in terms of $\hat{G}$ and $\hat{G}_{\mathrm{O}}$ as

$$\frac{q_{\pm}^2}{2} \lim_{\boldsymbol{r}', \boldsymbol{r}'' \to \boldsymbol{r}} (G - G_{\mathrm{O}}) = \frac{q_{\pm}^2}{4\pi} \int_0^{\infty} \left(\hat{G}(s, z, z) - \hat{G}_{\mathrm{O}}(s, z, z) \right) s ds \tag{2.60}$$

where we have used the fact that $J_0(0)$ is equal to 1. The integral above is evaluated using the Legendre-Gauss quadrature method. As the value of $\hat{G}$ for one quadrature point will be independent of the other, the integration step can be trivially parallelized. Furthermore, to increase the accuracy of the semi-infinite integral we perform a logarithmic transformation on s, $\nu = \log(1 + s)$. This transformation shrinks the integration interval thus allowing us to calculate the value of the integral with a small number of quadrature points. The cutoff value S for the integral and the number of quadrature points are hyper-parameters that can be decided by reproducing the known analytical solution to the above limit in the bulk solution

$$\frac{q_{\pm}^2}{2} \lim_{\boldsymbol{r}', \boldsymbol{r}'' \to \boldsymbol{r}} (G_{\mathrm{b}} - G_{\mathrm{O}}) = -\frac{q_{\pm}^2 \kappa_{\mathrm{b}}}{8\pi\epsilon_{\mathrm{b}}} \tag{2.61}$$

Note that like $\hat{G}_{\mathrm{O}}$, G_{O} also has an analytical solution. However, to cancel the errors arising from numerical integration, like G we perform a Hankel transform on G_{O} as well.

The above Fourier decomposition of $\hat{G}$ and the Legendre-Gauss quadrature method for integration was proposed previously by Xu and Maggs[105]. They also proposed a finite-difference-based discretization procedure for Equation 2.57 and the inversion of the corresponding symmetric and positive definitive sparse matrix to solve for $\hat{G}$. Since, only diagonal elements of $\hat{G}$ are needed, this inversion step was further optimized using the Schur complements recursively produced in the intermediate steps of the LDL factorization. However, accurately discretizing the Dirac delta function requires a very large number of grid points. Even after using a large number of points, the errors at the boundary can be very large. This makes the inversion step not only slow but also prone to errors, especially in systems where there are sharp changes in the concentration profiles. Furthermore, as the equations are to be solved repeatedly in every iteration step, these errors can accumulate over time. In the next subsection, we present a new alternative approach to solve for $\hat{G}$ to overcome these issues.

2.5.3 Sturm–Liouville theory inspired approach to solve for G

Here, we present a Sturm–Liouville theory-inspired approach to solve for $\hat{G}$ that converts the aforementioned two-dimensional matrix inversion problem into two one-dimensional problems. We also analytically handle the Dirac delta function hence reducing the required

number of grid points. We start by defining the operator $\mathcal{L}$ as

$$\mathcal{L} = -\frac{d}{dz'}\left(\epsilon(z')\frac{d}{dz'}\right) + \epsilon(z')(\kappa^2(z') + s^2) \tag{2.62}$$

Using $\mathcal{L}$, we can rewrite Equation 2.57 into two parts as

$$\mathcal{L}\hat{G}(s, z', z'') = 0, \quad (z'' \neq z') \tag{2.63}$$

$$\epsilon(z')\left[\frac{d\hat{G}}{dz'}(s, z' - 0, z') - \frac{d\hat{G}}{dz'}(s, z' + 0, z')\right] = 1, \quad (z'' = z') \tag{2.64}$$

where Equation 2.64 is obtained by integrating Equation 2.57 from $z' - 0$ to $z' + 0$ and using finiteness of functions ϵ, κ and $\hat{G}$. Additionally, from continuity of $\hat{G}$ we have

$$\hat{G}(s, z' - 0, z') = \hat{G}(s, z' + 0, z') \tag{2.65}$$

All the three conditions above can be satisfied by a solution of the form

$$\hat{G}(s, z', z'') = \begin{cases} A(s, z'')U(s, z'), & \text{if } z' \leq z'' \\ B(s, z'')V(s, z'), & \text{if } z' \geq z'' \end{cases} \tag{2.66}$$

In the above equation, both U and V satisfy

$$\mathcal{L}U(s, z') = 0 \tag{2.67}$$

$$\mathcal{L}V(s, z') = 0 \tag{2.68}$$

where for any z'', U satisfies the BC for $\hat{G}$ at $z' \to -\infty$ and V satisfies BC for $\hat{G}$ at $z' \to \infty$. The unknown functions A and B are obtained by imposing conditions 2.64 and 2.65 as follows

$$\epsilon(z')[A(s, z')U'(s, z') - B(s, z')V'(s, z')] = 1 \tag{2.69}$$

$$A(s, z')U(s, z') = B(s, z')V(s, z') \tag{2.70}$$

where U' and V' represent the first derivatives with respect to z'. Solving the above two equations for A and B we get

$$A(s, z') = C(s, z')V(s, z') \tag{2.71}$$

$$B(s, z') = C(s, z')U(s, z') \tag{2.72}$$

with $C(s, z')$ defined as

$$C(s, z') = \frac{1}{\epsilon(z')[V(s, z')U'(s, z') - U(s, z')V'(s, z')]} \tag{2.73}$$

The full solution to $\hat{G}$ reads

$$\hat{G}(s,z',z'') = \begin{cases} C(s,z'')V(s,z'')U(s,z'), & \text{if } z' < z'' \\ C(s,z'')U(s,z'')V(s,z'), & \text{if } z' > z'' \end{cases} \tag{2.74}$$

Next, as only the same point $\hat{G}$ is needed to evaluate the self-energy we can simplify the above equation as follows

$$\hat{G}(s,z,z) = \frac{U(s,z)V(s,z)}{\epsilon(z)[V(s,z)U'(s,z) - U(s,z)V'(s,z)]} \tag{2.75}$$

By dividing the denominator by the numerator we can further simplify the above expression

$$\hat{G}(s,z,z) = \frac{1}{\epsilon(z)[\frac{U'(s,z)}{U(s,z)} - \frac{V'(s,z)}{V(s,z)}]} \tag{2.76}$$

Thus, we now have an expression for $\hat{G}$ in terms of U and V. U and V can be solved by a forward and backward marching algorithm, starting with the BCs at their respective ends. Although with this new approach, we get rid of the inefficient matrix inversion process, the forward and backward marching algorithms for U and V can still be unstable, especially for larger domains as the errors with each marching step can accumulate and lead to divergence. This issue can be easily handled by introducing a simple variable change. We define two new variables P and Q as follows

$$P = \log U, \quad Q = \log V \tag{2.77}$$

This logarithmic transformation not only re-scales U and V to smaller, more manageable values but also allows a straightforward evaluation of $\hat{G}$ from Equation 2.76 as

$$\hat{G}(s,z,z) = \frac{1}{\epsilon(z)[P'(s,z) - Q'(s,z)]} \tag{2.78}$$

where P' and Q' again represent the first derivatives with respect to z. Putting the definitions of P and Q in Equations 2.67 and 2.68, we get the following differential equation form for P' and Q'

$$-\frac{dF}{dz} + (\kappa^2(z) + s^2) - \frac{F(s,z)}{\epsilon(z)}\frac{d\epsilon(z)}{dz} = F^2(s,z) \tag{2.79}$$

where $F = P'$ or Q'. The above equation though implicit and non-linear is easily solvable in only a few iteration steps using the Newton-Raphson method. The initial guesses for P' and Q' can be chosen as per the boundary conditions. Because of the logarithmic re-scaling of U and V, P' and Q' do not vary significantly in the domain, and hence the boundary condition motivated initial guesses provide very fast convergence. Furthermore, the enhanced accuracy achieved in the calculation of $\hat{G}$ through the use of Equation 2.78 allows us to utilize the analytical solution of $\hat{G}_O$ in Equation 2.60. In the previously proposed approach by Xu and Maggs[105], similar to $\hat{G}$, $\hat{G}_O$ was also determined through matrix inversion to cancel out numerical errors by taking advantage of the subtraction step between $\hat{G}$ and $\hat{G}_O$. This flexibility to use the analytical solution of $\hat{G}_O$ in our new approach significantly reduces the computational cost of the iterative algorithm.

2.5.4 Boundary conditions for G

The first boundary condition (BC) for $\hat{G}$ and hence, U and V, comes from the fact that two infinitely separated points are completely uncorrelated. Mathematically this can be written as

$$\lim_{|\boldsymbol{r}'-\boldsymbol{r}''|\to\infty} G(\boldsymbol{r}', \boldsymbol{r}'') = 0 \tag{2.80}$$

From Equation 2.56, the above limit then implies

$$\lim_{|z'-z''|\to\infty} \hat{G}(s, z', z'') = 0 \tag{2.81}$$

Thus, for finite z'', using Equation 2.66 we can write

$$U(s, z' \to -\infty) = 0 \tag{2.82}$$

$$V(s, z' \to \infty) = 0 \tag{2.83}$$

The other boundary conditions for U and V and hence P' and Q' are system-specific. Below, we describe BCs for three different systems studied in this thesis. The initial guesses for the non-linear implicit solvers for both $P'(z)$ and $Q'(z)$ are uniformly set to these boundary values to ensure that the guesses satisfy the BCs.

2.5.4.1 Single charged surface in contact with a salt solution

We consider a system with a charged plate located at $z = 0$ in contact with an infinite salt reservoir in the region $z > 0$. For $z < 0$, $\epsilon(z)$ is a constant equal to ϵ_{P} and $\kappa(z) = 0$. The equation for U in the region $z < 0$ thus becomes

$$-\frac{d^2U}{dz^2} + s^2U = 0 \tag{2.84}$$

For the condition given in Equation 2.82, U has the following analytical solution in $z < 0$

$$U(s, z) = a \exp(sz) \tag{2.85}$$

Next, to connect the solution in the region $z < 0$ to $z > 0$, we integrate Equation 2.67 from $z = 0-$ to $z = 0+$

$$\epsilon(z = 0+)\frac{dU}{dz}\bigg|_{z=0+} = \epsilon_{\mathrm{P}}\frac{dU}{dz}\bigg|_{z=0-} \tag{2.86}$$

From Equation 2.85, and using continuity of U, the r.h.s of the above equation can be written as

$$\epsilon(z = 0+)\frac{dU}{dz}\bigg|_{z=0+} = \epsilon_{\mathrm{P}} sU|_{z=0+} \tag{2.87}$$

Thus, in terms of P, we get the following boundary condition at $z = 0$

$$\left.\frac{dP}{dz}\right|_{z=0+} = P'|_{z=0+} = s\frac{\epsilon_{\mathrm{P}}}{\epsilon(z=0+)} \tag{2.88}$$

Similarly, in the region $z > L_{\mathrm{z}}$, i.e. the bulk solution, $\epsilon(z)$ is a constant equal to ϵ_{P} and $\kappa(z) = \kappa_{\mathrm{b}}$. The equation for V in this region is

$$-\frac{d^2V}{dz^2} + (s^2 + \kappa_{\mathrm{b}}^2)V = 0 \tag{2.89}$$

Combining 2.89 with Equation 2.83, we get

$$V(s,z) = b\exp(-(s^2 + \kappa_{\mathrm{b}}^2)^{1/2}z) \tag{2.90}$$

Now, to connect the solution in the region $z < L_{\mathrm{z}}$ to $z > L_{\mathrm{z}}$, we integrate Equation 2.68 from $z = L_{\mathrm{z}}-$ to $z = L_{\mathrm{z}}+$

$$\epsilon(z = L_{\mathrm{z}}-)\left.\frac{dV}{dz}\right|_{z=L_{\mathrm{z}}-} = \epsilon_{\mathrm{S}}\left.\frac{dV}{dz}\right|_{z=L_{\mathrm{z}}+} \tag{2.91}$$

From Equation 2.90, and using continuity of V, the r.h.s of the above equation can be written as

$$\epsilon(z = L_{\mathrm{z}}-)\left.\frac{dV}{dz}\right|_{z=L_{\mathrm{z}}-} = -\epsilon_{\mathrm{S}}(s^2 + \kappa_{\mathrm{b}}^2)^{1/2}V|_{z=L_{\mathrm{z}}-} \tag{2.92}$$

Finally, in terms of Q, we get the following boundary condition at $z = L_{\mathrm{z}}$

$$\left.\frac{dQ}{dz}\right|_{z=L_{\mathrm{z}}-} = Q'|_{z=L_{\mathrm{z}}-} = -(s^2 + \kappa_{\mathrm{b}}^2)^{1/2}\frac{\epsilon_{\mathrm{S}}}{\epsilon(z = L_{\mathrm{z}}-)} \tag{2.93}$$

2.5.4.2 Two charged surfaces separated by a salt solution

We consider a system with two charged plates located at $z = 0$ and $z = L_{\mathrm{z}}$ separated by a salt solution. For $z < 0$ and $z > L_{\mathrm{z}}$, $\epsilon(z)$ is a constant equal to ϵ_{P} and $\kappa(z) = 0$. Hence, the equations for U and for V are

$$-\frac{d^2U}{dz^2} + s^2U = 0, \quad z < 0 \tag{2.94}$$

$$-\frac{d^2V}{dz^2} + s^2V = 0, \quad z > L_{\mathrm{z}} \tag{2.95}$$

For the conditions given in Equation 2.82 and 2.83, U and V have the following analytical solutions

$$U(s,z) = a\exp(sz), \quad z < 0 \tag{2.96}$$

$$V(s,z) = b\exp(-sz), \quad z > L_z \tag{2.97}$$

Next, to connect the solution for U in the region $z < 0$ to $z > 0$, we integrate Equation 2.67 from $z = 0-$ to $z = 0+$

$$\epsilon(z=0+)\frac{dU}{dz}\bigg|_{z=0+} = \epsilon_P \frac{dU}{dz}\bigg|_{z=0-} \tag{2.98}$$

From Equation 2.85, and using continuity of U, the r.h.s of the above equation can be written as

$$\epsilon(z=0+)\frac{dU}{dz}\bigg|_{z=0+} = \epsilon_P sU|_{z=0+} \tag{2.99}$$

Thus, in terms of P, we get the following boundary condition at $z = 0$

$$\frac{dP}{dz}\bigg|_{z=0+} = P'|_{z=0+} = s\frac{\epsilon_P}{\epsilon(z=0+)} \tag{2.100}$$

Similarly, to connect the solution for V in the region $z < L_z$ to $z > L_z$, we integrate Equation 2.68 from $z = L_z-$ to $z = L_z+$

$$\epsilon(z=L_z-)\frac{dV}{dz}\bigg|_{z=L_z-} = \epsilon_P \frac{dV}{dz}\bigg|_{z=L_z+} \tag{2.101}$$

From Equation 2.90, and using continuity of V, the r.h.s of the above equation can be written as

$$\epsilon(z=L_z-)\frac{dV}{dz}\bigg|_{z=L_z-} = -\epsilon_P sV|_{z=L_z-} \tag{2.102}$$

Finally, in terms of Q, we get the following boundary condition at $z = L_z$

$$\frac{dQ}{dz}\bigg|_{z=L_z-} = Q'|_{z=L_z-} = -s\frac{\epsilon_P}{\epsilon(z=L_z-)} \tag{2.103}$$

2.5.4.3 Vapor-liquid interface in ionic fluids

Consider two bulk ionic fluid phases with salt concentrations $c_{\pm,v}$ (vapor) and $c_{\pm,l}$ (liquid) in equilibrium with each other. The low-concentration vapor phase lies in the region $z < 0$ and the high-concentration liquid phase in the region $z > L_z$. The region $0 < z < L_z$ is the interface between the two phases. The dielectric permittivity is assumed to have a constant value of ϵ_S. The equation for U in the vapor phase and the equation for V in the liquid phase are

$$-\frac{d^2U}{dz^2} + (s^2 + \kappa_v)U = 0, \quad z < 0 \tag{2.104}$$

$$-\frac{d^2V}{dz^2} + (s^2 + \kappa_l)V = 0, \quad z > L_z \tag{2.105}$$

For the conditions given in Equation 2.82 and 2.83, U and V have the following analytical solutions

$$U(s,z) = a\exp((s^2 + \kappa_s^2)^{1/2}z), \quad z < 0 \tag{2.106}$$

$$V(s,z) = b\exp(-(s^2 + \kappa_l^2)^{1/2}z), \quad z > L_z \tag{2.107}$$

Like before, we connect the solutions for U and V in the bulk phases to the interface to get

$$\left.\frac{dU}{dz}\right|_{z=0-} = (s^2 + \kappa_v^2)^{1/2}U|_{z=0-} \tag{2.108}$$

$$\left.\frac{dV}{dz}\right|_{z=L_z-} = -(s^2 + \kappa_l^2)^{1/2}V|_{z=L_z-} \tag{2.109}$$

In terms of P and Q, the above two conditions at $z = 0$ and $z = L_z$ can be rewritten as

$$\left.\frac{dP}{dz}\right|_{z=0+} = P'|_{z=0+} = (s^2 + \kappa_v^2)^{1/2} \tag{2.110}$$

$$\left.\frac{dQ}{dz}\right|_{z=L_z-} = Q'|_{z=L_z-} = -(s^2 + \kappa_l^2)^{1/2} \tag{2.111}$$

2.6 Spectral methods-based discretization and Python code

The Python code for solving the equations presented in the above sections was written on top of an open-source spectral methods-based differential equation solver *Dedalus*, developed by Burns et al.[106]. Dedalus is a high-performance computational framework into which one can input any initial value, boundary value, or eigenvalue problem as plain-text strings. These strings are then translated into efficient solvers using various numerical methods inside Dedalus. We opted for spectral methods instead of commonly used finite-difference-based discretization, as in Xu and Maggs[105], due to their significantly superior efficiency in simple geometries[107]. The exponential convergence property of spectral methods is particularly useful as it allows us to accurately resolve large domains common in double layer problems with fewer grid points and consequently reduced time and memory requirements.

Multiple options for the type of basis functions over which one can expand a continuous variable or function are available within Dedalus. In this thesis, we have dealt with non-periodic finite domains and hence, have used the Chebyshev basis, consisting of Chebyshev-T polynomials. A Chebyshev grid also provides more points near the boundaries which are

crucial to resolving sharp changes in double layer structures next to strongly charged surfaces and also accurately connecting the interface to the bulk. After creating the Chebyshev grid, we instantiate a non-linear boundary value problem (NLBVP) solver class to solve the equations. Next, we input the differential equations and the boundary conditions in the form derived in the preceding sections into this solver as plain-text strings. The NLBVP class contains an efficient Newton-Raphson method that solves the non-linear problem in question for a user provided initial guess. Dedalus also offers the option to set the tolerance value for the convergence criterion. Interested readers are referred to the Dedalus' method papers for further details[106, 108–110].

2.7 Numerical Analysis

In this section, we study the speed and stability of the aforementioned algorithm for the systems described in Section 2.5.4.1,2.5.4.2 and 2.5.4.3. We demonstrate the stability of algorithm with respect to both increasing domain size and number of spectral modes N.

2.7.1 Single charged surface in contact with a salt solution

We study three different systems with charged plates located at $z = 0$ and surface charge densities $\sigma = -0.01,\ -0.1$, and -0.65 C/m^2 in contact with 0.1 M divalent salt solution, $q_+ = 2$ and $q_- = 1$, and $a_\pm = 1.5$ Å. These three surface charge densities correspond to weak, moderate and strong electrostatic coupling regimes, respectively. The dielectric constant in the region $z > 0$ is taken to be that of water, $\epsilon_S = 80$, whereas the dielectric constant in the region $z < 0$ is set to be $\epsilon_P = 1$. For the numerical calculation of the self-energy via the integral in Eq. 2.60, we used a cutoff value of $S = 32$ and a total of 24 quadrature points. These parameters values were found to be sufficient to reproduce the limit in Eq. 2.61 with very high accuracy. The tolerance parameter δ for all the Newton solvers was set to 10^{-7}. The initial guesses for electrostatic potential $\psi(z)$ and counterion concentration profiles $c^{2+}(z)$ were taken to be the solutions of the non-linear mean-field Poisson-Boltzmann equations. To ensure stability we made the conservative choice of setting the mixing ratio m to 0.1 for all three surface charge densities. However, for low σ values, $m = 1$ also gives stable iterations. $m = 0.1$ is only needed for high σ values such as -0.65 C/m^2.

Representative $\psi(z)$ and $c^{2+}(z)$ profiles for $N = 1024$ and the domain size $L_z = 20\lambda_D$ or 160 Å, where λ_D is the Debye-Hučkel length, are plotted in Figure 2.1. However, as $L_z = 20\lambda_D$ is simply an approximation for thickness of the interface which in principle is infinite, to observe the convergence of the algorithm with increasing domain size we define the error E_L as a function of domain size as:

$$E_L(L_z) = \sqrt{\sum_{i=0}^{4}[\psi(L_z, z = \frac{i}{4}\lambda_D) - \psi(L_z^{ref} = 30\lambda_D, z = \frac{i}{4}\lambda_D)]} \tag{2.112}$$

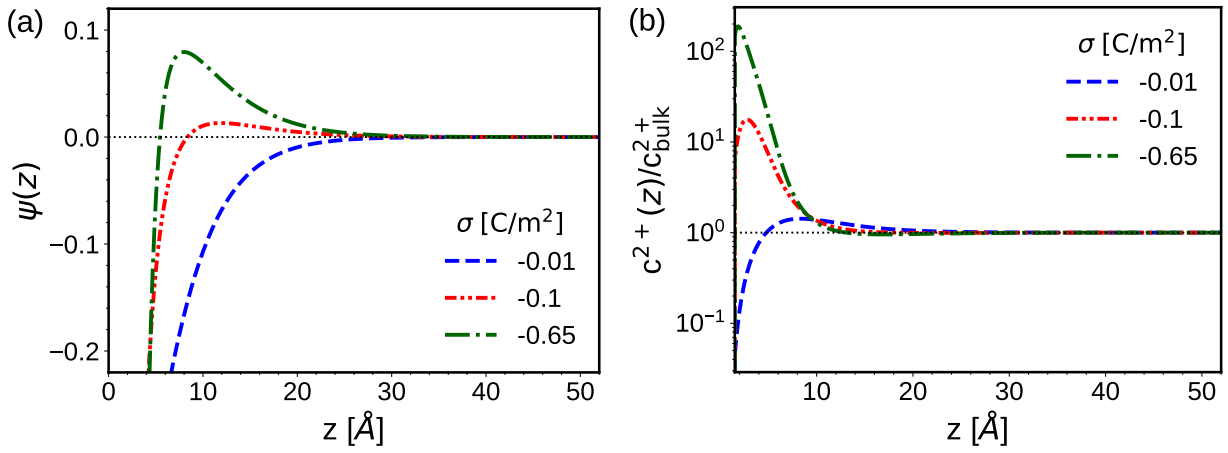

Figure 2.1: a) Electrostatic potential $\psi(z)$ profile and b) counterion concentration profile $c^{2+}(z)$ for a single charged plate system for low, medium and high surface charge densities. $q_+ = 2$, $q_- = 1$, $c_\mathrm{b} = 0.1$ M, $a_{\pm,s} = 1.5$ Å, $\varepsilon_\mathrm{S} = 80$, $\varepsilon_\mathrm{P} = 1$, $N = 1024$ and $L_\mathrm{z} = 20\lambda_\mathrm{D}$.

As the characteristic decay length of the interface is roughly λ_D, the choice of $L_\mathrm{z} = 30\lambda_\mathrm{D}$ as the reference is large enough. Figure 2.2 plots $\mathrm{E_L}$ showing convergence in $\psi(z)$ with increasing L_z for all three σ values. Hence, a value of $L_\mathrm{z} = 20\lambda_\mathrm{D}$ is large enough to capture the structure of the interface.

Next, setting $L_\mathrm{z} = 20\lambda_\mathrm{D}$, we study the rate of convergence with number of spectral modes N using the following two error metrics

$$E_\mathrm{surf}(N) = |\psi(N, z = 0) - \psi(N^\mathrm{ref} = 1024, z = 0)| \tag{2.113}$$

$$E_\mathrm{profile}(N) = \sqrt{\sum_{i=1}^{10} [\psi(N, z = \frac{i}{10} L_\mathrm{z}) - \psi(N^\mathrm{ref} = 1024, z = \frac{i}{10} L_\mathrm{z})]} \tag{2.114}$$

where E_surf measures error in surface electrostatic potential and E_profile measures error in electrostatic potential profile in the interface. The semi-log plots of these two error metrics as a function of N are plotted in Figure 2.3. For all three σ values the logarithm of these errors linearly decreases with N, proving spectral rate of convergence for the algorithm. Note that a minimum of $N = 160$ is needed for stable calculation of the double layer profile for $\sigma = -0.65$ C/m^2. For $N < 160$, it becomes very difficult to resolve steep changes in $\psi(z)$ associated with such high σ, leading to numerical instability.

The Sturm-Liouville theory inspired approach to analytically handle the Dirac delta function in Equation 2.57 allows us to use standard spectral methods to solve our differential equations thus ensuring spectral convergence. This is a significant improvement compared

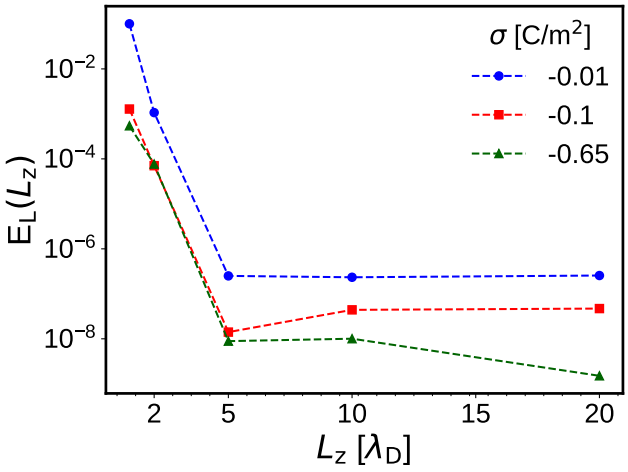

Figure 2.2: L_2 norm of the error in the electrostatic potential profile (E_L) with increasing domain size for low, medium and high surface charge densities. $q_+ = 2$, $q_- = 1$, $c_b = 0.1$ M, $a_{\pm,s} = 1.5$ Å, $\varepsilon_S = 80$, $\varepsilon_P = 1$ and $N = 1024$.

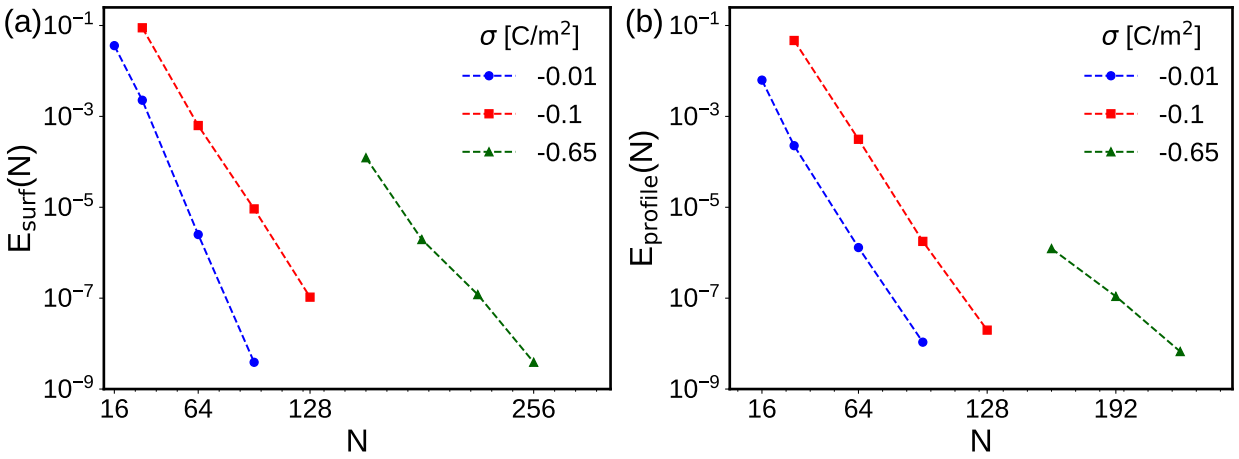

Figure 2.3: L_2 norm of the error in the a) surface electrostatic potential (E_{surf}) and b) electrostatic potential profile ($E_{profile}$) as a function of number of spectral modes for a single charged plate system for low, medium and high surface charge densities. $q_+ = 2$, $q_- = 1$, $c_b = 0.1$ M, $a_{\pm,s} = 1.5$ Å, $\varepsilon_S = 80$, $\varepsilon_P = 1$ and $L_z = 20\lambda_D$.

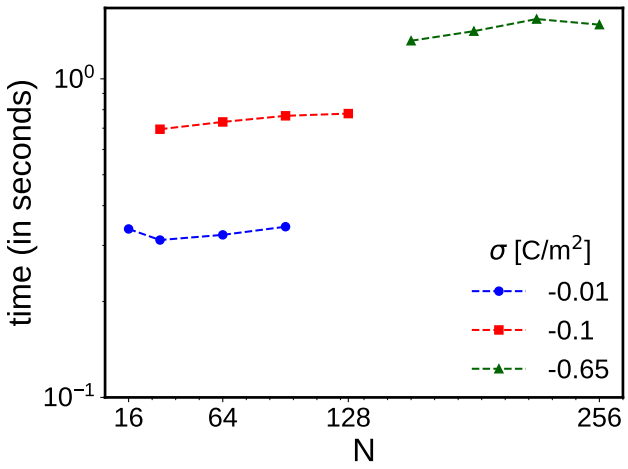

Figure 2.4: Execution time (in seconds) averaged over 10 instances for solving $\hat{G}(s = 0.0084, z, z)$ for a single charged plate system for low, medium and high surface charge densities. $q_+ = 2$, $q_- = 1$, $c_\mathrm{b} = 0.1$ M, $a_{\pm,s} = 1.5$ Å, $\varepsilon_\mathrm{S} = 80$, $\varepsilon_\mathrm{P} = 1$ and $L_\mathrm{z} = 20\lambda_\mathrm{D}$.

to the existing finite-difference based approach by Xu and Maggs[105] which only gives stable solutions for very low σ values, shows first order convergence and is only able to achieve errors as low as 10^{-3} even with a thousand grid points. With our new method, we are able to reduce errors to 10^{-7} with less than 100 points for low σ values such as -0.01 C/m^2. Most importantly, this enhanced accuracy is not accompanied by any additional computational time and in fact resolves the correlation function in less time than the method of Xu and Maggs. Figure 2.4 plots execution time with increasing N for the evaluation of $\hat{G}(s = 0.0084, z, z)$ averaged over 10 instances for the three σ values. $s = 0.0084$ was chosen for this plot as the calculations were slowest for this value. Unlike, Xu and Maggs' method, where the execution time linearly increases with N, the execution times in our method remain almost constant with the additional advantage of extremely high accuracy. The absolute time values are very similar to Xu and Maggs' method where also evaluation of $\hat{G}$ for low σ values requires time of the order of 0.1 sec. Note that our time calculations were done on 1.7 GHz Intel 8-core processor compared to relatively faster 2.67 GHz Intel 8-core processor used by Xu and Maggs.

Furthermore, using our method we were also able to perform stable calculations for complex features like oscillations in electrostatic potential and ion concentration profiles. Figure 2.5a plots $\psi(z)$ for the case of 3:1 salt in contact with a negatively charged surface with $\sigma = -0.15$ C/m^2 and $N = 1024$. For the chosen salt concentration and ion sizes, $\psi(z)$ shows prominent oscillations which decay with increasing distance from the surface. Increasing the value of L_z does not lead to any change in the profiles proving that oscillations are real physical features and not artifacts of the numerical method. In Figure 2.5b, we plot E_surf and E_profile as a function of N for the case of $L_\mathrm{z} = 30\lambda_\mathrm{D}$. As in the previous case of

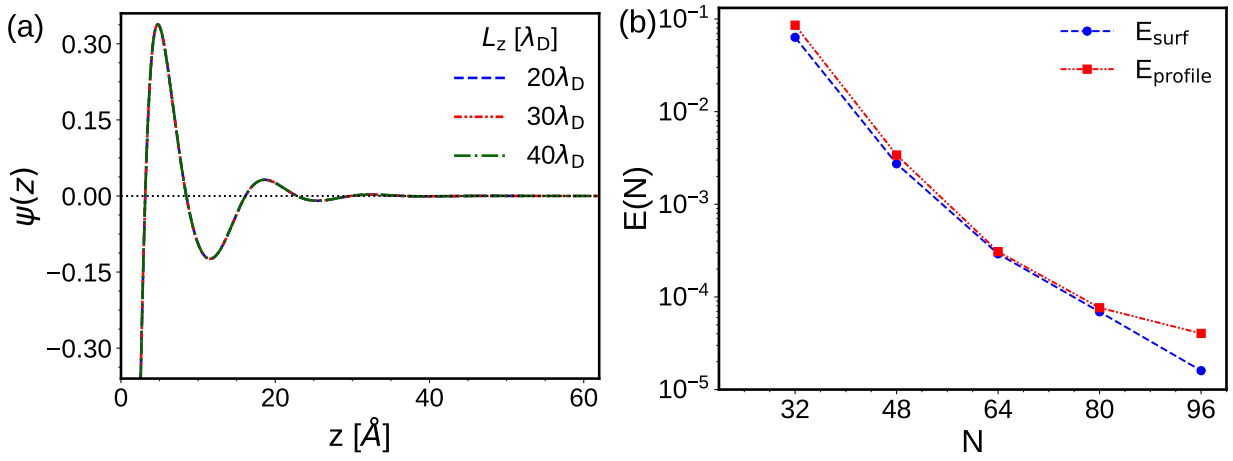

Figure 2.5: a) Oscillating electrostatic potential $\psi(z)$ profile for a single charged plate system, $N = 1024$. b) L_2 norm of the error in the surface electrostatic potential (E_{surf}) and electrostatic potential profile ($E_{profile}$) as a function of number of spectral modes. $\sigma = -0.15$ C/m^2, $q_+ = 3$, $q_- = 1$, $c_b = 0.5$ M, $a_{\pm,s} = 2.1$ Å, $\varepsilon_S = 80$, $\varepsilon_P = 1$ and $L_z = 30\lambda_D$.

2:1 salt, here also we are able to reduce errors to 10^{-5} with less than 100 spectral modes and only 24 quadrature points for numerical integration of Equation 2.60. However, unlike divalent salts here we are not able to achieve perfect spectral convergence. One reason for this could be the fact that in order to calculate self-energy with reasonable accuracy the cutoff value S for the integral in Equation 2.60 was set to be 1000. This high value of S affects the series convergence properties of the Legendre-Gauss quadrature method which in turn interferes with the spectral convergence property of the entire numerical algorithm.

2.7.2 Two charged surfaces separated by a salt solution

For this case as well, we study three different systems with two charged plates located at $z = 0$ and $z = L_z$ and surface charge densities $\{\sigma_1, \sigma_2\} = \{(-0.01, 0.02), (-0.1, 0.2), (-0.5, 1.0)\}$ C/m^2 in contact with 0.5 M divalent salt solution, $q_+ = 2$ and $q_- = 1$, and $a_\pm = 1.5$ Å. These three pairs of surface charge densities correspond to weak, moderate and strong electrostatic coupling regimes, respectively. The dielectric constant in the region $z > 0$ and $z < h$ is taken to be that of water, $\epsilon_s = 80$, whereas the dielectric constant in the region $z < 0$ and $z > h$ is set to be $\epsilon_p = 1$. Here again, for the numerical calculation of the self-energy via the integral in Eq. 2.60, we used a cutoff value of $S = 32$ and a total of 24 quadrature points. The tolerance parameter δ for all the Newton solvers was set to 10^{-7} and the initial guesses for electrostatic potential $\psi(z)$ and counterion concentration profiles $c^{2+}(z)$ were taken to be the solutions of the non-linear mean-field Poisson-Boltzmann equations. To ensure stability we made the conservative choice of setting the mixing ratio m to 0.1 for all three surface

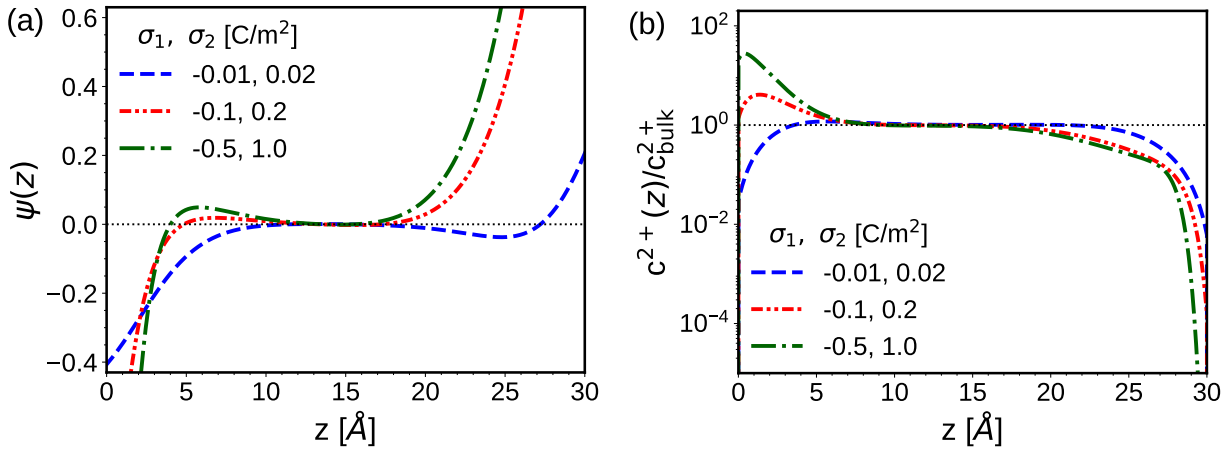

Figure 2.6: a) Electrostatic potential $\psi(z)$ profile and b) counterion concentration profile $c^{2+}(z)$ with respect to bulk for the three pairs of surface charge densities for the two plate system. $q_+ = 2$, $q_- = 1$, $c_\mathrm{b} = 0.5$ M, $a_{\pm,s} = 1.5$ Å, $L_\mathrm{z} = 30$ Å, $\varepsilon_\mathrm{S} = 80$, $\varepsilon_\mathrm{P} = 1$ and $N = 1024$.

charge densities. However, as for the case of single charged plate systems, for low σ values, $m = 1$ also gives stable iterations.

Representative $\psi(z)$ and $c^{2+}(z)$ profiles for $N = 1024$ and the domain size $L_\mathrm{z} = 30$ Å, are plotted in Figure 2.6. Next, we study the rate of convergence of these profiles with number of spectral modes N using the following two error metrics

$$E_\mathrm{surf}(N) = \sqrt{\sum_{i=0}^{1}[\psi(N, z = iL_\mathrm{z}) - \psi(N^\mathrm{ref} = 1024, z = iL_\mathrm{z})]} \tag{2.115}$$

$$E_\mathrm{profile}(N) = \sqrt{\sum_{i=1}^{9}[\psi(N, z = \frac{2i+1}{20}L_\mathrm{z}) - \psi(N^\mathrm{ref} = 1024, z = \frac{2i+1}{20}L_\mathrm{z})]} \tag{2.116}$$

where E_surf measures error in electrostatic potential on the two surfaces and E_profile measures error in electrostatic potential profile in the interface. The semi-log plots of these two error metrics as a function of N are plotted in Figure 2.7. For all three pair of σ values the logarithm of these errors linearly (or higher) decreases with N, proving spectral rate of convergence of the algorithm for two plate system as well. Note that unlike one-plate system here small value of $N = 40$ also gives stable calculation of the double layer profile for $\{\sigma_1, \sigma_2\} = \{-0.5, 1.0\}$ C/m^2. As in this case we do not need approximate the infinite interface with a finite domain length the stability of the algorithm is found to be better than single plate case analysed in the previous subsection. Similar to one plate system, this

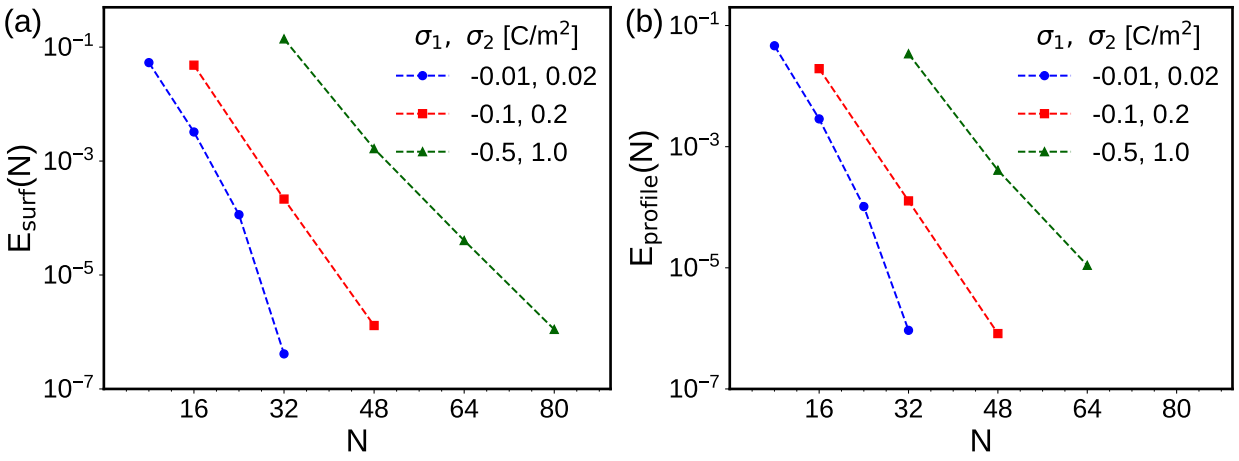

Figure 2.7: L_2 norm of the error in the a) surface electrostatic potential (E_{surf}) and b) electrostatic potential profile ($E_{profile}$) as a function of number of spectral modes for the three pairs of surface charge densities for the two plate system. $q_+ = 2$, $q_- = 1$, $c_b = 0.5$ M, $a_{\pm,s} = 1.5$ Å, $L_z = 30$ Å, $\varepsilon_S = 80$, $\varepsilon_P = 1$ and $N = 1024$.

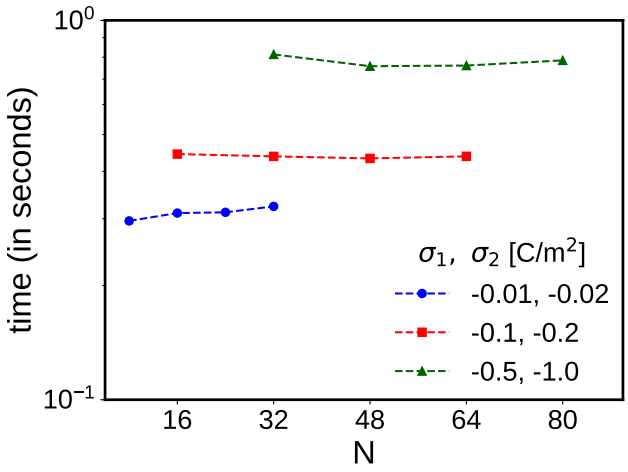

Figure 2.8: Execution time (in seconds) averaged over 10 instances for solving $\hat{G}(s = 0.0084, z, z)$ for three pairs of surface charge densities for the two plate system. $q_+ = 2$, $q_- = 1$, $c_b = 0.5$ M, $a_{\pm,s} = 1.5$ Å, $L_z = 30$ Å, $\varepsilon_S = 80$ and $\varepsilon_P = 1$.

enhanced accuracy does not require any additional computational time and the execution times for evaluation of $\hat{G}(s = 0.0084, z, z)$ remains almost constant with N. Figure 2.4 plots these execution times with increasing N for the three pairs of σ values.

2.7.3 Vapor-liquid interface in ionic fluids

Figure 2.9 shows electrostatic potential profile $\psi(z)$ (solid lines), net charge distribution $\rho(z)$ and ion concentration profiles for the case of the interface between high density 'liquid' and low density 'gas' phase for a divalent salt, $q_+ = 2$, $q_- = 1$, and $a_\pm = 1.5$ Å, at $T/T_c = 0.9$, where T_c is the critical temperature for the phase coexistence curve. A total of $N = 4096$ spectral modes were used to solve the equations for a solution domain with $L_z = 10\lambda_v + 20\lambda_l$, where λ_v and λ_l are Debye-Hückel lengths in the vapor and liquid phases, respectively. As mentioned previously, Debye-Hückel lengths are the characteristic decay length-scale of the interface, hence this domain size was found to be sufficient to capture the interface completely. However, due to the highly anisotropic ionic cloud on the two sides of the interface resulting from the significant difference in ion concentrations between the two bulk phases, this case is the most challenging to numerically simulate. Therefore, in order to calculate self-energy accurately a cutoff value of $S = 10^6$ and a total of 24 quadrature points were needed. Finally, the tolerance parameter δ for all the Newton solvers was set to 10^{-5} and the mixing ratio m was taken to be 0.1.

Next, to study error convergence with spectral modes, we define $E_{\text{profile}}(N)$ as

$$E_{\text{profile}}(N) = \sqrt{\sum_{i=0}^{10} [\psi(N, z = \frac{i}{10} L_z) - \psi(N^{\text{ref}} = 4096, z = \frac{i}{10} L_z)]} \tag{2.117}$$

The semi-log plot of $E_{\text{profile}}(N)$ as a function of N are plotted in Figure 2.10. Although our method is stable and the error progressively reduces with N, to reduce the error below 10^{-7}, at least 500 spectral modes are needed, compared to less than 100 modes needed for the previous two cases. The slower convergence could be attributed to the very high value of S needed to calculate the self-energy. As discussed before, this affects the series convergence properties of the Legendre-Gauss quadrature method, which in turn interferes with the spectral convergence property of the entire numerical algorithm.

2.8 Summary

We have modified the Gaussian Renormalized Fluctuation theory by including the excluded volume effect of ions and solvent molecules, and decomposing the electrostatic correlation function into a short-range contribution associated with the local electrostatic environment and a long-range contribution accounting for the spatially varying ionic strength and dielectric permittivity. For most electrical double layers, the double-layer length scale is much larger than the ion size due to the long-range nature of Coulombic interactions, allowing

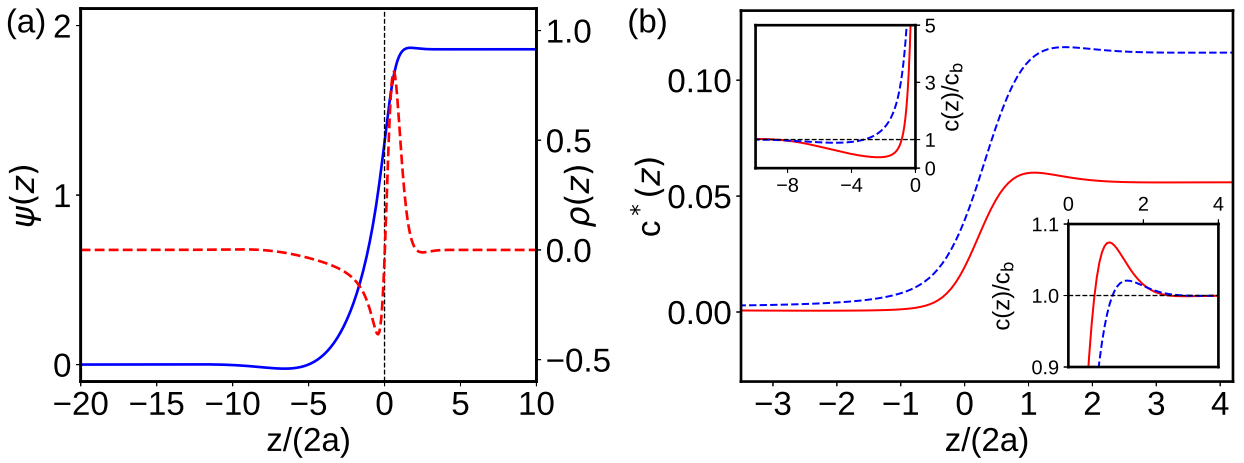

Figure 2.9: Structure of a vapor-liquid interface for a divalent salt, $T/T_c = 0.9$, $q_+ = 2$, $q_- = 1$, $a_\pm = 2$ Å, $L_z = 10\lambda_v + 20\lambda_l$, $\varepsilon_S = 80$, and $N = 4096$. a) Electrostatic potential profile $\psi(z)$ (solid lines) and net charge distribution $\rho(z)$ (dashed lines). The vertical dotted line denotes the point of zero charge. c) Cation (solid) and anion (dashed) concentration profiles, $c^* = c(2a)^3$. The insets enlarge the double layer structure on the two sides of the interface, ion concentrations are plotted relative to their respective bulk values.

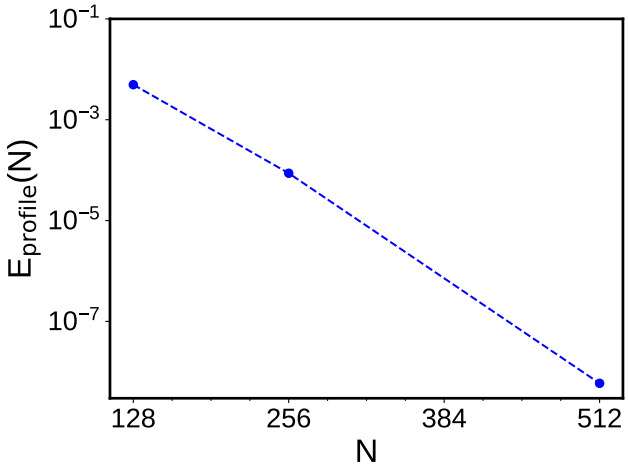

Figure 2.10: L_2 norm of the error in the electrostatic potential profile $E_{profile}$ as a function of number of spectral modes for the vapor-liquid interface system. $q_+ = 2$, $q_- = 1$, $a_{\pm,s} = 2$ Å, $L_z = 10\lambda_v + 20\lambda_l$, and $\varepsilon_S = 80$.

us to separate the two length scales. We also describe in detail a three-level iterative algorithm to solve the resultant equations in symmetric geometries. Additionally, we discuss a new Sturm-Liouville theory-inspired approach developed here for calculating the electrostatic correlation function G. This method analytically handles the Dirac delta function in the differential equation of G, allowing us to employ highly efficient spectral methods. We demonstrate the spectral convergence property of our algorithm for the case of one charged plate system, a two-plate system, and a vapor-liquid interface in ionic fluids. The results presented in the subsequent chapters are calculated using this algorithm. The code for the algorithm is available at https://github.com/nikhil0165 under GPL-3.0 license. The repository name for one charged plate system (Section 2.5.4.1) is one_plate_mgrf, for two charged plates separated by salt solution (Section 2.5.4.2) is two_plates_mgrf, and for the system of vapor-liquid interface in ionic fluids (Section 2.5.4.3) is vapor_liquid_mgrf. A major advantage of using Dedalus is its ability to solve NLBVPs not only in Cartesian but also in cylindrical as well as spherical coordinate systems. This algorithm and the attached codes establish a platform from which one can extend the development of codes for the Modified Gaussian Renormalized Fluctuation Theory beyond symmetric planar geometries.

Chapter 3

Vapor-Liquid interface in ionic fluids

3.1 Introduction

A classic example where the spatially varying ion-ion correlations play the dominant role is the vapor-liquid interface in ionic fluids. Since the pioneering experimental work by Buback and Franck[111], it has been well recognized that ionic salts exhibit two-phase coexistence below a certain critical temperature[112, 113]. Analogous to vapor-liquid phase equilibrium in real gases, ionic salts dissolved in a solvent can also undergo phase separation into a high ion density 'liquid' and a low density 'vapor' phase because of ion-ion correlations. This coexistence has also been predicted by theories, and molecular simulations, where both the phase boundary and criticality have been reasonably captured [29, 76–79]. Despite the progress in explaining the bulk thermodynamics, the interfacial behavior remain less addressed to our knowledge. Bresme and coworkers[80–82] performed molecular simulations to study the interface of ionic fluids, including the density profile and surface tension. However, it is difficult to apply simulation methods away from the critical temperature due to the very low density of the vapor phase. On the theory side, two main methods have been invoked to model this vapor-liquid interface: non-local density functional theory[114–116] and the square-gradient theory[117–119]. These approaches describe the ion-ion correlation in the inhomogeneous interfacial region using a functional form based on the bulk correlation function. In the density functional theory, the choice of the density to evaluate the local correlation is *ad hoc*[63, 114], which prevents its generalization to different systems. Whereas in the square-gradient approach, truncating the expansion of the free energy at the square-gradient level limits the applicability of this method only to systems where the concentration deviation from the bulk is small. The theory thus cannot be used to describe interfaces away from the critical point. Furthermore, none of the existing theories have been applied to systems where the cations and anions are not symmetric, either in terms of valency or ionic size. The asymmetry leads to an interphase electrostatic potential (Galvani potential) and local charge separation across the interface[76, 81], which increases the complexity of both the physics and numerical solution. This gap in our understanding is a serious issue considering how

ubiquitous asymmetric electrolytes are. Therefore, a self-consistent and non-perturbative theory to describe the electrostatics at the vapor-liquid interface is necessary.

To accurately quantify the inhomogeneity of ion-ion correlation is a great challenge majorly for the following two reasons. First, the correlation function needs to be resolved at two very different length scales, one associated with ion size (short-range) and the other with interfacial thickness (long-range). Second, the ionic cloud is highly anisotropic on the two sides of the interface due to the huge difference in ion concentration between the two bulk phases. These two features have not been correctly captured in previous theoretical work because of the mathematical approximations involved. In this chapter, we apply our modified Gaussian renormalized fluctuation theory[41, 75, 120] to model the vapor-liquid interface for both symmetric and asymmetric ionic salts.

3.2 Results and Discussion

We consider a system of an ionic salt with cations of valency q_+, born radius a_+, and anions of valency q_-, born radius a_- dissolved in a solvent with a constant dielectric permittivity ϵ. A constant ϵ facilitates the quantitative comparison with molecular simulations performed using the primitive model. The concentrations of the coexisting phases and the Galvani potential difference $\Delta\psi_G$ can be obtained by equalizing the chemical potentials and the pressure in the two bulk phases. The corresponding equations are Eq. 2.21, 2.22, 2.17 and 2.26 given in Section 2.3. Here without loss of generality, we have taken the potential of the vapor phase to be zero and the potential of the liquid phase to be ψ_G. The structure and properties of the interface are calculated from equations 2.40 - 2.46.

3.2.1 Symmetric salts

We start with the bulk thermodynamics of symmetric salt, where $q_+ = q_- = 2$ and $a_+ = a_- = a$. Figure 3.1 plots the phase diagram of the vapor-liquid equilibrium in terms of reduced temperature T/T_c where T_c is the critical temperature. By accounting for the finite charge spread on the ion, our theory predicts a much broader coexistence envelope compared to the point-charge Debye-Hückel (DH) theory and is in quantitative agreement with three independent sets of simulation data[78, 80, 121]. In the homogeneous bulk, the self-energy only contains the short-range component $u_{\pm,s}$, which depends on the details of the ion. Our results highlight the necessity of including the finite charge spread to accurately capture the short-range correlation. The short-range correlation thus also becomes a prerequisite to modeling the correlations in the interface. It should be noted that in Figure 3.1, the comparison is made at the same distance from the critical point. It is well recognized that fluctuation theories at the Gaussian level cannot accurately capture the critical point, a feature that is only possible to be reproduced through renormalization-group calculations[29, 113].

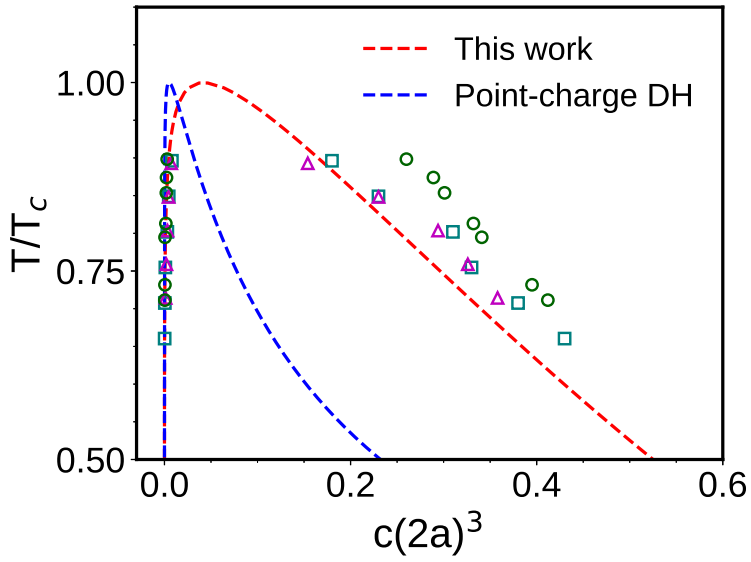

Figure 3.1: Phase diagram of liquid-vapor coexistence in symmetric ionic fluids plotted using reduced temperature (T/T_c) and scaled total concentration of ions $c(2a)^3$. The lines represent theoretical predictions in comparison with the simulation data from González-Melchor et al.[80](circles), Orkoulas et al.[122] (squares), and Caillol et al.[121] (triangles).

By resolving the correlation function at both short and long rafnges, we can calculate the interfacial ion concentration profile between the two coexisting bulk phases. The concentration profiles for different values of T/T_c are shown in Figure 3.2a. The profiles are shifted to have the same position of the Gibbs dividing surface (GDS). Including the long-range correlation effect is essential for capturing the continuous change in concentration from vapor to liquid. This diffused interface cannot even be created by theories that only include the local correlation. The importance of the long-range effect is also illustrated by the interfacial width on the two sides of the GDS for the ionic species, as shown in the inset of Figure 3.2a. As the critical temperature is approached, the interfacial width on both sides increases and eventually diverges at the critical concentration, which is consistent with the divergence of the correlation length at the critical point as predicted by Lee and Fisher[119]. Furthermore, the concentration dependence of the interfacial width on vapor-side δ_v is counter-intuitive. As the concentration in the vapor phase increases, its bulk correlation length (analogous to Debye screening length) decreases, which is expected to shorten δ_v. The increase of δ_v predicted by our theory is a result of the long-range correlation effect from the bulk liquid phase to the vapor side. The two sides of the interface interfere with each other due to this long-range effect.

Our theory also quantitatively captures the interfacial properties of the vapor-liquid interface. Figure 3.2b shows remarkable agreement of interfacial tension between our calculations and the simulation results from González-Melchor et al.[82]. The quantitative agreement of

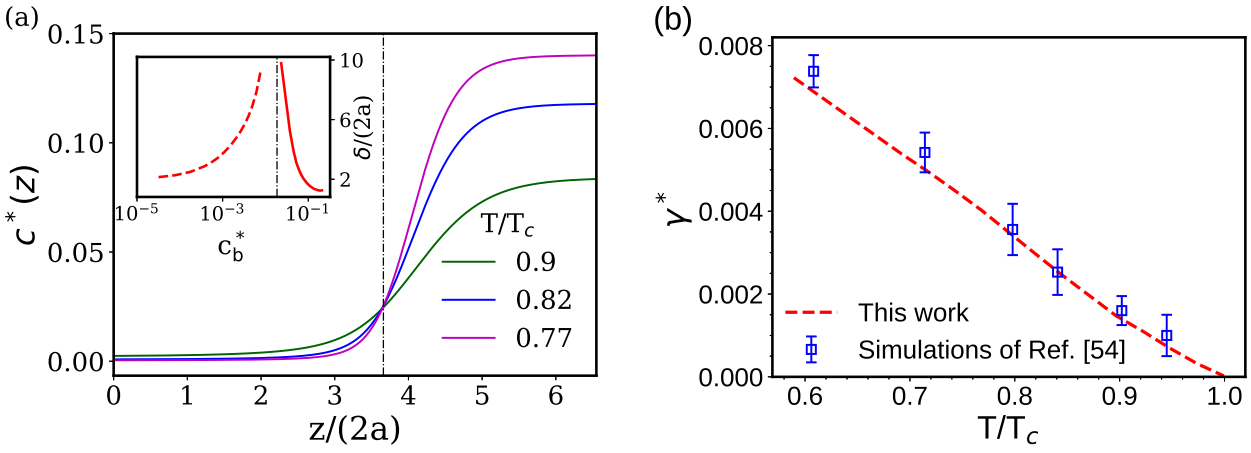

Figure 3.2: Interfacial structure and properties for a symmetric salt, $\epsilon = 80$. a) Ion concentration $c^* = c(2a)^3$ profiles for different T/T_c with vertical dashed-dot line denoting the Gibbs dividing surface. The inset plots the interfacial width on the vapor (dashed) and liquid side (solid) of the interface against the ion concentration in the corresponding bulk (c_b^*). b) Non-dimensional surface tension $\gamma^* = \gamma 4\pi\varepsilon(2a)^3/(q_+q_-e^2)$ as a function of the reduced temperature T/T_c predicted by our theory in comparison with simulations of González-Melchor et al.[82].

both the phase coexistence curve and the interfacial tension for a wide range of temperatures validates the ability of our theory to accurately model interfaces with large interfacial inhomogeneities. For the same vapor-liquid interface, non-local density functional approaches have been found to overestimate interfacial tension values by a factor of three[114]. Our method is also superior to the square gradient theory-based approaches, which are only valid close to the critical temperature. The non-perturbative nature of our method allows us to capture inhomogeneous correlation beyond the square gradient level and thus guarantees its applicability to a variety of interfacial systems with steep concentration gradients.

3.2.2 Asymmetric salts

The modified Poisson-Boltzmann form of our equations enables us to conveniently include electrostatic potential and ion-ion correlations in a unified framework. For the case of asymmetric salts, where cation and anion have different valencies or ion sizes, the difference in their self-energies leads to local charge separation and an electrostatic potential profile across the interface. Here, we provide the first theoretical prediction of interfacial structure for a 2:1 ($q_+ : q_-$) salt. Figure 3.3a shows the Galvani potential $\Delta\psi_G$ predicted by our theory, in good agreement with the simulation results reported in literature[81]. The electrostatic potential profile and the net charge distribution are plotted in Figure 3.3b. As the potential

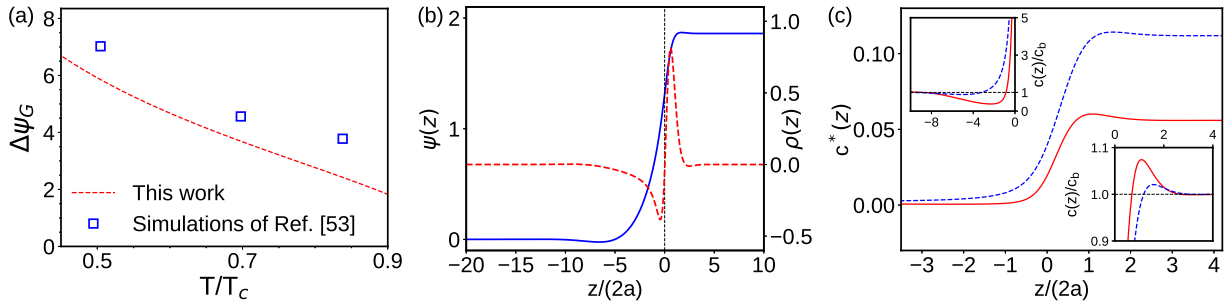

Figure 3.3: Interfacial structure for a 2:1 ($q_+ : q_-$) asymmetric salt a) Theoretical predictions of Galvani potential $\Delta\psi_G$ in comparison with simulation data from Ref. [81] b) Electrostatic potential profile $\psi(z)$ (solid lines) and net charge distribution $\rho(z)$ (dashed lines). The vertical dotted line denotes the point of zero charge. c) Cation (solid) and anion (dashed) concentration profiles, $c^* = c(2a)^3$. The insets enlarge the double layer structure on the two sides of the interface, ion concentrations are plotted relative to their respective bulk values. $T/T_c = 0.9$ for b and c.

changes from 0 in the vapor phase to a finite value in the liquid phase, its curvature and hence the net charge is forced to change sign at some intermediate point. Net positive and negative charges accumulate on the liquid and vapor sides, respectively. The two sides of the interface behave as charged objects with equal and opposite charges, essentially acting as double layers to each other. This dual double layer structure can be more clearly seen in the ion distribution in Figure 3.3c. On the vapor side, the net charge is negative and the electrostatic potential and ion distribution are similar to electrolyte solutions in contact with a positively charged surface. The left inset shows the depletion of cations compared to the bulk value, whereas anions are enriched. On the other hand, local excess of cations over anions can be seen in the right inset, as expected for a double layer next to a negatively charged surface. Similar self-energy-induced charge separation can also be observed in other interfaces, such as two immiscible fluids[123, 124] or micro-phase separated block copolymers[14, 125].

In Figure 3.3c, it is worth noting that concentrations of both cations and anions on the liquid side are larger than their corresponding bulk values. This prediction can be explained by the strong correlation effect in the liquid phase. Similar counter-intuitive enrichment of cations is not expected on the vapor side due to its low ion densities. The cooperative enrichment of both counterions and coions is critical to explaining the phenomena of charge inversion in electrical double layers[120]. The over-accumulation of multivalent counterions next to the charged surface is stabilized by the presence of an excess amount of coions.

3.3 Summary

The Modified Gaussian Renormalized Fluctuation Theory and the decomposition method for the correlation function provide essential improvements over existing methods to model the vapor-liquid interface. The correlation function is decoupled into a short-range contribution associated with the local electrostatic environment and a long-range contribution accounting for the spatially varying ionic strength across the interface between the two bulk phases. The non-perturbative and self-consistent nature of the theory allows the description of bulk thermodynamics and interface in a wide range of temperatures. A finite charge spread on the ion is necessary to accurately describe the short-range correlation and hence the vapor-liquid coexistence curve. Including the long-range correlation effect is essential for generating a continuous concentration profile across the interface. The resulting interfacial tension predicted by our theory is in quantitative agreement with simulation data for symmetric salts. We also provide the first theoretical prediction of the interface for an asymmetric salt, where the difference in ion correlation between cations and anions leads to an electrostatic potential profile and local charge separation on both the vapor and liquid sides of the interface. The ion distribution profiles on each side of the interface resemble an electrical double layer next to a charged surface. Because of high ion densities in the double layer on the liquid side, a cooperative enrichment of both counterions and coions is predicted.

Chapter 4

Overcharging and charge inversion in electrical double layers

4.1 Introduction

One long-standing puzzle beyond the scope of the mean-field Poisson-Boltzmann (PB) theory is the over-accumulation of counterions in the electrical double layer (EDL), known as overcharging [31, 44, 83]. To understand overcharging, we first need to revisit the structure of a typical EDL in the context of electrokinetic flows, where electrokinetic flows refer to the motion of ions and the surrounding fluid as a result of a pressure drop, an electric field, or an electrochemical potential gradient. The structure of EDL can be divided into two main regions[2]. The first is the stagnant or stern layer, where the ions are strongly bound to the surface and cannot move upon applying a force. The second region is the diffuse layer, where the ions are free to move. Typically, the diffuse part of the EDL is dominated by counterions, giving it a net opposite charge to that of the surface[4]. Thus, for a negatively charged surface, the direction of electrokinetic flow aligns with the applied force. However, in some systems, there is an over-accumulation of counterions near the surface, a phenomenon known as the overcharging of the EDL[83, 126]. To ensure charge neutrality, this over-accumulation leads to a reversal in the sign of the net charge in the diffuse layer. Furthermore, if the extent of this over-accumulation is significant enough, depending on the fluid properties, there could be an inversion in the direction of electrokinetic flows, a phenomenon known as charge inversion [30, 43, 44, 127–129]. For example, when a pressure gradient is applied to the salt solution inside a charged nanochannel, the resulting ionic current, also known as streaming current, can invert its direction[30]. Similarly, when an electric field is applied to a suspension of charged colloids, the overcharging of EDL can lead to a reversal in the sign of the electrophoretic mobility of the colloidal particles[43, 127]. Understanding the physics of overcharging and charge inversion is crucial as these two phenomena are relevant to the design of modern nanodevices and various biophysical processes[20, 128, 130–134]. Localized charge inversion has proven to be crucial in the functioning of nanofluidic devices such as ionic

diodes and rectifiers[128, 130]. The reversal of electrophoretic mobility offers a promising avenue for the development of innovative DNA sequencing methodologies[131, 132]. Furthermore, overcharging plays a vital role in the formation of chromatin; for instance, the amount of DNA wrapping around positive histone proteins in a nucleosome exceeds the requirements of charge neutrality by a significant margin[135]. Therefore, it is desirable to develop a self-consistent and numerically solvable approach to model these phenomena.

There are two main driving forces for the over-accumulation of counterions: the presence of specific chemical interactions between counterions and the charged surface, and strong electrostatic correlations between ions [136, 137]. In any system, both these driving forces together contribute to over-accumulation, however, their relative contribution depends on the counterion valency. For monovalent salts, the strength of electrostatic correlations is very weak, and molecular simulations have shown that overcharging cannot occur in room temperature water in the absence of specific chemical interactions[83]. In the case of divalent counterions, Kubíčková et al.[83] performed Monte Carlo simulations using only coulombic pair potentials and hard-sphere interactions, and showed that ion correlations are strong enough to cause overcharging of EDL. However, these simulations could not observe any reversal in the sign of electrophoretic mobilities for practical values of surface charge densities [42, 43, 83]. This implies that both specific interactions and ion correlations are necessary to explain experimentally observed charge inversion in divalent electrolytes [136]. For counterions with valency three and higher, unless the surface is highly reactive, both experiments[31] and simulations[83] have shown that ion correlations are the dominant factor in determining the strength of charge inversion. Besteman et al.[31] found that for trivalent salts next to a silica surface, the critical salt concentration at which charge inversion occurs is not sensitive to the chemical identity of the ions. Hence, pure electrostatic-based modeling should be able to capture charge inversion in trivalent salts, whereas to fully capture charge inversion in divalent salts one needs to include both specific interactions and electrostatics in the model.

Experiments and simulations have extensively studied overcharging and charge inversion in the last few decades. Multiple studies show a continuous transition from a normal double layer to an overcharged double layer as surface charge increases[138–140]. Continuously increasing surface charge slows down overcharging and eventually leads to ionic crowding at the surface[53, 138, 141]. Furthermore, simulations show ionic layering and oscillation of electrostatic potential in the so-called strong-coupling condition of high surface charge and high valency[83, 126, 142, 143]. The effect of salt concentration on charge inversion is rather non-trivial and shows a non-monotonic change in the magnitude of the inverted mobility and ionic current. [30, 43, 144]. Van der Heyden et al. [30] measured the streaming current inside silica nanochannels and found that in the low salt concentration regime, increasing trivalent salt concentration reverses the direction of the current. However, with a further increase in concentration, the magnitude of the inverted current reaches a maximum and gets suppressed at high salt concentrations. Furthermore, in the case of multivalent and monovalent salt mixtures, which are highly relevant to biological and geological conditions, both experiments [30, 128] and simulations [145, 146] showed that the addition of monovalent salt cancels charge inversion. The magnitude of the inverted streaming current was also found

to behave non-monotonically with the addition of monovalent salt[30, 128].

The above-mentioned non-monotonic salt concentration dependence of charge inversion has also been confirmed by experiments and simulations on the electrophoretic mobilities of charged colloidal particles [144, 147]. In the experiments of Martín-Molina et al.[147], the magnitude of inverted mobility for a negatively charged latex particle was found to reach a maximum followed by a drop with increasing Lanthanum ion concentration. To further understand the these non-monotonic trends and decouple the effects of hydrodynamics and EDL structure, Hsiao and Luijten [144] performed Langevin dynamics simulations for polyelectrolytes and calculated the drift velocities resulting from the applied electric field. Their simulations also showed a non-monotonic dependence of the inverted velocity on multivalent ion concentration, which proves that the EDL structure is responsible for the suppression of charge inversion at high salt concentrations. However, the details of the EDL structure and its relationship with the non-monotonic nature of inverted electrokinetic flows remain unknown.

Theoretical studies are necessary to provide important insight into the structure and properties of electrical double layers. Unfortunately, the classical PB theory cannot even qualitatively capture the phenomena of overcharging and charge inversion as it does not account for ion-ion correlations. Hence, over the years, a number of theories have been proposed to go beyond mean-field PB[44, 45, 47–62]. One of the most famous works in this regard is the Strongly Correlated Liquid (SCL) theory developed by Shklovskii and coworkers [44, 52, 68, 148]. Inspired by one-component plasma physics, Perel and Shklovskii assumed the presence of a high-density two-dimensional condensed layer of counterions on the charged surface existing in the form of a Wigner crystal (WC) lattice. SCL essentially invokes a two-state model where this WC lattice at the surface is in equilibrium with a second diffuse double layer described by mean-field PB. This SCL theory was applied to many systems consisting of charged polymers, membranes, and colloids[149, 150]. Moreira and Netz[151] made corrections to the SCL theory by performing a perturbative expansion and compared the theoretical results with Monte-Carlo simulations. The WC picture is exact in the strong coupling limit and is able to predict inversion in ionic current and electrophoretic mobility with increasing multivalent salt. However, it fails to capture the onset of the ion condensation, hence missing the transition from the normal double layer to the overcharged double layer that occurs in the intermediate coupling regime. Furthermore, because the ion-ion correlation and the excluded volume effect in the diffuse layer have not been included, the SCL theory fails to capture the following key experimental observations. It predicts that the charge inversion will be monotonically enhanced by increasing the concentration of multivalent counterions, which cannot explain the non-monotonic dependence of charge inversion on salt concentration observed in experiments and simulations [30, 144, 147]. Its prediction of giant charge inversion [148] in the mixture of multivalent and monovalent electrolytes also contradicts experimental observations of reduction in the strength of charge inversion as monovalent salts are added[30, 145, 146].

To capture ion condensation and the continuous transition from normal to overcharge double layer, Lau [52] developed a perturbative theory with a one-loop correction of the

electrostatic potential. Bazant and coworkers[53, 69, 143] constructed a phenomenological free energy expression by writing the correlation contribution in terms of gradients of electrostatic potential and an associated correlation length parameter. Gupta et al.[50] added a screening potential to the Boltzmann factor to account for ion correlations. This screening potential was also expressed in terms of the electrostatic potential gradient but without any phenomenological parameter. While all these models could predict the excess accumulation of counterions on the surface and the subsequent charge inversion, similar to the SCL theory, they cannot capture the non-monotonic dependence of the charge inversion on multivalent ion concentration. Lau's point charge model overestimates ion correlations and does not include the excluded volume effects of ions and solvent molecules, thus permitting unlimited accumulation of counterions at the surface and a monotonic growth in charge inversion with salt concentration. For the models of Bazant et al. and Gupta et al., although excluded volume effects have been included, the gradient of electrostatic potential vanishes in bulk and thus these models were unable to capture any correlation contribution to the bulk free energy. As the interface and bulk are in equilibrium, these theories fail to capture the spatially varying ion correlation coherently. The incorrect description of the bulk leads to an inaccurate description of the interface.

A more rigorous way to formulate electrostatic correlations is to use the Ornstein-Zernike correlation formalism as in Integral equation-based theories (IET) and classical density functional theories (DFT)[34–36, 42, 43, 46, 54, 152, 153]. To our knowledge, no existing IET approach has successfully described the decrease in Zeta potential ψ_ζ (equivalently diffuse plane potential) at high salt concentrations. Martín-Molina et al.[42, 43] used the hypernetted-chain closure (HNC) for the correlation between ions and the charged colloidal particle and the mean-spherical approximation (MSA) closure to model the ion-ion correlations. To solve the problem in a numerically tractable manner, the functional form of the ion-ion correlation in the inhomogeneous interface was approximated to be the same as in the bulk. While their work predicts an inversion in the sign of electrophoretic mobility, it was unsuccessful in capturing its non-monotonic change with salt concentration. In addition to the approximation used to calculate ion-ion correlation, another issue is the implicit treatment of solvent molecules which ignores their excluded volume and thus could lead to an overestimation of the accumulation of counterions near the charged surface. Gillespie et al. [54] successfully captured the non-monotonic inversion of ionic current in pure multivalent salts using a density functional theory (DFT) based approach. However, DFT-based approaches rely on perturbing the free energy around a chosen reference ion concentration profile. These profiles are determined by density weighting functions that are tailored to a specific system, making them less adaptable to other correlation-induced phenomena. Such weighting functions also lead to a lack of a physically intuitive description of the electrical double layer[63, 65]. In general, the integral nature of equations in these two models makes the solution procedure computationally challenging[154, 155].

The most challenging task in modeling overcharged EDLs is to accurately and simultaneously account for the inhomogeneous ion-ion correlation and the excluded volume effect of molecules in the EDL. When charge inversion occurs, the correlations are significantly

enhanced at the surface, making it computationally difficult to model the steep change in correlations from the surface to the bulk. In this chapter, we apply the Modified Gaussian Renormalized Fluctuation Theory to study EDLs next to planar surfaces and account for both short-range and long-range features of electrostatic correlations. This way we self-consistently include the spatially varying correlations, image charge effect, and excluded volumes in a numerically tractable unified framework. The nature of overcharging and charge inversion with respect to surface charge, counterion valency, salt concentration, the addition of monovalent counterions, and dielectric contrast is revealed. The predictions of our theory are in good agreement with experiments and simulation results. Theoretical predictions are compared with the experimental measurements of streaming currents[30] and electrophoretic mobility[42] to elucidate the relative contributions of the inhomogeneous ion-ion correlations and excluded volume effects towards the non-monotonic behavior of the inverted electrokinetic flow. Comparisons with the existing theories in literature are also provided to highlight the accuracy of our theory.

4.2 Results and Discussion

In this chapter, we study overcharging and charge inversion in the case of a negatively charged surface σ in contact with an aqueous electrolyte solution. The charged surface is positioned at $z = 0$ and the salt solution is confined to the region $z > 0$. Although, the equations 2.40 - 2.45 derived in Sections 2.4 and 2.5 can account for local dielectric variations, for simplicity, we solve for the case of the primitive model of electrolytes. $\varepsilon(z)$ is taken to be a step function with the value ε_{P} for $z < 0$ and $\varepsilon_{\mathrm{S}} = 80$ for $z > 0$. Here, the focus is on the effect of surface charge density, counterion valency, salt concentration, and dielectric contrast. Therefore, q_- is set to 1, and ions and solvent molecules are considered to have the same radius a. Furthermore, we write excluded volumes as $v_\pm = \frac{4}{3}\pi a^3$, thus excluding the effect of the hydration shell of ions on the EDL structure.

4.2.1 Effect of surface charge density

Our theory successfully captures the transition from a normal double layer to an overcharged one as surface charge density increases. Fig. 4.1a and 4.1b show the electrostatic potential profile and ion distribution respectively for the case of a 2:1 salt solution. At a low σ value of -0.02 C/m^2, the potential is negative in the entire region, in line with the normal double-layer structure predicted by PB. As σ increases to -0.15 C/m^2, more counterions are attracted to the surface, enhancing the strength of ion correlations. Compared to the case of $\sigma = -0.02$ C/m^2, the EDL becomes narrower and the ion concentrations close to the surface increase for $\sigma = -0.15$ C/m^2, as has been observed in simulations [58, 156]. The sign of potential turns from negative to positive, leading to an overcharged double layer. Because of overcharging, coions are enriched in the diffuse region far away from the surface, and counterions are depleted as depicted in Fig. 4.1b. For very high $|\sigma| > 4$ C/m^2, EDL remains overcharged but

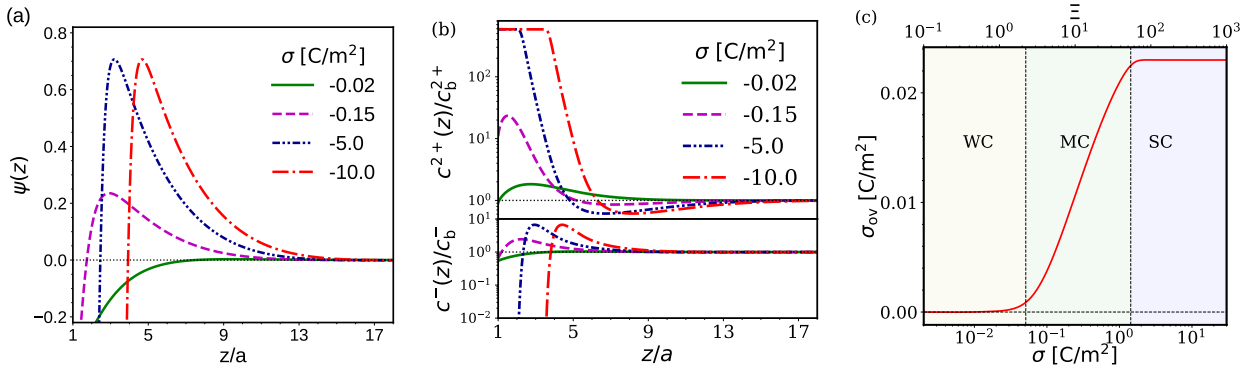

Figure 4.1: Continuous transition from normal double to overcharged double layer depicted using 2:1 salt solution. $c_b = 0.2$ M, $a_{\pm,s} = 1.5$ Å and $\varepsilon_S = \varepsilon_P = 80$. a) Electrostatic potential $\psi(z)$ profiles and b) distributions of counterion and coions for increasing surface charge density σ. c) The degree of overcharging σ_{ov} as function of σ and electrostatic coupling parameter Ξ. Three regions correspond to weak coupling (WC), moderate coupling (MC), and strong coupling (SC).

the counterion accumulation near the surface reaches its saturation concentration determined by the excluded volume constraint. A three-dimensional condensed layer of counterions is formed with almost no coions. The thickness of the condensed layer increases as σ becomes more negative. This phenomenon is commonly known as the "crowding" of finite-size ions in EDLs[53, 103, 141].

To further elucidate the dependence of overcharging on σ, we define the degree of overcharging as $\sigma_{ov} = \int_0^{z^*} \rho(z)dz - |\sigma|$. σ_{ov} quantifies the number of accumulated counterions in excess of bare surface charge. z^* is the position at which net charge density $\rho(z)$ changes sign from positive to negative. $\sigma_{ov} = 0$ represents the absence of overcharging, whereas overcharging is stronger as σ_{ov} becomes more positive. Fig. 4.1c shows a continuous transition from a normal double layer to an overcharged one, in agreement with the observations in experiments and simulations[138–140]. At very high σ, σ_{ov} attains a plateau due to the saturation of counterion density near the surface. This trend has also been indicated by different independent simulation studies[138, 157], which observed a slow down of inverted ψ_ζ and its potential saturation at high σ.

The physical origin of overcharging can be characterized using the electrostatic coupling parameter $\Xi = 2\pi q_+^3 l_b^2 \sigma/e$, where $l_b = \frac{e^2}{4\pi\epsilon k_B T}$ is the Bjerrum length. l_b measures the strength of coulombic interactions compared to thermal energy. Ξ hence quantifies the strength of ion-ion correlations compared to thermal energy. Fig. 4.1c clearly shows that the overcharging curve can be divided into three regimes: $\sigma_{ov} = 0$, a fast increase of σ_{ov}, and the plateau, corresponding respectively to weak, moderate and strong coupling regimes. In the weak coupling regime, EDL can be qualitatively described by the mean-field PB. In the moderate

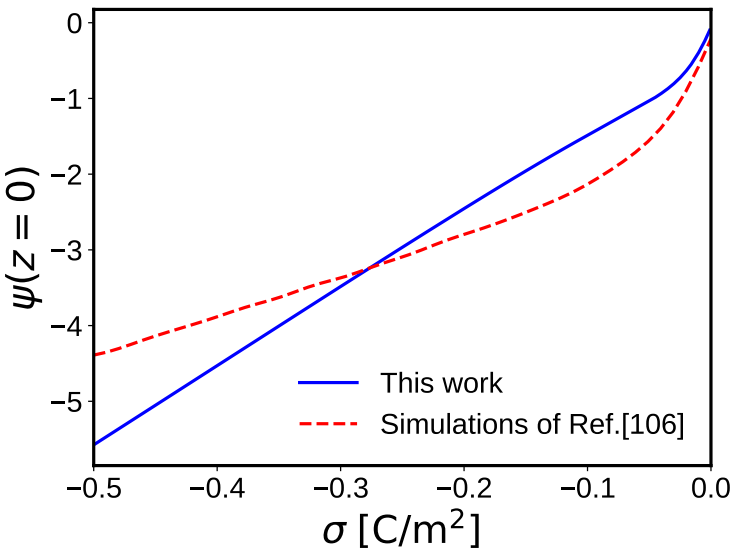

Figure 4.2: Electrostatic potential at the surface, $\psi(z = 0)$, as a function of surface charge density σ. The solid lines represent predictions of our theory and the dashed lines represent the simulation results of Valiskó et al.[58]. Parameters used for both our calculations and simulations are: $c_b = 0.1$ M, $a_{\pm,s} = 1.5$ Å, and $\varepsilon_S = \varepsilon_P = 80$.

coupling regime, PB fails to even qualitatively capture the overcharged EDL, which necessitates a systematic inclusion of correlations. Finally, in the strong-coupling regime, both correlations and excluded volume effects play a significant role in describing crowding. Our theory predicts that the transition from weak to moderate coupling occurs at $\Xi \sim O(1)$ and that from moderate to strong coupling occurs at $\Xi \sim O(100)$. These results of transition points are in quantitative agreement with the values well-accepted in literature to separate different coupling regimes[40, 151, 158]. Hence, our theory is successful in self-consistently unifying the description of overcharging in all three coupling regimes. We also note that a similar characterization of the overcharged EDL in terms of three distinct regimes was also done by Voukadinova and Gillespie [159]. However, to our knowledge, our theory is the first to discuss the existence of saturation in the degree of overcharging in the strong coupling regime. It is also important to highlight here that the inclusion of the excluded volume effect in the Modified Gaussian Renormalized Fluctuation Theory is essential to capture the crowding of finite-size ions and saturation in overcharging in the strong coupling limit.

To validate our theory, we provide a quantitative comparison with Monte-Carlo simulations of Valiskó et al.[58] in Figure 4.2. Using the same value of surface charge, ion size, and bulk salt concentration as in simulations, our theoretical predictions of surface electrostatic potential are in good agreement with the simulation data without any fitting parameters. The agreement is better at low σ compared to high σ values. One possible reason for this deviation could be the fact that the simulations of Valiskó et al. used an implicit model for

solvent which ignores its excluded volume. This implicit treatment leads to larger counterion accumulation at the surface and hence lower surface potentials. We note that at high σ the volume fraction of ions at the surface becomes very large. This requires a more rigorous treatment of the excluded volume effect compared to the local-density approximation used in our theory, such that the microstructure of the condensed layer can be quantitatively captured. However, in any case, the behavior of overcharging can still be divided into the three aforementioned coupling regimes as discussed above in Figure 4.1c. In order to reproduce features like oscillations in counterion density profile as observed in simulations[58, 143] the incompressibility constraint should be replaced by tools like the fundamental measure theory used in DFT-based approaches[54, 156].

4.2.2 Effect of counterion valency

Counterion valency also has a significant impact on overcharging. Increasing valency leads to stronger correlations, enhances overcharging, and even induces oscillations in electrostatic potential and ion distribution. In Fig. 4.3, $\psi(z)$ is plotted for $q_+ = 1$, 2, and 3. Monovalent counterions do not show any overcharging even at very high σ. Although the correlation strength increases for divalent counterions, it results only in marginal overcharging for practical choices of surface charge and ion size. This is the reason why it is experimentally difficult to observe charge inversion in divalent electrolytes[30]. For trivalent ions, correlation is greatly enhanced, and overcharging is pronounced. Ionic layering occurs near the surface; oscillations in the distribution of both counterions and coions are observed as in the inset of Fig. 4.3. The oscillation is a sign of successive overcharging; each peak in the $\psi(z)$ essentially overcharges the layer of net negative charge preceding it.

4.2.3 Effect of dielectric contrast

The systematic treatment of electrostatic fluctuations allows us to simultaneously capture the inhomogeneity in both ionic strength and dielectric permittivity. In most real systems there is a dielectric mismatch between the charged plate and electrolyte solution, resulting in image charge repulsion on mobile ions. The image charge effect is found to alter EDL only in the weak coupling regime, refer to Fig. 4.4. For 2:1 salt solution at low $\sigma = -0.01$ C/m^2, the electrostatic potential profile shifts significantly towards negative because the weak correlation due to low counterion concentration cannot counter the image charge depletion. On the contrary, for high $\sigma = -0.15$ C/m^2 when charge inversion occurs, the counterion concentration near the surface is so high that EDL is dominated by the ion correlation. The change in $\psi(z)$ is therefore almost negligible. These predictions are consistent with the simulation results of Wang and Ma [160]. In Figure 4.5, we compare our theoretical predictions with their results for the case of trivalent and monovalent salt mixture. At a high σ of -0.16 C/m^2, the $\psi(z)$ profiles with the dielectric contrasts obtained from both theory and simulation completely overlap with the case of no dielectric contrast. However,

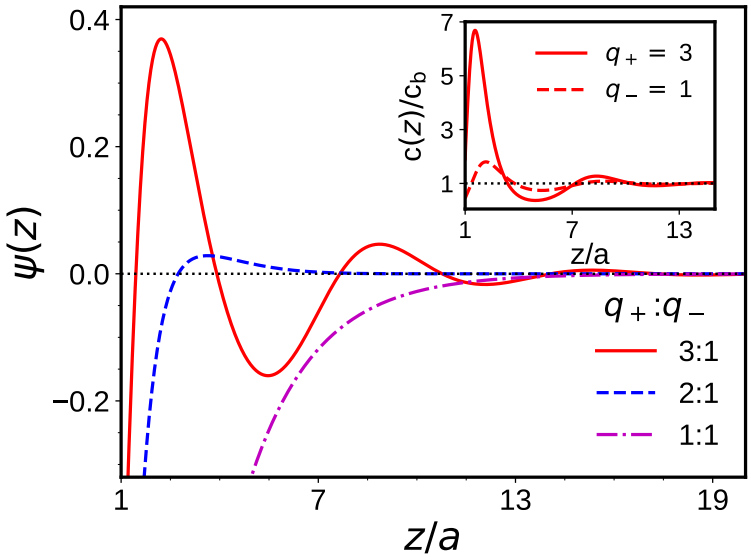

Figure 4.3: The effect of counterion valency on electrostatic potential profiles. The inset highlights the oscillations in counterion and coion distributions. $c_b = 0.5$ M, $\sigma = -0.15$ C/m^2, $a_{\pm,s} = 2.1$ Å, and $\varepsilon_S = \varepsilon_P = 80$.

at low σ of -0.04 C/m^2, dielectric contrast was found to shift $\psi(z)$ in the negative direction. With only ion size $a_\pm = 3.0$ Å as an adjustable parameter, the theoretical values of $\psi(z)$ in both cases are in good quantitative agreement with the simulations. The ion size $a_\pm$ used in simulations was 4.8 Å.

4.2.4 Effect of salt concentration

Experiments[30, 43] and simulations[58, 144] have observed non-monotonic dependence of inverted ionic current and electrophoretic mobility on salt concentration, a feature which has not been fully understood yet. Our theory is able to capture this non-monotonic behavior of overcharging with increasing multivalent salt concentration. This non-monotonicity is a consequence of the competition between ion correlations and the translational entropy of ions. In Figure 4.6a, electrostatic potential profiles $\psi(z)$ are plotted for three different salt concentrations of trivalent salt ($q_+ = 3$ and $q_- = 1$). At a low salt concentration of $c_b = 0.05$ mM or debye length $\lambda_D = 17.7$ nm, the entropic penalty for the ions to come to the surface is very high and cannot be compensated by the gain in the energy due to ion-ion correlations. Thus, there is no overcharging, and $\psi(z) < 0$ in the entire EDL. When $c_b = 10$ mM ($\lambda_D = 1.25$ nm), the increased strength of ion correlations is sufficient to overcome the entropic loss for the ions to move from the bulk to the surface. $\psi(z)$ becomes greater than zero and the double layer is strongly overcharged. However, a further increase of c_b to 1000 mM ($\lambda_D = 0.125$ nm) suppresses overcharging: $\psi(z)$ is less positive than the case of $c_b = 10$

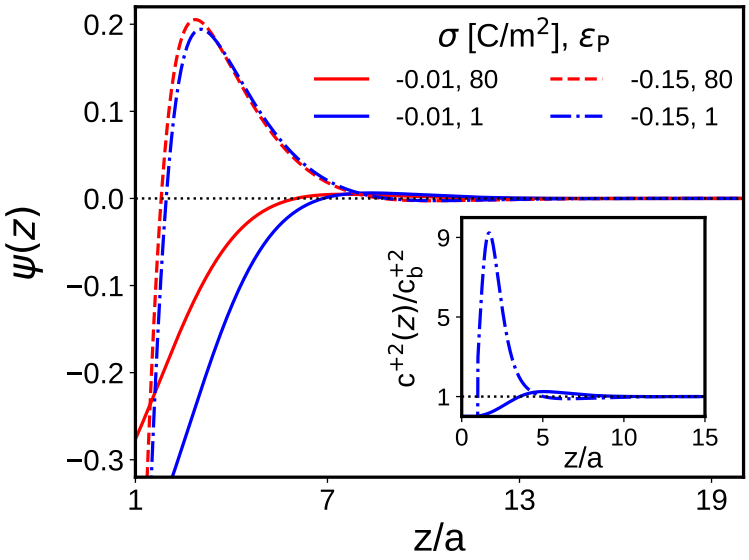

Figure 4.4: The image charge effect due to dielectric contrast on charge inversion. The inset shows the difference in counterion distribution under the absence ($\sigma = -0.01$ C/m^2) and the presence ($\sigma = -0.15$ C/m^2) of charge inversion when the dielectric contrast is included. $q_+ = 2$, $q_- = 1$, $c_b = 0.5$ M, $a_{\pm,s} = 1.5$ Åand $\epsilon_S = 80$.

mM. At high salt concentrations, although the entropic penalty is small, the strength of ion-ion correlations far away from the surface and in the bulk is greatly enhanced, which reduces the driving force for ions to come to the surface. This depletion of ions from the surface is also facilitated by the excluded volume interactions between ions and solvent molecules, as can be seen from Equation (2.14).

The relative contribution of inhomogeneous ion correlations and excluded volume effects to the aforementioned non-monotonic trend can be evaluated by quantifying the degree of overcharging σ_{ov}. In Figure 4.6b, σ_{ov} is plotted as a function of salt concentrations. For comparison, we also provide the results for the case without including the excluded volume effects. Both the two curves capture the non-monotonic nature of overcharging, with a slightly enhanced σ_{ov} in the absence of the excluded volume effects. Thus, an accurate accounting of spatially varying ion correlations from surface to bulk is necessary and sufficient to explain the non-monotonic salt concentration dependence of overcharging. Furthermore, the biggest difference in σ_{ov} values of the two curves occurs near the maxima. Hence, it can be expected that the excluded volume effects could play a more significant role when the density of ions near the surface is very high - the strong coupling limit. Examples include systems with very high surface charges or large ion sizes, such that ionic crowding can take place at the surface[161]. However, for practical values of surface charge densities and ion sizes like the parameters chosen in the current calculations ($\sigma = -0.15$ C/m^2 and $a_{\pm,s} = 2.5$ Å), ionic crowding is absent and hence the excluded volume effect on overcharging is negligible.

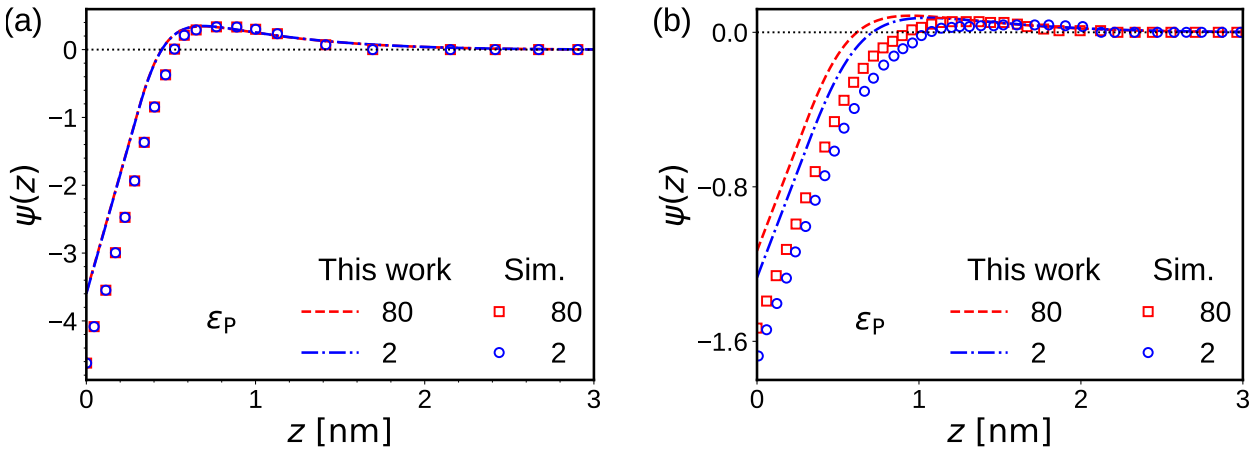

Figure 4.5: Effect of dielectric contrast on electrostatic potential profiles $\psi(z)$. Comparing our theoretical predictions with simulations of Wang and Ma[160] for the case of trivalent and monovalent salt mixture. $c_b^{3:1} = 0.03$ M, $c_b^{1:1} = 0.1$ M, $a_\pm = 3.0$ Å and $\epsilon_S = 80$. a) $\sigma = -0.15$ C/m^2 and b) $\sigma = -0.04$ C/m^2. Lines represent our theoretical predictions and symbols represent simulation data. The ion size $a_\pm$ used in simulations was 4.8 Å.

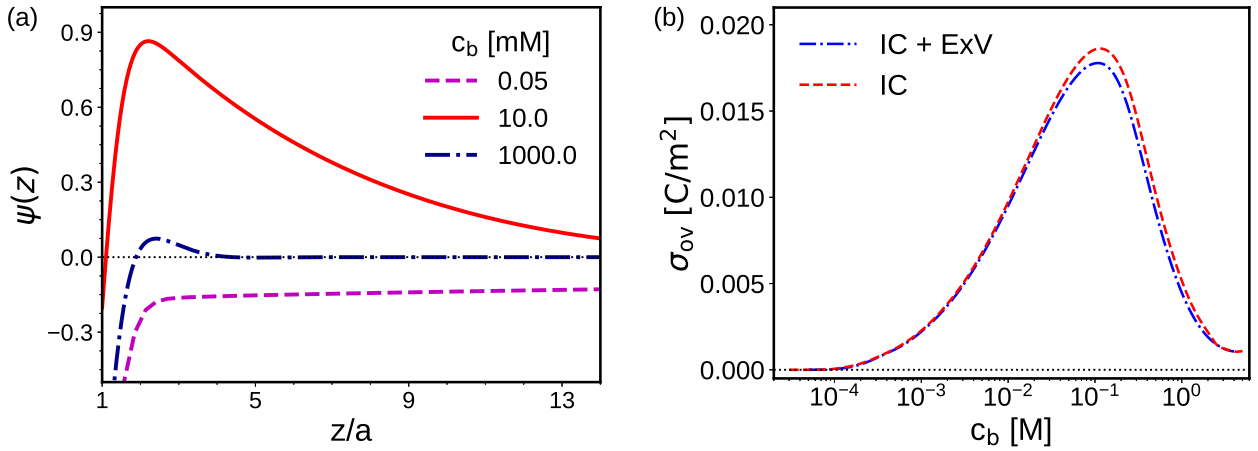

Figure 4.6: Non-monotonic overcharging of the double layer with increasing trivalent salt concentration c_b, $q_+ = 3$, $q_- = 1$, σ = -0.15 C/m^2 and $a_{\pm,s} = 2.5$ Å. a) Electrostatic potential $\psi(z)$ profiles and b) the degree of overcharging σ_{ov}, as a function of c_b. *IC + ExV* includes both ion correlations (IC) and excluded volume (ExV) effects whereas *IC* only includes ion correlations.

4.2.4.1 Inversion of streaming current in nanochannels

Here, we compare our theoretical predictions with experimental measurements of the streaming current S in planar nanochannels by van der Heyden et al.[30]. To calculate S, we incorporate the double-layer structure into the Poiseuille flow. The expression for streaming current in a nanochannel is given by

$$S = w \int_0^H \rho(z) u(z) dz \tag{4.1}$$

where $\rho(z)$ is the local charge density, $u(z)$ is the local fluid velocity, w is the width and H is the height of the nanochannel. An accurate theoretical prediction of streaming current requires knowledge of factors like the position of the slip plane, concentration-dependent viscosity, and ion correlations. Here we use a simple model with the position of the slip plane at $z = 2a$, where a is the radius of the ions. This choice for slip plane is commonly adopted in previous works[54, 138, 139] and is also supported by electrophoretic simulations [127, 162]. The viscosity of the solution is taken to be that of the bulk water. For the case of pressure-driven flow, the local fluid velocity can be written from planar Poiseuille flow as

$$u(z) = \frac{\Delta P_{\text{channel}}}{8\nu L} \frac{H^2}{(H/2 - 2a)^2} (z - 2a)(H - 2a - z) \tag{4.2}$$

where $\Delta P_{\text{channel}}$ is the applied pressure difference, ν is the bulk viscosity of water and L is the length of the nanochannel. Substituting Eq. 4.2 into Eq. 4.1 and using local charge density predicted by the theory, the streaming current can be calculated, as shown in Fig. 4.7a. Only the ion size a was used as a fitting parameter, and the surface charge and the dimensions of the nanochannel were adopted from the experimental setup of van der Heyden et al.[30]. In section 4.2.3, we showed that the strength of charge inversion is not affected by long-range image interactions, therefore, we take the dielectric permittivity to be equal to that of water throughout the system.

Fig. 4.7a shows a non-monotonic behavior of S as a function of c_b for both divalent and trivalent salts. This nature as explained above is a consequence of competition between correlations and the translational entropy of ions. At low salt concentrations, the translational entropy loss for ions to accumulate at the surface is very large, which cannot be compensated by the energy gain from correlation. Thus, counterion accumulation is limited and there is no charge inversion. As c_b increases, the gain in correlation increases, whereas the entropic loss for ions to come to the surface decreases. As a result, counterion accumulation is sufficient to invert the sign of ψ_ζ and hence S from positive to negative. For higher c_b, the strength of ion correlations in bulk also increases which reduces the energetic incentive for the counterions to migrate to the surface. This together with the excluded volume effect at the surface leads to a maximum in S. With the continued increase in c_b, strong correlations in bulk further reduce counterion accumulation, and the sign of S changes back from positive to its original negative, manifested as "reentrant charge inversion". Finally, at extremely high salt concentrations, S approaches zero due to strong screening. As shown in Fig. 4.7a,

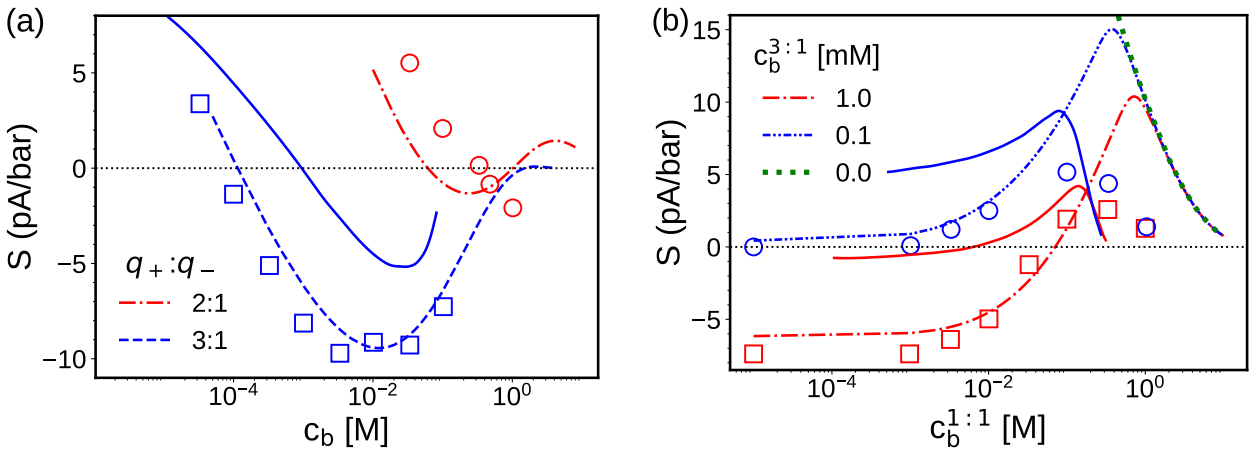

Figure 4.7: Nonmonotonic dependence of charge inversion on salt concentration. $\sigma = -0.15$ C/m^2 and $\varepsilon_S = \varepsilon_P = 80$. a) Streaming current S as a function of c_b for pure divalent ($a_\pm = 1.5$ Å) and trivalent ($a_\pm = 2.5$ Å) salt solution. b) S_{str} as a function of added monovalent salt $c_b^{1:1}$ to a fixed trivalent salt concentration $c_b^{3:1}$. $a_\pm = 2.5$ Å for both monovalent and trivalent salt. Dashed lines represent our theoretical predictions, solid lines represent DFT results from Hoffman and Gillespie[57], and symbols represent experimental S data adopted from van der Heyden et al.[30].

our theoretical predictions capture the non-monotonic dependence of streaming currently on the salt concentration with a good quantitative agreement with experimental data [30]. The ψ_ζ predicted by our theory for 3:1 salt is also close to the simulation results of Valiskó et al.[58]. The value of ψ_ζ at $c_b = 1$ M and $\sigma = -0.1$ C/m^2 as obtained in simulation is -0.06, and our theoretical result for the same σ, c_b and ion radius of 3.0 Å is -0.024. This negative sign of ψ_ζ predicted by both simulations and our theory is consistent with the idea of non-monotonic behavior of charge inversion with salt concentration. For trivalent ions, the agreement is remarkable, because the electrostatic correlation is the dominant effect for ions with high valency. However, for divalent salts, our theory underestimates critical salt concentration for charge inversion. In the case of divalent counterions, the strength of correlations is not very strong and the structure of the double layer is also influenced by other effects like specific adsorption, the orientation of dipoles near the surface, and the hydration of ions.

Our theory can also capture the non-monotonic reduction of charge inversion as monovalent salt is added to a multivalent salt solution[30]. The addition of monovalent salt also enhances ion correlations in bulk and hence in Fig. 4.7b, S shows an initial increase and a subsequent disappearance of charge inversion as monovalent salt concentration $c_b^{1:1}$ increases. With the continued increase in $c_b^{1:1}$, the role of monovalent counterions becomes more important, resulting in a minimum in S. After that, EDL gets dominated by monovalent salt, and

S approaches zero. The curves of two $c_b^{3:1}$ values merge with that of a pure monovalent salt solution. At low $c_b^{1:1}$, our calculations of S are in excellent agreement with the experiments of Van der Heyden et al. [30]. The discrepancy between theory and experiments at high $c_b^{1:1}$ could be attributed to the increased viscosity near the interface at high salt concentrations [163, 164]. Issues with modeling electrokinetic flow at high salt concentrations are discussed in detail in the review paper by Bazant et al.[165].

For comparison, the results from a density functional theory (DFT) based approach by Hoffman and Gillespie[57] are also plotted in Figure 4.7. In the pure trivalent salt case, this approach overestimates the critical concentration required for charge inversion by an order of magnitude. DFT also underestimates the magnitude of current by at least a factor of two. In the case of mixtures, for the case of 1mM $c_b^{3:1}$, DFT underestimates the critical monovalent salt concentration required to cancel charge inversion by an order of magnitude. For both 0.1 mM and 1 mM trivalent salt, DFT overestimates the magnitude of streaming current by at least five orders of magnitude in both low and high monovalent salt conditions.

4.2.4.2 Reversal of electrophoretic mobility

The electrophoretic mobility μ_{ep} of a charged colloidal particle is determined from the following equation

$$\mathbf{u}_\infty = \mu_{ep}\mathbf{E} \tag{4.3}$$

where $\mathbf{u}_\infty$ is the fluid velocity far away from the charged particle and $\mathbf{E}$ is the applied electric field. For small electric fields, the so-called linear regime, μ_{ep} is independent of $\mathbf{E}$, and only depends on the intrinsic double layer structure and fluid properties. In this section, we compare our theoretical predictions with experimental measurements for colloidal particles with diameters much larger than both the thickness of the double layer and the velocity profile. Thus, the curvature of the particle can be neglected and the double layer and the velocity profile can thus be approximated as that in the planar geometry. We further assume $\nu(z)$ and $\epsilon(z)$ to be constant and replace them with their bulk value of water. The drift velocity for this system of a salt solution surrounding a particle in the presence of applied electric field E in the x-direction is given by

$$u_\infty = \frac{\epsilon\psi_\zeta}{\nu}E \tag{4.4}$$

where ψ_ζ is the electrostatic potential at the slip plane. μ_{ep} can be easily identified from the above equation as $\frac{\epsilon\psi_\zeta}{\mu}$. This is the well-known Helmholtz-Smoluchowski equation[166]. ψ_d is calculated using the Modified Gaussian Renormalized Fluctuation Theory and the predictions can be directly compared with experimental data.

By incorporating the Modified Gaussian Renormalized Fluctuation Theory into the Helmholtz-Smoluchowski equation as shown above, we successfully predict the non-monotonic dependence of inverted electrophoretic mobility μ_{ep} on trivalent salt concentration. This non-monotonic effect is also an outcome of the competition between ion correlations and the

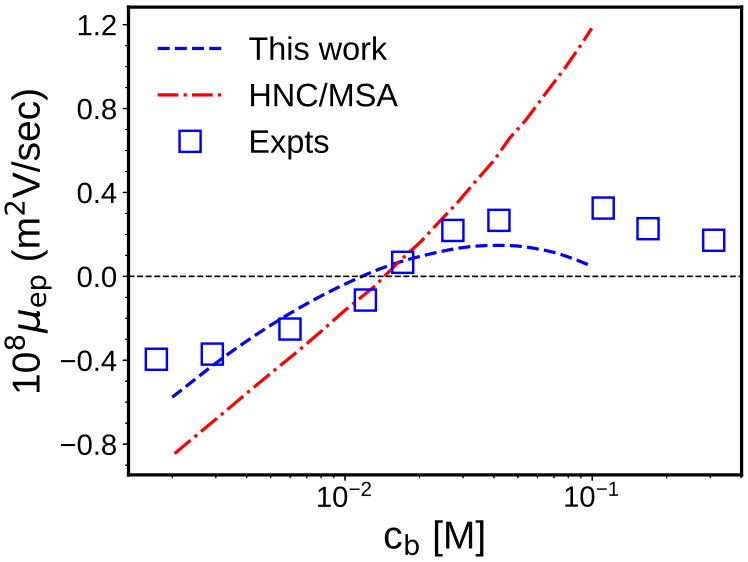

Figure 4.8: Non-monotonic behavior of the reversed electrophoretic mobility of a negatively charged colloidal particle immersed in a trivalent salt solution. Symbols represent experimental data from Martín-Molina et al.[42] and dashed lines represent our theoretical calculations $q_+ = 3$ and $q_- = 1$, $\sigma = -0.016$ C/m^2 and $a_{\pm,s} = 2.3$ Å. For comparison, the results of the Integral equation-based formalism used by Martín-Molina et al.[42] is shown in *HNC/MSA* line.

translation entropy of ions, similar to the streaming current profile in Figure 4.7. As shown in Figure 4.8, our predictions are in quantitative agreement with experimental measurements for μ_{ep} was calculated for c_b ranging from 0.002 M to 0.1 M, where the corresponding range of Debye screening length λ_D is 2.8 nm to 0.4 nm. The small difference between our theory and experiments at low c_b can be attributed to the planar approximation for the double layer and velocity field invoked in the calculation. On the other hand, at high salt concentrations, although neglecting the curvature of particles is a good approximation, the discrepancy between theory and experiments could be explained by the uncertainty in the position of the slip plane as well as the value of viscosity in the double layer. Particularly, for $c_b > 0.1$ M, $\lambda_D > 0.4$ nm is very close to the thickness of the stagnant layer ($2a = 4.6$ Å), which therefore makes the mobility calculations very sensitive to the choice of the slip plane. It should be also noted that in our calculations both ion size a and surface charge density σ are used as adjustable parameters.

We also compare our theoretical results with existing predictions from the integral equation-based HNC/MSA method by Martín-Molina et al.[42] as shown in Figure 4.8. HNC/MSA approach incorrectly predicts a monotonic increase in inverted electrophoretic mobility. Perhaps approximating the functional form of the inhomogeneous ion-ion correlation with the bulk correlation function limits the ability of integral-equation-based approaches to capture

the non-monotonic trends observed in the experiment.

4.3 Summary

We have applied the Modified Gaussian Renormalized Fluctuation Theory to elucidate the nature of overcharging and charge inversion by self-consistently capturing the spatially varying ion correlation, dielectric permittivity, and excluded volume effect. Overcharging is dominated by ion correlations and excluded volume effects, with only a minor contribution from the image force. For multivalent electrolytes, increasing surface charge induces a continuous transition from a normal double layer to an overcharged one, and eventually to ionic crowding at the surface. These three characteristics of EDL correspond respectively to weak, moderate, and strong coupling regimes. To our knowledge, our theory is the first to discuss the existence of saturation in the degree of overcharging in the strong coupling regime. Increasing counterion valency enhances overcharging and leads to ionic layering and oscillations.

Our theory also correctly captures the non-monotonic dependence of charge inversion on salt concentration. We incorporate our theory into the transport equations for electrolyte solutions to investigate ion correlation-induced inversion of electrokinetic flows. We have successfully predicted the inversion of the streaming current in nanochannels and the reversal of electrophoretic mobility of colloidal particles in the presence of trivalent salt. In a significant improvement over existing theories, we are able to capture the non-monotonic dependence of charge inversion on salt concentration in quantitative agreement with experiments. The magnitude of the inverted streaming current and the electrophoretic mobility is found to increase with salt concentration, reach a maximum, and then gradually reduce at high salt concentrations. By analyzing the effect of salt concentration on the electrical double layer structure, we elucidate the origin of this non-monotonic behavior of the electrokinetic flows. This non-monotonicity is a consequence of the competition between inhomogeneous ion correlations and the translational entropy of the ions. The existing theories have failed to qualitatively or quantitatively capture this phenomenon as they cannot accurately model the inhomogeneous ion correlations from surface to bulk. With the increase in multivalent salt concentration, the strong ion correlations in the bulk disincentive the counterions to move to the surface and overcharge the double layer. This explains the suppression of charge inversion at high salt concentrations. Although the excluded volume effect of ions and solvent molecules does lead to the depletion of counterions near the surface, its contribution to the degree of overcharging is negligible for all practical values of surface charge densities.

Chapter 5

Short-range like-charge attraction in multivalent salt solutions

5.1 Introduction

The starting point for describing the force between two surfaces immersed in an electrolyte solution is the classical Derjaguin-Landau-Verwey-Overbeek (DLVO) theory, which accounts for two contributions: the short-range Van der Waals force and the long-range electrostatic force. This electrostatic force, originating from overlapping electrical double layers (EDLs)[167], is described in the DLVO framework by the mean-field Poisson-Boltzmann (PB) theory. For two like-charged surfaces, PB predicts a universally repulsive force. However, numerous experimental [33, 84, 85] and simulation studies[86–90] have reported that this force becomes attractive at short distances in the presence of multivalent salts. This counterintuitive phenomenon is known as "like-charge attraction" and cannot be captured even qualitatively by mean-field Poisson-Boltzmann (PB).

One crucial factor missing in mean-field PB is the electrostatic correlation between ions. Molecular simulations using only hard-sphere and coulombic force fields have identified the ion correlation effect as the origin of like-charge attraction [87, 88, 168, 169]. Such simulations also observed continuous transition from repulsion to attraction as surface charge increases[170–172]. The dependence of the strength of attraction on multivalent salt concentration is rather non-trivial and shows non-monotonic behavior. Wu et al.[88] and Angelescu et al.[89] showed that attraction is most pronounced at an intermediate salt concentration and becomes weaker at high salt concentrations. A related phenomenon observed in experiments is the reentrant stability of charged colloids where the aggregates redissolve at high multivalent salt concentrations[85, 99, 100]. Furthermore, it is interesting to note that adding monovalent salt to multivalent salts significantly increases the solubility of colloids at low multivalent salt concentrations. However, this effect is negligible when the concentration of multivalent salt is high[99, 100, 173, 174].

Over the years many theories have been proposed to understand ion correlation-driven

like-charge attraction[39, 40, 44, 74, 149, 175–189]. The Strongly Correlated Liquid (SCL) theory assumes a Wigner-crystal lattice of correlated counterions at the surface in contact with a diffuse layer described by mean-field PB[67, 149, 178]. Although SCL predicts an attractive force, the model is only valid in the so-called strong coupling limit[187, 190]. Like-charge attraction is correlated to the overcharging of the EDL[149], where overcharging is defined as the excess accumulation of counterions in the double layer that could lead to a change in the sign of the curvature of the electrostatic potential[120, 161]. The subsequent reentrant condensation at high multivalent salt concentration is attributed to the significant overcharging. As per SCL theory, like-charge attraction is most prominent when the surfaces are neutralized, whereas the net electrostatic force could become repulsive when there is either significant undercharging or overcharging. To get repulsion at high salt concentrations, the surfaces have to be significantly overcharged [149]. However, simulations by Pai-Yi Hsiao[126] showed that the redissolution of polyelectrolyte condensates at high salt concentrations can occur without any inversion of their net charge. In addition, the same simulations also showed that like-charge attraction can happen even in conditions of significant undercharging. Furthermore, through simulations, Wu et al.[88] suggest that the reduction in attraction between two surfaces at high salt concentrations originates from strong bulk ion correlations which diminish the free energy gain as the two surfaces approach each other. The main limitation of the SCL theory lies in its utilization of a mean-field PB description for the diffuse region of the double layer and the bulk. Their approach only accounts for correlations within the small condensed layer of counterions near the surface. The SCL theory's inability to capture the spatially varying ion correlation from the surface to the bulk prevents correct modeling of the structure of the overlapping double layers and their free energy. Thus, they fail to explain the underlying cause of the non-monotonic strength of like-charge attraction with respect to multivalent salt concentration.

Bazant et al.[53, 186] expressed the ion correlation energy in terms of the gradient of electrostatic potential. Since the potential gradient vanishes in the bulk, this theory cannot model the bulk ion correlations correctly and thus is unable to capture the non-monotonic salt concentration dependence of like-charge attraction. Another class of methods to model ion correlations is based on the Ornstein-Zernike equation like in liquid-state integral equation theories[176–178]. Recently, using such a method, Suematsu et al.[185] captured the non-monotonic nature of attraction. However, inhomogeneous ion-ion correlation in the interface was approximated with the bulk form of the correlation function. It is well-known that such local-density approximations sometimes give unphysical results[54, 63] preventing their generalization to explain other EDL-related phenomena[114, 161]. In addition, solving the complete Ornstein-Zernike equation in an inhomogeneous system is numerically challenging, especially for trivalent salts[185].

It is also important to highlight the field-theoretic approach of Netz et al.[39, 40, 184] in modeling like-charge attraction. They used a perturbative expansion in terms of electrostatic coupling parameter $\Xi = 2\pi q^3 l_B^2 \sigma$ to capture the coulombic energy gain due to ion correlations. Here, q is the counterion valency, l_B is the Bjerrum length, and σ is the surface charge density of the two surfaces. However, their analysis was limited to double layer forces in

counterion-only systems, i.e., where the number of counterions in the system is fixed. These counterion-only systems are fundamentally different than salt systems, as in the latter the bulk concentration of ions also plays a critical role in determining the strength of attraction. The difference between the two kinds of systems and associated bulk correlations becomes further important as closely relevant phenomena of ion correlation-induced overcharging can only happen in salt systems. Both experiments[30, 42] and simulations[43, 126, 144] have shown that like the strength of like-charge attraction, the strength of overcharging also depends non-monotonically on multivalent salt concentration. Therefore, it is necessary to develop a self-consistent approach to model ion correlations that can capture both overcharging and like-charge attraction in multivalent salt systems.

Furthermore, in order to have a full understanding of the stability and self-assembly of charged colloids, both electrostatic and non-electrostatic effects need to be accounted for. The relative importance of the non-electrostatic effects like specific adsorption, solvation, and hydration can only be evaluated if the essential electrostatic contributions are accurately modeled. To our knowledge, existing works have not self-consistently solved the inhomogeneous electrostatic correlations from the interface to the bulk to explain like-charge attraction in multivalent salt solutions. In this chapter, we address this gap by leveraging the Modified Gaussian Renormalized Fluctuation Theory[41, 75, 120, 191], which in Chapter 4 was shown to quantitatively capture the phenomenon of overcharging[120, 161]. With this approach, we aim to fully account for the effect of spatially varying ion correlations on the structure of overlapping electric double layers (EDLs) and their associated free energies. We elucidate the nature of like-charge attraction with respect to surface charge, counterion valency, salt concentration, and the addition of monovalent salts. The connection between overcharging and like-charge attraction is also examined.

5.2 Results and Discussion

We consider a system of two similarly charged plates located at $z = 0$ and $z = D$, where D is the separation distance between the two plates. Both plates have a uniform surface charge density σ. The electrolyte solution with cations of valency q_+ and anions of valency q_- is confined in the region between the plates and is connected to an outer bulk reservoir of salt concentration c_b. In this section, we study the effect of surface charge, counterion valency, and salt concentration on electrostatic force between the two surfaces. For simplicity, the dielectric function is assumed to be constant throughout the system, $\varepsilon(\boldsymbol{r}) = 78.5$, i.e., the primitive model for electrolytes. Ions and solvent molecules are considered to have the same radius a, which is also the minimum possible separation between an ion's center and the charged surface. The equations and boundary conditions to solve for this system are 2.40 - 2.46, given in Section 2.5. The pressure P between the two surfaces is calculated using

$$P = -\left(\frac{\partial \mathcal{W}}{\partial h}\right)_{\mu_\pm} - P_\mathrm{b} \tag{5.1}$$

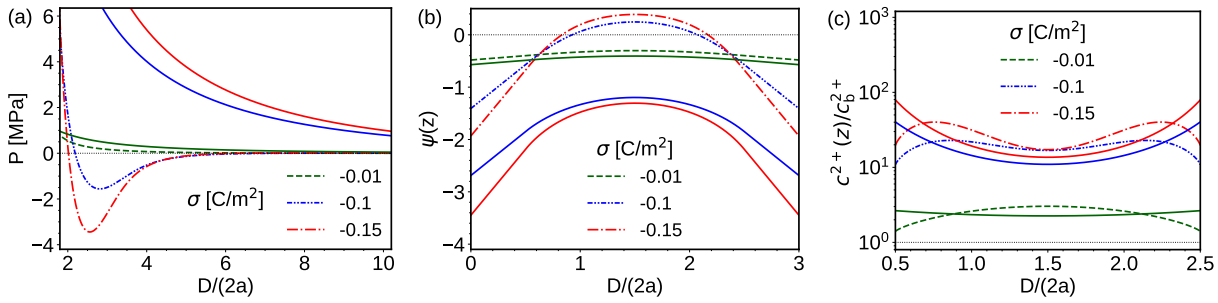

Figure 5.1: Continuous transition from pure repulsion to short-range attraction in overlapping double layers as surface charge density σ increases. $q_+ = 2$, $q_- = 1$, $c_b = 0.1$ M, $a_{\pm,s} = 1.5$ Å. a) Pressure as a function of separation distance D between the two plates. b), and c) plot electrostatic potential profiles $\psi(z)$, and counterion concentration profiles, respectively for $D = 6a$. Dashed lines represent predictions from our theory and solid lines represent mean-field Poisson-Boltzmann results.

where $\mathcal{W}$ is defined in Eq. 2.46 and P_b in Eq. 2.26.

5.2.1 Effect of surface charge

In agreement with simulations[170–172], our theory predicts a continuous transition from pure repulsion to like-charge attraction as surface charge density increases. Figure 5.1a plots the pressure () P as a function of separation distance h for the case of 0.1 M divalent salt solution, $q_+ = 2$ and $q_- = 1$. At a low σ value of -0.01 C/m^2, the pressure remains positive (repulsion) at all separations, in quantitative agreement with the predictions of mean-field PB. Increasing σ to -0.1 C/m^2 leads to a weak short-range attraction. This attraction gets more pronounced as σ becomes more negative. In stark contrast, PB predicts a stronger repulsion as the magnitude of σ increases. For all σ values, attraction is short-ranged and occurs at a separation distance of a few ion diameters, in agreement with simulations[86, 87, 168]. At large h, the force has a weak repulsive tail compared to PB, which has also been observed in simulations[88, 89, 168].

To understand the origin of like-charge attraction, electrostatic potential profiles $\psi(z)$ and counterion concentration profiles $c_b^{2+}(z)$ are plotted in Figure 5.1b and 5.1c respectively. The inclusion of ion-ion correlations leads to an enhanced screening of the surface charges hence reducing surface potential and the repulsive component of the free energy (first line in Eq. 2.19). The remaining attractive contribution directly comes from the gain in ion-ion correlation energy described by the third line in Eq. 2.19. At low surface charges, counterion concentrations are not high enough to make correlation effects important. Hence our pressure, $\psi(z)$, and $c_b^{2+}(z)$ predictions are very close to PB. It is at high surface charges where the correlation contribution to free energy starts dominating; our theoretical predictions

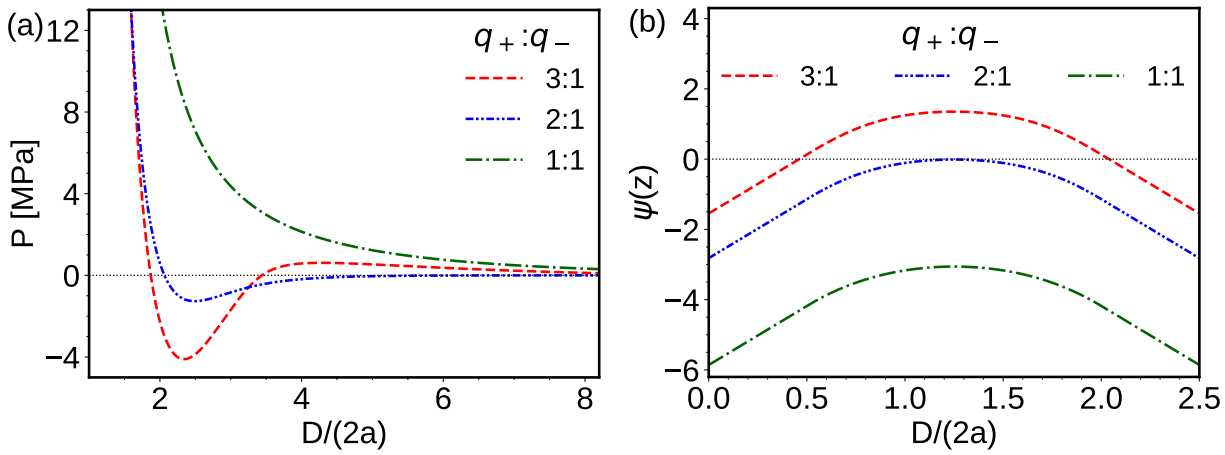

Figure 5.2: a) The effect of counterion valency on pressure P. b) Electrostatic potential $\psi(z)$ for $D = 5a$. $c_b = 0.1$ M, $\sigma = -0.15$ C/m^2, $a_{\pm,s} = 2.0$ Å.

start deviating significantly from PB and an attractive force appears. It is also worth noting that in Figure 5.1c ion concentrations are significantly larger than the bulk at the mid-plane (z=$h/2$). Thus, if the pressure is calculated using the mean-field Maxwell stress, one would only get a repulsive force. The reason our theory correctly predicts the short-range attraction is the systematic inclusion of the ion correlation contribution to the free energy. Figure 5.1 also demonstrates the lack of any causal relationship between overcharging and like-charge attraction. The curvature of $\psi(z)$ remains negative for all chosen σ values, implying the absence of any overcharging of EDL. However short-range attraction is still observed at high σ. Our results elucidate that while both the phenomena of overcharging and like-charge attraction arise from ion correlations, the presence of one phenomenon does not inherently imply the presence of the other. Similarly, the existence of one is not a prerequisite for the occurrence of the other. This also confirms the simulation results of Allahyarov et al.[192] and P.Y. Hsiao[126]. Our Modified Gaussian Renormalized Fluctuation Theory is the first to coherently capture these two phenomena in a unified framework.

5.2.2 Effect of counterion valency

Counterion valency is another key factor in determining the strength of ion correlations and hence the double-layer force. Figure 5.2a plots the pressure profiles for different counterion valencies. For monovalent counterions, correlations are very weak and the force is repulsive at all length scales. In fact, our theory does not show any attraction for monovalent salts for all values of σ, as also seen in simulations [86–90, 168]. For divalent counterions, correlation strength increases, leading to a small attractive force. For trivalent counterions, a very

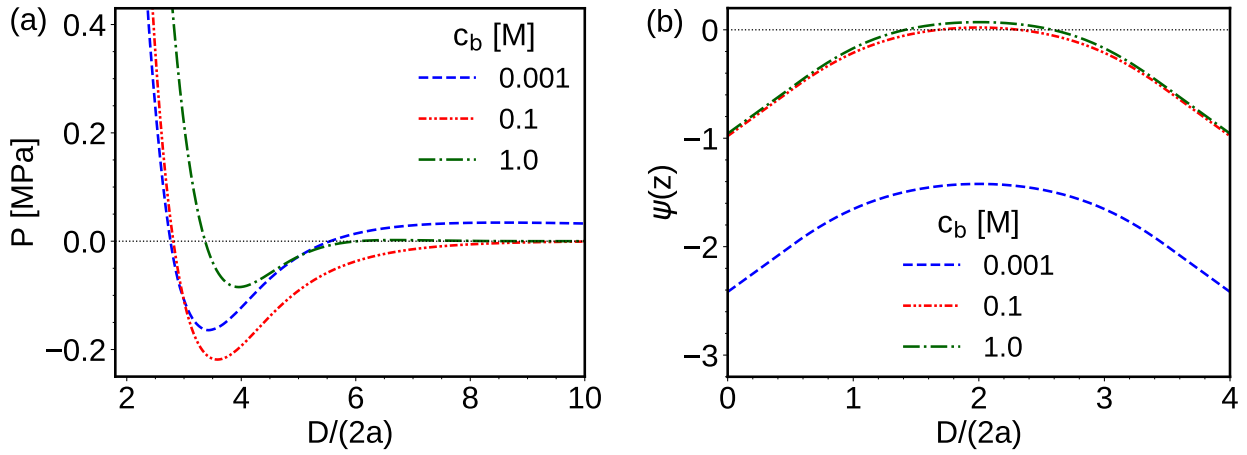

Figure 5.3: a) Non-monotonic salt concentration dependence of the attractive force. b) Electrostatic potential profiles $\psi(z)$ at h = $8a$, where the force is attractive for all three c_b. $q_+ = 2$, $q_- = 1$, $\sigma = -0.05$ C/m^2, $a_{\pm,s} = 1.5$ Å.

strong attractive force is predicted. This increasing strength of attraction is in agreement with simulations of Linse and Lobaskin [86, 87], where the size of colloidal aggregates was found to be significantly larger in the presence of trivalent ions compared to divalent ions. Furthermore, $\psi(z)$ profiles in Figure 5.2b show that an increase in the strength of correlations also enhances the possibility of overcharging. The EDL is not overcharged for any of the three counterions; however, both trivalent and divalent ions show like-charge attraction. This again proves the lack of any causal relationship between overcharging and like-charge attraction.

5.2.3 Effect of salt concentration

Monte Carlo simulations have shown that the attractive force does not monotonically increase with salt concentration[88, 89]. This non-monotonic salt concentration dependence of like-charge attraction is also correctly captured by our theory. Figure 5.3a shows pressure profiles for three different salt concentrations. Increasing c_b from 0.001 M to 0.05 M weakens the long-range repulsion because of the enhanced screening of surface charges. In addition, the attraction well deepens, as higher bulk ion concentration reduces entropy loss for ions to move to the surface. This drives more counterions to the surface leading to larger gains in the correlation energy. However, attraction almost disappears for $c_b = 1.0$ M . At very high salt concentrations, the strength of correlations in the bulk itself is very strong and there is no gain in correlation energy for the ions when they come from bulk to the surface. The accumulation of ions is further bounded by the excluded volumes of ions and solvent

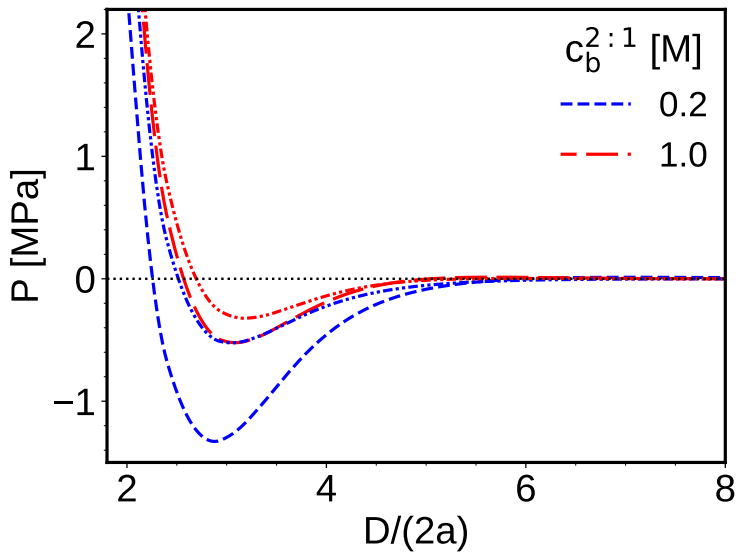

Figure 5.4: The effect of adding 0.5 M monovalent salt to a solution with fixed concentrations of divalent salt $c_b^{2:1}$ on like-charge attraction. The solid lines represent pressure curves for the pure divalent salt solution and the dashed lines represent pressures after monovalent salt is added. $\sigma = -0.1$ C/m^2, $a_{\pm,s} = 1.5$ Å.

molecules. In Figure 5.3b, we also plot $\psi(z)$ for the three c_b at $h = 8a$, where all three concentrations show attractive force. The curvature of $\psi(z)$ remains negative for all c_b values implying no overcharging of the surfaces. These results are in agreement with the simulations by Pai-Yi Hsiao [126] which showed that the redissolution of polyelectrolyte condensates at high salt concentrations can occur without any inversion of their net charge. In addition, the same simulations also showed that like-charge attraction can happen even in conditions of significant undercharging, a feature that is also captured by our theory, see the curves of $c_b = 0.001$ M in Figure 5.3. Therefore, this non-monotonic behavior of the attractive force should be understood as a result of the competition between ion correlations and the translational entropy of the ions.

5.2.4 Effect of secondary monovalent salt

The addition of monovalent salt to a multivalent salt solution also increases the strength of ion correlations in bulk and leads to a decrease in the strength of attraction. In Figure 5.4, 0.5 M of monovalent salt is added to 0.2 M and 1.0 M of a fixed concentration of divalent salts ($c_b^{2:1}$). For low $c_b^{2:1}$, the addition of monovalent salt leads to a significant reduction in attraction. However, as $c_b^{2:1}$ increases, the effect of monovalent salt on this suppression of attraction reduces. This effect is almost negligible for 1.0 M. At 1.0 M of $c_b^{2:1}$, the strength of bulk correlations due to divalent salt is high enough that further addition of monovalent

salt does not lead to any change in attraction. The curve for the salt mixture completely overlaps with the case of pure divalent salt. A similar dependence of adding monovalent salt has been indicated in the solubility measurements of charged colloids [100, 173, 174]. Experiments found that the addition of monovalent salt increases the critical multivalent salt concentration to initiate aggregation. However, the re-dissolution of charged aggregated at high multivalent salt concentrations was shown to be insensitive to monovalent salt.

5.3 Summary

We apply the Modified Gaussian Renormalized Fluctuation Theory to study the phenomenon of ion correlation-driven like-charge attraction. The theory self-consistently captures the effects of inhomogeneous ion correlations on the structure of overlapping double layers and their free energy. The systematic inclusion of correlation in the free energy is key to successfully modeling like-charge attraction. We predict a continuous transition from pure repulsion to short-range attraction as the surface charge density increases. At high surface charges, more ions migrate to the surface, leading to a gain in correlation energy. This attraction is found to be absent for monovalent salts and becomes more pronounced as the counterion valency increases. We demonstrate that overcharging is not a necessary condition for like-charge attraction. Like-charge attraction is observed for both overcharged and normal double layers. Furthermore, our theory is also able to capture the non-monotonic salt concentration dependence of the attractive force as a consequence of the competition between ion correlations and translational entropy. The reduction of attraction at high salt concentrations provides a possible explanation for the long-standing puzzle of reentrant condensation. Our theoretical predictions are in agreement with the simulation and experimental results. Finally, the self-consistent quantification of the essential electrostatic contributions presented here paves the way toward a complete understanding of interfacial forces.

Chapter 6

Long-range opposite charge repulsion in multivalent salt solutions

6.1 Introduction

The electrostatic force between two charged surfaces in the presence of a salt solution is the key to determining equilibrium and non-equilibrium properties in a wide variety of systems related to electrochemistry[193–196], materials science[2, 8, 9], and biology[16–19, 197, 198]. In the classical Derjaguin-Landau-Verwey-Overbeek (DLVO) framework[2], this electrostatic force is described by the mean-field Poisson-Boltzmann (PB) theory, which is long-ranged compared to the short-range Van der Waals attraction. Consistent with physical intuition, mean-field PB predicts a repulsive force between two like-charged surfaces and an attractive force between two oppositely charged surfaces at all separation distances. However, numerous experimental and simulation studies have reported attraction between like-charged surfaces[33, 84–90] and repulsion between oppositely charged surfaces[31, 32, 91–98] in the presence of multivalent salts. The origin of these counter-intuitive phenomena is the electrostatic correlation between ions, the strength of which dominates thermal forces in the case of multivalent ions[32, 87]. Since the mean-field PB does not account for ion-ion correlations, it fails to even qualitatively capture the aforementioned phenomena. While like-charge attraction has been extensively studied by theories beyond mean-field PB[39, 44, 74, 175, 176, 178–183, 185–187], opposite-charge repulsion has received considerably less attention[72, 199]. Understanding opposite-charge repulsion is of great importance, as the interaction between oppositely-charged surfaces is at the core of numerous practical applications like cement formation[10], papermaking[11], food processing[12], and surface patterning[13], as well as biological processes such as protein binding[135, 200, 201] and targeted drug delivery[20, 21].

The force measurements by Besteman et al. provided one of the very first experimental evidence that opposite-charge repulsion is an outcome of ion-ion correlation[31, 91]. They employed an atomic force microscope (AFM) setup to measure the force between a positively-charged amine-terminated surface and a silica bead which originally carries negative charges.

It was found that the force between these two surfaces changes from attractive to repulsive at a critical multivalent salt concentration. This critical concentration strongly depends on the ion valency and weakly depends on the chemical identity of the ions. A similar result has also been observed from the AFM measurements conducted by Borkovec and coworkers[93, 94, 97]. Using Monte-Carlo simulations for the primitive model of electrolytes, Trulsson et al.[32, 92] were able to reproduce these repulsive force curves, thus confirming the purely electrostatic origin of opposite-charge repulsion. It was found that opposite-charge repulsion is long-ranged, acting up to a length scale of a few nanometers. This is quite different from ion correlation-driven like-charge attraction, which occurs at the length scale of a few angstroms[87, 202].

The existing studies have indicated that opposite-charge repulsion is related to another ion-correlation induced phenomenon known as overcharging[44, 161], which is defined as the excess accumulation of counterions near a charged surface. However, the relationship between these two phenomena remains unclear. Trulsson et al.[32] reported that repulsion is accompanied by overcharging at large separations between the two surfaces, but for the same salt concentration at intermediate separations, repulsion can occur without overcharging. These observations suggest that overcharging is not the cause of opposite-charge repulsion. While the simulations of Trulsson et al. were limited to low salt concentrations, it is natural to ask whether this conclusion holds for high salt concentrations as well. Particularly, does the strength of repulsion monotonically increase with salt concentration? This is an important question to ask as the strength of other correlation-induced phenomena like overcharging and like-charge attraction have been shown to depend non-monotonically on salt concentration[30, 64, 88, 144, 202]. Furthermore, it is also desirable to understand how the repulsive force changes with the addition of a a secondary monovalent salt. This is crucial as multivalent and monovalent salt mixtures widely exist in many biological and geological systems[4]. A self-consistent theory accounting for the effect of spatially varying ion-ion correlations on the structure of overlapping double layers and their free energies is needed to answer the above questions and explain the thermodynamic reasoning behind them. Such a coarse-grained description can not only provide an efficient method to explore the complete parameter space but also to calculate long-range forces in electrolyte solutions which could facilitate the development of a fast hybrid molecular dynamics approach.

On the theoretical side, Hatlo and Lue[72] developed a variational approach in the field theoretical framework to model opposite-charge repulsion and overcharging in multivalent salt solutions. Their theory used a point-charge model for the ions, not only overestimating the ion correlations but also ignoring the excluded volume effect of both ions and solvent molecules. They also noted that an arbitrary mathematical operator needs to be introduced to decouple of the short and long-range components of the ion correlations. Although they were able to show good agreement with the simulation results of Trulsson et al.[32] for divalent and trivalent salts, their method failed to predict any repulsion for tetravalent salts, which is inconsistent with the simulation results. Recently, Zhou[199] employed a classical density functional theory (DFT)-based approach and included the contribution of ion correlations to the free energy using second-order perturbation around the bulk density

of ions. This perturbative approach inherently limits the applicability of the method to systems where ion concentrations at the surface are close to the bulk salt concentration. This assumption is not valid if the surface charge density or ion valency is high. Furthermore, DFT theories are computationally challenging and often use density weighting functions that are specific to a particular geometry or system, again limiting its generalization.

An accurate treatment of the spatially varying ion correlations on the structure of overlapping double layers and their free energy is necessary to understand the mechanism behind long-range opposite-charge repulsion. In this chapter, we use the Modified Gaussian Renormalized Fluctuation Theory to study the force between two approaching oppositely charged surfaces immersed in a multivalent salt solution. The force curves calculated by our theory are in quantitative agreement with the simulation results by Trulsson et al.[32] for divalent, trivalent, and tetravalent ions. We also examine the nature of the repulsive force in the entire salt concentration regime and elucidate the relationship between overcharging and opposite-charge repulsion. Furthermore, we investigate how the force change with the addition of monovalent salt to a multivalent salt solution.

6.2 Results and Discussion

In the current work, we study the force between two plates of $\sigma_1 = -0.3204$ C/m^2 and $\sigma_2 = -0.1602$ C/m^2 mediated by pure multivalent salt solutions as well as their mixtures with monovalent salt. We use the primitive model for electrolytes where the dielectric permittivity is assumed to be constant throughout the system and is taken to be that of water at 298 K, i.e., $\varepsilon(\boldsymbol{r}) = 78.7$. These values of surface charges and dielectric permittivity model facilitate direct comparison with simulation results of Trulsson et al.[32]. The born radius of the monovalent anion was fixed at 2.0 Å. For simplicity, we assume that the excluded volume of multivalent cation, monovalent anion, monovalent cation, and the solvent molecule to be the same and equal to $\frac{4}{3}\pi a_+^3$, where a_+ is the born radius of the multivalent cation. As in the previous chapter, the equations and boundary conditions to solve for this system are 2.40 - 2.46, given in Section 2.5. The pressure P between the two surfaces is calculated using

$$P = -\left(\frac{\partial \mathcal{W}}{\partial h}\right)_{\mu_\pm} - P_\mathrm{b} \tag{6.1}$$

where $\mathcal{W}$ is defined in Eq. 2.46 and P_b in Eq. 2.26.

6.2.1 Effect of salt concentration

Figure 5.2 plots the pressure P as a function of the separation distance D between the two surfaces immersed in divalent, trivalent and tetravalent salt solutions, respectively. Our theoretical predictions are in very good quantitative agreement with the simulation results of Trulsson et al.[32] for all the different cation valencies. At low salt concentrations, the ion correlation effect is not significant, the force is universally attractive at all separation

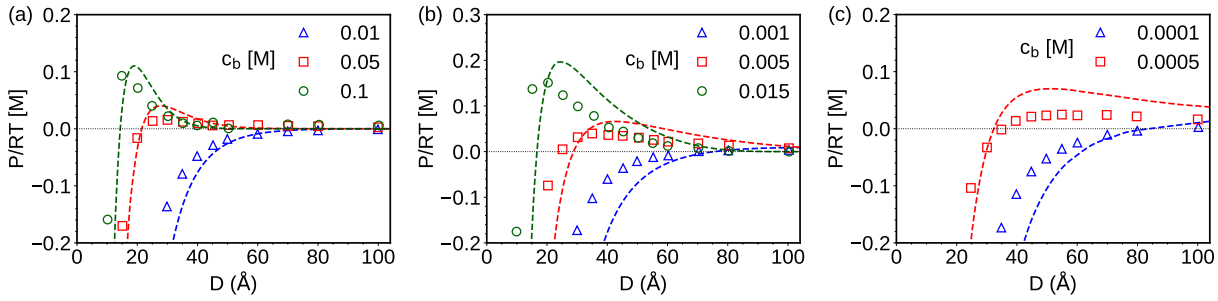

Figure 6.1: Transition from pure attraction to long-range repulsion in overlapping double layers as salt concentration c_b increases. σ_1 = -0.3204 C/m^2, σ_2 = 0.1602 C/m^2, q_- = 1, and a_- = 1.5 Å. The net pressure in molar units between two surfaces as a function of separation distance D for a) $q_+ = 2$ and $a_{+,s} = 1.6$ Å b) $q_+ = 3$ and $a_+ = 2.5$ Å and c) $q_+ = 4$ and $a_+ = 2.5$ Å. Dashed lines represent our theoretical predictions and symbols represent simulation data from Trulsson et al.[32].

distances. This is consistent with the well-known mean-field results of the interactions between two oppositely charged objectives. However, the effect of ion correlations becomes more pronounced as salt concentration increases. The long-range force turns gradually from attraction to repulsion, leading to the emergence of the long-range opposite-charge repulsion. It is worth noting that the force remains attractive at short ranges even in the presence of long-range opposite-charge repulsion. This duality of long-range repulsion and short-range attraction gives rise to a maxima in the pressure curve, which is also in agreement with independent force measurements by Besteman et al.[31, 91] and Borkovec et al.[93, 94, 97]. With only multivalent ion size as an adjustable parameter, we are able to quantitatively capture the pressure curves at both short and long ranges. To our knowledge, this is the first theoretical work in the literature to quantitatively capture these pressure curves for all cation valencies for the entire salt concentration range.

To explore the nature of opposite-charge repulsion at high salt concentrations, pressure profiles from our theory are plotted for pure divalent salt, reaching up to $c_b = 2.0$ M in Figure 6.2a. Increasing salt concentration increases the screening effect and hence the pressure curves can be seen shifting leftwards. Most importantly, the strength of repulsion was found to increase monotonically with salt concentration in stark contrast to ion correlation-driven like-charge attraction whose strength has been shown to depend non-monotonically on multivalent salt concentration[88, 202]. The underlying physics behind these results can be understood by looking at the structure of free energy. The free energy of the system can be divided into two components: a repulsive entropic component and an attractive electrostatic component. When the salt concentrations are very low, say 0.01 M, the entropy loss for ions to come between the two plates is very high, thus there are fewer ions in the

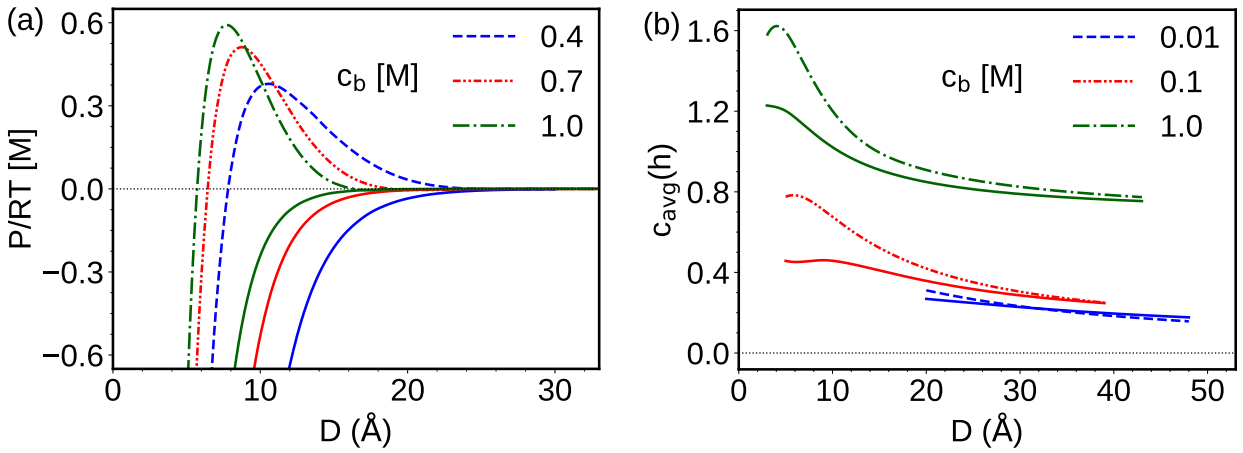

Figure 6.2: Monotonically increasing strength of the repulsive force with multivalent salt concentration. a) The net pressure in molar units between two surfaces as a function of separation distance D for increasing salt concentration c_b. b) Average concentrations in the slit for a given D as predicted by our theory (dashed) and mean-field PB(solid). σ_1 = -0.3204 C/m^2, σ_2 = 0.1602 C/m^2, $q_+ = 2$, $q_- = 1$, and $a_{+,s} = 1.6$ Å.

slit leading to a very low screening of surface charges and strong electrostatic attraction. Increasing c_b from 0.01 M to 0.1 M increases the number of ions in the slit and weakens the long-range attraction because of the enhanced screening effect. This paves the way for entropic repulsion to start dominating electrostatic attraction leading to long-range opposite charge repulsion. With continued increases in salt concentration, the electrostatic attraction becomes weaker and weaker leading to a net stronger repulsive force. The screening of attractive force is significantly higher in the case of multivalent salts compared to monovalent salts because of the ion-ion correlation effect and hence opposite-charge repulsion is only observed in multivalent salts. Similarly, the absence of ion-ion correlations in mean-field PB, solid lines in Figure 6.2a, reduces the number of ions in the slit leading to less screening of the electrostatic attraction and reduced entropic repulsion and thus mean-field PB fails to even qualitatively capture opposite-charge repulsion. This increased ion concentration, as an outcome of ion correlations, is quantified in Figure 6.2b, where the average concentration in the slit for a given separation distance D predicted by both our theory and mean-field PB are plotted. These plots clearly show that the average ion concentrations predicted by our theory progressively increase with bulk salt concentration and are always higher than mean-field PB predictions, except for $c_b = 0.01$ M, for which the force is not attractive. This figure is also in agreement with the analysis of Trulsson et al. [32], who showed that the electrostatic component is universally attractive, whereas the entropic component is universally repulsive and is responsible for opposite-charge repulsion.

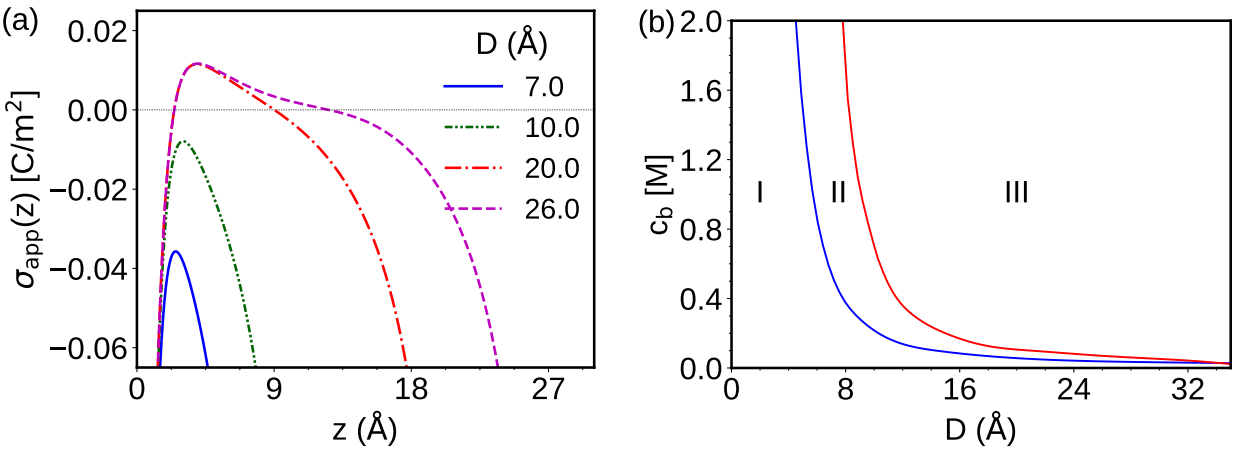

Figure 6.3: Relationship between overcharging and opposite charge repulsion. a) Apparent charge density profiles, $\sigma_{\text{app}}(z) = \sigma_1 + \int_0^z \rho(z^*)dz^*$, where $\rho(z)$ is the local charge density at z, for different separation distance D between the plates for $c_b = 0.4$ M. b) Concentration-separation phase diagram showing different regions of repulsion, attraction and overcharging. I = No overcharging and No repulsion, II = Repulsion with no overcharging, III = Repulsion with overcharging. σ_1 = -0.3204 C/m^2, σ_2 = 0.1602 C/m^2, $q_+ = 2$, $q_- = 1$, and $a_{+,s} = 1.6$ Å for both the plots.

6.2.2 Relationship between overcharging and opposite-charge repulsion

Next, we elucidate the relationship between overcharging and opposite-charge repulsion by plotting the apparent surface charge density of plate 1, $\sigma_{\text{app}}(z) = \sigma_1 + \int_0^z \rho(z^*)dz^*$, for $c_b = 0.4$ M of divalent salt in Figure 6.3a. Here, $\rho(z)$ is the local charge density at distance z from plate 1, where z ranges from [0, D], with D being the separation distance between the two plates. If $\sigma_{\text{app}} > 0$ at any position z, the electrical double layer is considered overcharged. If $\sigma_{\text{app}} < 0$ for all positions z, there is no overcharging in the double layer for that particular separation distance D. Using this definition, in Figure 6.3a, profiles for $h = 7$ and $10, $Å correspond to normal double layers, whereas $h = 20$ and $26, $Å represent overcharged double layers. Furthermore, from the pressure curves for $c_b = 0.4$ M in Figure 6.2a, it can be seen that the force is repulsive at $h = 10, 20$ and $26, $Å and attractive for $h = 7$ Å. The complete c_b vs D phase diagram for a divalent salt, highlighting three different regions of overcharging, opposite-charge repulsion, and opposite-charge attraction, is shown in Figure 6.3b. Region I mostly occupies low separation distances where a strong attraction and no overcharging of plate 1 is observed. To the right of Region I, in Region II at moderate separation distances, our theory predicts opposite-charge repulsion without any overcharging. In Region III, both overcharging and opposite-charge repulsion are obtained.

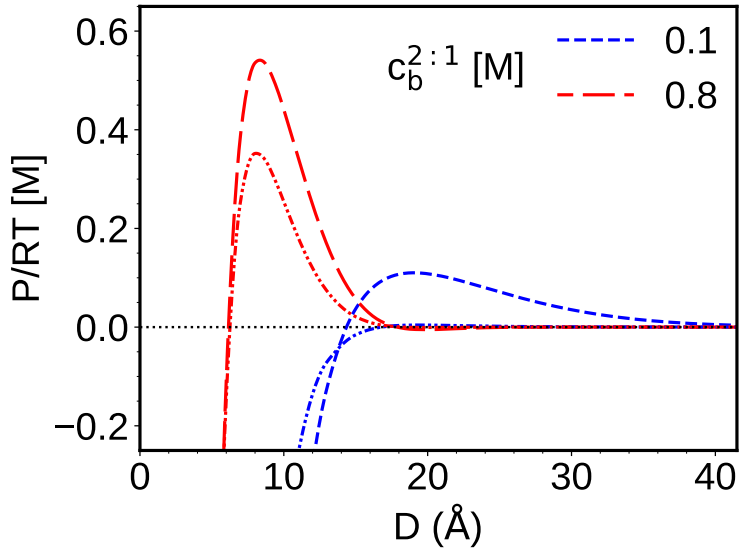

Figure 6.4: The effect of adding 0.5 M monovalent salt to a solution with fixed concentrations of divalent salt $c_b^{2:1}$ on opposite charge repulsion. The dashed lines represent pressure curves for the pure divalent salt solution and the dashed-dot lines represent pressures after monovalent salt is added. σ_1 = -0.3204 C/m^2, σ_2 = 0.1602 C/m^2, and $a_{\pm,s}$ = 2.0 Å.

The existence of regions in the phase diagram showing opposite-charge repulsion with and without overcharging proves that there is no causal relationship between overcharging and opposite-charge repulsion, in agreement with the simulation results of Trulsson et al.[32]. The enhanced strength of ion-ion correlations in multivalent salt solutions increases the number of both counterions and coions between the two plates which could lead to both entropy-induced opposite-charge repulsion as well as overcharging. As the system moves from Region III to Region II the positive plate σ_2 moves closer to negatively charged σ_1 repelling positive multivalent counterions away from the slit leading to the disappearance of overcharging. However, the amount of ions in the slit is still large enough to create a net repulsive force. Finally in Region I, the separation between the plates is so low that the number of ions in the slit is drastically reduced and the bare electrostatic attraction between the surface also becomes very large and we see a net attractive force.

6.2.3 Effect of secondary monovalent salt

The addition of monovalent salt to a system with multivalent salt was found to diminish the strength of opposite-charge repulsion. In Figure 6.4, pressure profiles are plotted for pure divalent salt solutions with $c_b^{2:1}$ = 0.1 M and 0.8 M, as well as for the cases where 0.5 M monovalent salt is added to each of them. At low salt concentrations, for example in the case of $c_b^{2:1}$ = 0.1 M, the addition of monovalent salt could lead to the total disappearance

of the repulsive force. The introduction of monovalent salt reduces the bulk translational entropy of the ions. Consequently, when the two plates come closer, the entropy loss for the system is less, which in turn reduces the strength of the repulsive component of the pressure. Furthermore, because of the low valency of monovalent ions, the ion-ion correlation effect is not strong enough to screen the electrostatic attraction and hence overall we see a reduction in the strength of opposite-charge repulsion.

6.3 Summary

We apply here the Modified Gaussian Renormalized Fluctuation Theory to study the phenomenon of opposite-charge repulsion and its relationship with overcharging for two planar surfaces immersed in a multivalent salt solution. Both opposite-charge repulsion and overcharging are outcomes of ion-ion correlations which play a dominant role in double layers with multivalent counterions. Our theory accurately accounts for the effect of these spatially varying ion-ion correlations on the free energy of such systems in a self-consistent manner. We predict the transition from pure attraction to long-range repulsion and short-range attraction on the addition of multivalent salt, in quantitative agreement with simulations. In an improvement over existing theories, we can capture the pressure curves for not only divalent and trivalent counterions but also for tetravalent ones. The low computational cost of our coarse-grained theory facilitates easy exploration of much broader parameter space. Taking advantage of this, a complete concentration-separation distance phase diagram spanning low to high salt concentrations and small to large separation distances is constructed. We studied the unexplored region of medium and high salt concentrations and found that the strength of opposite-charge repulsion monotonically increases with the addition of multivalent salt. This is an important result as the strength of other ion correlation-induced phenomena like overcharging and like-charge attraction is known to behave non-monotonically with multivalent salt concentration. In line with simulation results, we find regions in which opposite-charge repulsion is observed both with and without overcharging of the double layers. The increased strength of ion-ion correlations in multivalent ions allows more ions to come between the two charged plates leading to higher entropic repulsion and enhanced screening of electrostatic attraction which leads to an overall repulsive force between the two oppositely charged surfaces. The same ion-ion correlations also lead to overaccumulation of counterions in the double layer thus overcharging it. Thus, there is no inherent causal relationship between the two phenomena, however, overcharging is always expected to be followed by opposite-charge repulsion as both are a result of a heightened number of ions in the double layer. We did not find a scenario where overcharging is followed by attraction. Finally, this work, alongside our previous study on ion-correlation-driven like-charge attraction[202], underscores the capability of our Modified Gaussian Renormalized Fluctuation Theory to systematically capture electrical double layer structure and provides a comprehensive understanding of electrostatic forces in the presence of multivalent salt solutions.

Chapter 7

Conclusions and Outlook

Building upon the work of Z.-G. Wang[75], we have developed and demonstrated a new electrolyte solution theory entitled "Modified Gaussian Renormalized Fluctuation Theory." This theory systematically accounts for the effects of spatially varying ion-ion correlations, dielectric permittivity, and the excluded volume effect on the structure and properties of the electrical double layer. A major contribution of this thesis lies in the introduction of a self-consistent scheme to decompose electrostatic correlation into short-range and long-range contributions, addressing ion-ion correlation at two distinct length scales: one associated with ion size (short-range) and the other associated with interface thickness (long-range). In the process, we provide a new expression for the electrostatic component of the solvation-free energy, both in the bulk and at the interface. We also incorporate the excluded volume effect of ions and solvent molecules by including the incompressibility constraint in the partition function. The modified Poisson-Boltzmann nature of the equations (2.12 - 2.15) derived in this work, along with providing a physically intuitive description of the double layer, facilitates the adoption of various numerical methods developed over the last century to solve the highly non-linear exponential problem in diverse geometries. Additionally, we present a novel Sturm-Liouville theory-inspired approach for fast and accurate calculation of the electrostatic correlation function in symmetric geometries. This innovative approach transforms the complex two-dimensional problem into two one-dimensional problems, enhancing computational efficiency and providing spectral convergence with number of modes. An open-source spectral methods-based Python code is also available at https://github.com/nikhil0165.

We have studied several ion correlation-induced phenomena to understand the scope and limitations of the Modified Gaussian Renormalized Fluctuation Theory. One of the first systems modeled was the classical problem of the vapor-liquid interface in ionic fluids. The finite charge spread model for the ion was found to be necessary to accurately describe the short-range correlation and hence the vapor-liquid coexistence curve. The interfacial tension predicted by our theory is in quantitative agreement with simulation data for symmetric salts. We also provide the first theoretical prediction of the interface for an asymmetric salt, where the difference in ion correlation between cations and anions leads to an electrostatic potential profile and local charge separation on both the vapor and liquid sides of the interface.

Next, we applied the theory to model electrical double layers next to strongly charged surfaces in concentrated multivalent salt solutions and investigated the phenomena of overcharging, like-charge attraction, and opposite charge repulsion. The physical origin of overcharging can be characterized using the electrostatic coupling parameter and the phenomena can be divided into weak, moderate and strong coupling regimes. In the weak coupling regime, EDL can be qualitatively described by the mean-field PB. In the moderate coupling regime, PB fails to even qualitatively capture the overcharged EDL, which necessitates a systematic inclusion of correlations. Finally, in the strong-coupling regime, both correlations and excluded volume effects play a significant role in describing crowding. Overcharging is dominated by ion correlations and excluded volume effects, with only a minor contribution from the image force. Our theory is successful in self-consistently unifying the description of overcharging in all three coupling regimes and is the first to discuss the existence of saturation in the degree of overcharging in the strong coupling regime. In a significant improvement over classical density-functional theories and liquid-state Integral equation based methods, we captured the non-monotonic dependence of charge inversion on multivalent salt concentration as well as the addition of monovalent salt, in quantitative agreement with experiments.

In the case of opposite-charge repulsion, by accurately accounting for the effect of spatially varying ion-ion correlations we capture these repulsive forces for divalent, trivalent as well as tetravalent ions in quantitative agreement with simulations. Our theory predicts that the strength of opposite-charge repulsion monotonically increases with salt concentration. The addition of monovalent salt to a multivalent salt solution is found to decrease the strength of the repulsion. Similarly, for like-charge attraction, the addition of monovalent salt reduces attraction, however, unlike opposite-charge repulsion, the strength of attractive force depends non-monotonically on multivalent salt concentration. The reduction of attraction at high salt concentrations could be a contributing factor towards the reentrant stability of charged colloidal suspensions observed in experiments and simulations. Most importantly, we demonstrate that overcharging, like-charge attraction, and opposite-charge repulsion are outcomes of ion-ion correlations, often occurring under similar conditions, but without a causal relationship with each other.

Looking ahead, several promising directions emerge for future research. Being a field-theoretic formulation, our theory can be easily incorporated as the electrostatic component to study the structure and dynamic behaviors in a variety of soft matter, biophysical, and electrochemical systems. Our Modified Gaussian Renormalized Fluctuation Theory can be combined with self-consistent field theory for polyelectrolytes to understand their morphology and mechanical response to the addition of multivalent salts[14, 135, 203]. Equation 2.27 essentially gives an expression of chemical potential for ions in systems where ion-ion correlations and excluded volume of molecules are expected to play a significant role. This expression for chemical potential can be used in the diffusion term of the Poisson-Nernst-Planck equations to study dynamic phenomena like charging of electrical double layers[6], electroconvection[204], diffusiophoresis, and diffusioosmosis[205]. Similarly, our theory can improve the potential of mean force calculations for ion permeation in biological ion channels. This could be particularly important for the transport of Ca^{2+} and Mg^{2+}, where the

electrostatic potential profile inside the channel induced by the surrounding baths cannot be accurately modeled using mean-field PB[206, 207]. On a more ambitious side, the ability of our theory to model electrostatic force between two charged surfaces could be used to develop an efficient hybrid molecular dynamics approach. Pursuing these projects would also require developing efficient computational methods to solve these highly non-linear equations for asymmetric geometries.

Finally, it is essential to acknowledge the limitations of our theory. A major drawback is that the reference state chosen to estimate the free energy in the Gibbs-Feynman-Bogoliubov inequality takes on a Gaussian form. Consequently, the theory may be insufficient to describe systems where higher-order correlations dominate. Examples include electrolyte solutions at low temperatures [208] or ionic liquids[209, 210], where ion clusters play a critical role. Furthermore, the integral over the field ξ, which enforces the incompressibility constraint, is evaluated in the saddle point limit. This is expected to produce quantitative errors in conditions where the double layer is highly crowded or ion sizes are very large. Nevertheless, as demonstrated in this thesis, the ability of our theory to quantitatively capture various ion-correlation-induced phenomena underscores that accounting for electrostatic correlations at the Gaussian level is generally sufficient to model most practical electrolyte systems.

Bibliography

[1] J. Newman and N. P. Balsara, *Electrochemical systems, 4th ed.* (John Wiley & Sons: Hoboken, NJ, USA, 2021).

[2] J. N. Israelachvili, *Intermolecular and surface forces* (Academic press: New York, 2011).

[3] R. Messina, "Electrostatics in soft matter," J. Condens. Matter Phys. **21**, 113102 (2009).

[4] Y. Levin, "Electrostatic correlations: From plasma to biology," Rep. Prog. Phys. **65**, 1577–1632 (2002).

[5] M. V. Fedorov and A. A. Kornyshev, "Ionic liquids at electrified interfaces," Chem. Rev. **114**, 2978–3036 (2014).

[6] J. Wu, "Understanding the electric double-layer structure, capacitance, and charging dynamics," Chem. Rev. **122**, 10821–10859 (2022).

[7] R. B. Schoch, J. Han, and P. Renaud, "Transport phenomena in nanofluidics," Rev. Mod. Phys **80**, 839–883 (2008).

[8] A. E. Larsen and D. G. Grier, "Like-charge attractions in metastable colloidal crystallites," Nature **385**, 230–233 (1997).

[9] A. D. Dinsmore, J. C. Crocker, and A. G. Yodh, "Self-assembly of colloidal crystals," Curr. Opin. Colloid Interface Sci. **3**, 5–11 (1998).

[10] L. Ferrari, J. Kaufmann, F. Winnefeld, and J. Plank, "Interaction of cement model systems with superplasticizers investigated by atomic force microscopy, zeta potential, and adsorption measurements," J. Colloid Interface Sci. **347**, 15–24 (2010).

[11] S. Varennes and T. Van De Ven, "Effects of polyelectrolyte on the deposition and detachment of colloidal particles subjected to flow," Colloids Surf. **33**, 63–74 (1988).

[12] D. Guzey and D. J. McClements, "Formation, stability and properties of multilayer emulsions for application in the food industry," Adv. Colloid Interface Sci. **128-130**, 227–248 (2006).

[13] H. Agheli, J. Malmström, E. M. Larsson, M. Textor, and D. S. Sutherland, "Large area protein nanopatterning for biological applications," Nano Lett. **6**, 1165–1171 (2006).

[14] C. E. Sing, J. W. Zwanikken, and M. Olvera De La Cruz, "Electrostatic control of block copolymer morphology," Nat. Mater. **13**, 694–698 (2014).

[15] J. Yu, N. E. Jackson, X. Xu, Y. Morgenstern, Y. Kaufman, M. Ruths, J. J. de Pablo, and M. Tirrell, "Multivalent counterions diminish the lubricity of polyelectrolyte brushes," Science **360**, 1434–1438 (2018).

[16] C. Caccamo, G. Pellicane, and D. Costa, "Phase transitions in hard-core yukawa fluids: toward a theory of phase stability in protein solutions," J. Phys. Condens. Matter **12**, A437–A442 (2000).

[17] J. C. Butler, T. Angelini, J. X. Tang, and G. C. Wong, "Ion Multivalence and Like-Charge Polyelectrolyte Attraction," Phys. Rev. Lett. **91** (2003).

[18] F. Zhang, M. W. A. Skoda, R. M. J. Jacobs, S. Zorn, R. A. Martin, C. M. Martin, G. F. Clark, S. Weggler, A. Hildebrandt, O. Kohlbacher, and F. Schreiber, "Reentrant condensation of proteins in solution induced by multivalent counterions," Phys. Rev. Lett. **101**, 148101 (2008).

[19] R. Nassar, G. L. Dignon, R. M. Razban, and K. A. Dill, "The Protein Folding Problem: The Role of Theory," J. Mol. Biol. **433** (2021).

[20] W. M. Gelbart, R. F. Bruinsma, P. A. Pincus, and V. Adrian Parsegian, "DNA-Inspired Electrostatics," Phys. Today **53**, 38 (2007).

[21] F. J. Solis and M. O. d. l. Cruz, "Flexible Polymers Also Counterattract," Phys. Today **54**, 71 (2007).

[22] D. A. Doyle, J. M. Cabral, R. A. Pfuetzner, A. Kuo, J. M. Gulbis, S. L. Cohen, B. T. Chait, and R. MacKinnon, "The structure of the potassium channel: Molecular basis of K+ conduction and selectivity," Science **280**, 69–77 (1998).

[23] E. Gouaux and R. MacKinnon, "Principles of selective ion transport in channels and pumps," Science **310**, 1461–1465 (2005).

[24] L. Tang, T. M. Gamal El-Din, J. Payandeh, G. Q. Martinez, T. M. Heard, T. Scheuer, N. Zheng, and W. A. Catterall, "Structural basis for Ca2+ selectivity of a voltage-gated calcium channel," Nature **505**, 56–61 (2014).

[25] S. Sakipov, A. I. Sobolevsky, and M. G. Kurnikova, "Ion Permeation Mechanism in Epithelial Calcium Channel TRVP6," Sci. Rep. **8**, 1–13 (2018).

[26] C. Maffeo, S. Bhattacharya, J. Yoo, D. Wells, and A. Aksimentiev, "Modeling and simulation of ion channels," Chem. Rev. **112**, 6250–6284 (2012).

[27] B. Z. Lu, Y. C. Zhou, M. J. Holst, and J. A. Mccammon, "Recent Progress in Numerical Methods for the Poisson-Boltzmann Equation in Biophysical Applications," Commun. Comput. Phys. **3**, 973–1009 (2008).

[28] Z.-G. Wang, "Variational methods in statistical thermodynamics—a pedagogical introduction," in *Variational Methods in Molecular Modeling*, edited by J. Wu (Springer Singapore, Singapore, 2017) pp. 1–29.

[29] M. E. Fisher and Y. Levin, "Criticality in ionic fluids: Debye-hückel theory, bjerrum, and beyond," Phys. Rev. Lett. **71**, 3826–3829 (1993).

[30] F. H. Van Der Heyden, D. Stein, K. Besteman, S. G. Lemay, and C. Dekker, "Charge inversion at high ionic strength studied by streaming currents," Phys. Rev. Lett. **96**, 224502 (2006).

[31] K. Besteman, M. A. Zevenbergen, H. A. Heering, and S. G. Lemay, "Direct observation of charge inversion by multivalent ions as a universal electrostatic phenomenon," Phys. Rev. Lett. **93**, 170802 (2004).

[32] M. Trulsson, B. Jönsson, T. Åkesson, J. Forsman, and C. Labbez, "Repulsion between oppositely charged surfaces in multivalent electrolytes," Phys. Rev. Lett. **97** (2006).

[33] P. Kékicheff, S. Marčelja, T. J. Senden, and V. E. Shubin, "Charge reversal seen in electrical double layer interaction of surfaces immersed in 2:1 calcium electrolyte," J. Chem. Phys. **99**, 6098 (1993).

[34] Z. Tang, L.Mier-Y-Teran, H. Davis, L. Scriven, and H. White, "Non-local free-energy density-functional theory applied to the electrical double layer," Mol. Phys. **71**, 369–392 (1990).

[35] L.Mier-Y-Teran, Z. Tang, H. Davis, L. Scriven, and H. White, "Non-local free-energy density-functional theory applied to the electrical double layer," Mol. Phys. **72**, 817–830 (1991).

[36] E. Waisman and J. L. Lebowitz, "Mean spherical model integral equation for charged hard spheres. ii. results," J. Chem. Phys. **56**, 3093–3099 (1972).

[37] I. Rouzina and V. A. Bloomfield, "Macroion attraction due to electrostatic correlation between screening counterions. 1. mobile surface-adsorbed ions and diffuse ion cloud," J. Phys. Chem. **100**, 9977–9989 (1996).

[38] R. R. Netz, "Debye-Hückel theory for slab geometries," Eur. Phys. J. E **3**, 131–141 (2000).

[39] R. R. Netz and H. Orland, "Beyond Poisson-Boltzmann: Fluctuation effects and correlation functions," Eur. Phys. J. E **1**, 203–214 (2000).

[40] R. R. Netz, "Electrostatistics of counter-ions at and between planar charged walls: From Poisson-Boltzmann to the strong-coupling theory," Eur. Phys. J. E **5**, 557–574 (2001).

[41] R. R. Netz and H. Orland, "Variational charge renormalization in charged systems," Eur. Phys. J. E **11**, 301–311 (2003).

[42] A. Martín-Molina, M. Quesada-Pérez, F. Galisteo-González, and R. Hidalgo-Álvarez, "Looking into overcharging in model colloids through electrophoresis: Asymmetric electrolytes," J. Chem. Phys. **118**, 4183–4189 (2003).

[43] A. Martín-Molina, J. A. Maroto-Centeno, R. Hidalgo-Álvarez, and M. Quesada-Pérez, "Charge reversal in real colloids: Experiments, theory and simulations," Colloids Surf., A **319**, 103–108 (2008).

[44] A. Y. Grosberg, T. T. Nguyen, and B. I. Shklovskii, "Colloquium: The physics of charge inversion in chemical and biological systems," Rev. Mod. Phys. **74**, 329–345 (2002).

[45] S. Pianegonda, M. C. Barbosa, and Y. Levin, "Charge reversal of colloidal particles," Europhys. Lett. **71**, 831–837 (2005).

[46] F. Jiménez-Ángeles and M. Lozada-Cassou, "On the regimes of charge reversal," Mol. Phys. **128**, 174701 (2008).

[47] S. Y. Mashayak and N. R. Aluru, "A multiscale model for charge inversion in electric double layers," J. Chem. Phys. **148**, 214102 (2018).

[48] A. P. dos Santos, A. Diehl, and Y. Levin, "Colloidal charge renormalization in suspensions containing multivalent electrolyte," J. Chem. Phys. **132**, 104105 (2010).

[49] S. Buyukdagli and R. Blossey, "Beyond poisson–boltzmann: fluctuations and fluid structure in a self-consistent theory," J. Phys. Condens. Matter **28**, 343001 (2016).

[50] A. Gupta, A. Govind Rajan, E. A. Carter, and H. A. Stone, "Ionic Layering and Overcharging in Electrical Double Layers in a Poisson-Boltzmann Model," Phys. Rev. Lett. **125**, 188004–188005 (2020).

[51] M. Quesada-Pérez, E. González-Tovar, A. Martín-Molina, M. Lozada-Cassou, and R. Hidalgo-Álvarez, "Overcharging in Colloids: Beyond the Poisson–Boltzmann Approach," ChemPhysChem **4**, 234–248 (2003).

[52] A. W. C. Lau, "Fluctuation and correlation effects in a charged surface immersed in an electrolyte solution," Phys. Rev. E **77**, 011502 (2008).

[53] M. Z. Bazant, B. D. Storey, and A. A. Kornyshev, "Double layer in ionic liquids: Overscreening versus crowding," Phys. Rev. Lett. **106**, 046102 (2011).

[54] D. Gillespie, A. S. Khair, J. P. Bardhan, and S. Pennathur, "Efficiently accounting for ion correlations in electrokinetic nanofluidic devices using density functional theory," J. Colloid Interface Sci. **359**, 520–529 (2011).

[55] Y. Avni, R. M. Adar, and D. Andelman, "Charge oscillations in ionic liquids: A microscopic cluster model," Phys. Rev. E **101**, 010601 (2020).

[56] F. Jiménez-Ángeles, R. Messina, C. Holm, and M. Lozada-Cassou, "Ion pairing in model electrolytes: A study via three-particle correlation functions," J. Chem. Phys. **119**, 4842–4856 (2003).

[57] J. Hoffmann and D. Gillespie, "Ion correlations in nanofluidic channels: Effects of ion size, valence, and concentration on voltage- and pressure-driven currents," Langmuir **29**, 1303–1317 (2013).

[58] M. Valiskó, T. Kristóf, D. Gillespie, and D. Boda, "A systematic Monte Carlo simulation study of the primitive model planar electrical double layer over an extended range of concentrations, electrode charges, cation diameters and valences," AIP Adv. **8**, 025320 (2018).

[59] L. Lue, "A variational field theory for solutions of charged, rigid particles," Fluid Ph. Equilibria **241**, 236–247 (2006).

[60] M. M. Hatlo and L. Lue, "A field theory for ions near charged surfaces valid from weak to strong couplings," Soft Matter **5**, 125–133 (2009).

[61] S. Buyukdagli, M. Manghi, and J. Palmeri, "Variational approach for electrolyte solutions: From dielectric interfaces to charged nanopores," Phys. Rev. E **81**, 041601 (2010).

[62] S. Buyukdagli, M. Manghi, and J. Palmeri, "Ionic capillary evaporation in weakly charged nanopores," Phys. Rev. Lett. **105**, 158103 (2010).

[63] R. Evans, "Density Functionals in the Theory of Non-Uniform Fluids," in *Fundamentals of Inhomogeneous Fluids*, edited by D. Henderson (Marcel Dekker, 1992) pp. 85–175.

[64] N. R. Agrawal and R. Wang, "Non-monotonic salt concentration dependence of inverted electrokinetic flow," AIChE Journal , e18269 (2023).

[65] Y. Rosenfeld, M. Schmidt, H. Löwen, and P. Tarazona, "Fundamental-measure free-energy density functional for hard spheres: Dimensional crossover and freezing," Phys. Rev. E **55**, 4245–4263 (1997).

[66] D. Gillespie, "Free-energy density functional of ions at a dielectric interface," J. Phys. Chem. Lett **2**, 1178–1182 (2011).

[67] B. I. Shklovskii, "Screening of a macroion by multivalent ions: Correlation-induced inversion of charge," Phys. Rev. E **60**, 5802–5811 (1999).

[68] V. Perel and B. Shklovskii, "Screening of a macroion by multivalent ions: a new boundary condition for the Poisson–Boltzmann equation and charge inversion," Phys. A (Amsterdam, Neth.) **274**, 446–453 (1999).

[69] B. D. Storey and M. Z. Bazant, "Effects of electrostatic correlations on electrokinetic phenomena," Phys. Rev. E **86**, 56303 (2012).

[70] A. W. Lau, D. B. Lukatsky, P. Pincus, and S. A. Safran, "Charge fluctuations and counterion condensation," Phys. Rev. E **65**, 7 (2002).

[71] A. W. Lau and P. Pincus, "Counterion condensation and fluctuation-induced attraction," Phys. Rev. E **66**, 14 (2002).

[72] M. M. Hatlo and L. Lue, "A field theory for ions near charged surfaces valid from weak to strong couplings," Soft Matter **5**, 125–133 (2009).

[73] S. Buyukdagli, M. Manghi, and J. Palmeri, "Variational approach for electrolyte solutions: From dielectric interfaces to charged nanopores," Phys. Rev. E **81**, 041601 (2010).

[74] S. Buyukdagli, "Like-charge attraction and opposite-charge decomplexation between polymers and DNA molecules," Phys. Rev. E **95**, 22502 (2017).

[75] Z. G. Wang, "Fluctuation in electrolyte solutions: The self energy," Phys. Rev. E **81**, 021501 (2010).

[76] M. E. Fisher, J.-N. Aqua, and S. Banerjee, "How multivalency controls ionic criticality," Phys. Rev. Lett. **95**, 135701 (2005).

[77] Q. Yan and J. J. de Pablo, "Hyper-parallel tempering monte carlo: Application to the lennard-jones fluid and the restricted primitive model," J. Chem. Phys. **111**, 9509–9516 (1999).

[78] G. Orkoulas and A. Z. Panagiotopoulos, "Phase behavior of the restricted primitive model and square-well fluids from Monte Carlo simulations in the grand canonical ensemble," J. Chem. Phys. **110**, 1581–1590 (1999).

[79] J.-M. Caillol, D. Levesque, and J.-J. Weis, "Critical behavior of the restricted primitive model revisited," J. Chem. Phys. **116**, 10794–10800 (2002).

[80] M. González-Melchor, J. Alejandre, and F. Bresme, "Surface Tension of the Restrictive Primitive Model for Ionic Liquids," Phys. Rev. Lett. **90**, 4 (2003).

[81] J. Alejandre, F. Bresme, and M. Gonzalez-Melchor, "Interfacial properties of charge asymmetric ionic liquids," Mol. Phys. **107**, 357–363 (2009).

[82] M. González-Melchor, F. Bresme, and J. Alejandre, "Molecular dynamics simulations of the surface tension of ionic liquids," J. Chem. Phys. **122**, 338 (2005).

[83] A. Kubíčková, T. c. v. Křížek, P. Coufal, M. Vazdar, E. Wernersson, J. Heyda, and P. Jungwirth, "Overcharging in biological systems: Reversal of electrophoretic mobility of aqueous polyaspartate by multivalent cations," Phys. Rev. Lett. **108**, 186101 (2012).

[84] O. Zohar, I. Leizerson, and U. Sivan, "Short range attraction between two similarly charged silica surfaces," Phys. Rev. Lett. **96** (2006).

[85] S. Kumar, I. Yadav, S. Abbas, V. K. Aswal, and J. Kohlbrecher, "Interactions in reentrant phase behavior of a charged nanoparticle solution by multivalent ions," Phys. Rev. E **96**, 60602 (2017).

[86] P. Linse and V. Lobaskin, "Electrostatic attraction and phase separation in solutions of like-charged colloidal particles," Phys. Rev. Lett. **83**, 4208–4211 (1999).

[87] P. Linse and V. Lobaskin, "Electrostatic attraction and phase separation in solutions of like-charged colloidal particles," J. Chem. Phys **112**, 3917–3927 (2000).

[88] J. Z. Wu, D. Bratko, H. W. Blanch, and J. M. Prausnitz, "Monte Carlo simulation for the potential of mean force between ionic colloids in solutions of asymmetric salts," J. Chem. Phys **111**, 7084–7094 (1999).

[89] D. G. Angelescu and P. Linse, "Monte carlo simulation of the mean force between two like-charged macroions with simple 1: 3 salt added," Langmuir **19**, 9661–9668 (2003).

[90] X. Zhang, J. S. Zhang, Y. Z. Shi, X. L. Zhu, and Z. J. Tan, "Potential of mean force between like-charged nanoparticles: Many-body effect," Sci. Rep **6**, 1–12 (2016).

[91] K. Besteman, M. A. G. Zevenbergen, and S. G. Lemay, "Charge inversion by multivalent ions: Dependence on dielectric constant and surface-charge density," Phys. Rev. E **72** (2005).

[92] M. Trulsson, B. Jönsson, T. Åkesson, J. Forsman, and C. Labbez, "Repulsion between oppositely charged macromolecules or particles," Langmuir **23**, 11562–11569 (2007).

[93] I. Popa, P. Sinha, M. Finessi, P. Maroni, G. Papastavrou, and M. Borkovec, "Importance of charge regulation in attractive double-layer forces between dissimilar surfaces," Phys. Rev. Lett. **104**, 228301–228302 (2010).

[94] F. J. Montes Ruiz-Cabello, G. Trefalt, P. Maroni, and M. Borkovec, "Accurate predictions of forces in the presence of multivalent ions by poisson–boltzmann theory," Langmuir **30**, 4551–4555 (2014).

[95] H. S. Antila, P. R. Van Tassel, and M. Sammalkorpi, "Interaction modes between asymmetrically and oppositely charged rods," Phys. Rev. E **93**, 022602 (2016).

[96] H. S. Antila, P. R. Van Tassel, and M. Sammalkorpi, "Repulsion between oppositely charged rod-shaped macromolecules: Role of overcharging and ionic confinement," J. Chem. Phys. **147** (2017).

[97] M. Moazzami-Gudarzi, a. Pavel Adam, A. M. Smith, G. Trefalt, I. Szilá gyi, P. Maroni, and M. Borkovec, "Cite this," Phys. Chem. Chem. Phys **20**, 9436 (2018).

[98] C. Lin, X. Zhang, X. Qiang, J. S. Zhang, and Z. J. Tan, "Apparent repulsion between equally and oppositely charged spherical polyelectrolytes in symmetrical salt solutions," J. Chem. Phys. **151**, 114902 (2019).

[99] R. Asor, O. Ben-Nun-Shaul, A. Oppenheim, and U. Raviv, "Crystallization, Reentrant Melting, and Resolubilization of Virus Nanoparticles," ACS Nano **11**, 9814–9824 (2017).

[100] J. Pelta, F. Livolant, and J.-L. Sikorav, "Dna aggregation induced by polyamines and cobalthexamine," J. Biol. Chem **271**, 5656–5662 (1996).

[101] R. Wang and Z. G. Wang, "Effects of image charges on double layer structure and forces," J. Chem. Phys. **139**, 124702 (2013).

[102] R. Wang and Z. G. Wang, "On the theoretical description of weakly charged surfaces," J. Chem. Phys. **142**, 104705 (2015).

[103] I. Borukhov, D. Andelman, and H. Orland, "Steric effects in electrolytes: A modified poisson-boltzmann equation," Phys. Rev. Lett. **79**, 435–438 (1997).

[104] G. Fredrickson, *The Equilibrium Theory of Inhomogeneous Polymers* (Oxford University Press, 2005).

[105] Z. Xu and A. C. Maggs, "Solving fluctuation-enhanced Poisson-Boltzmann equations," J. Comput. Phys. **275**, 310–322 (2014).

[106] K. J. Burns, G. M. Vasil, J. S. Oishi, D. Lecoanet, and B. P. Brown, "Dedalus: A flexible framework for numerical simulations with spectral methods," Phys. Rev. Res. **2**, 023068 (2020).

[107] J. P. Boyd, *Chebyshev and Fourier spectral methods* (Courier Corporation, 2001).

[108] G. M. Vasil, K. J. Burns, D. Lecoanet, S. Olver, B. P. Brown, and J. S. Oishi, "Tensor calculus in polar coordinates using jacobi polynomials," J. Comput. Phys. **325**, 53–73 (2016).

[109] D. Lecoanet, G. M. Vasil, K. J. Burns, B. P. Brown, and J. S. Oishi, "Tensor calculus in spherical coordinates using jacobi polynomials. part-ii: Implementation and examples," J. Comput. Phys.: X **3**, 100012 (2019).

[110] G. M. Vasil, D. Lecoanet, K. J. Burns, J. S. Oishi, and B. P. Brown, "Tensor calculus in spherical coordinates using jacobi polynomials. part-i: Mathematical analysis and derivations," J. Comput. Phys.: X **3**, 100013 (2019).

[111] M. Buback and E. Franck, "Measurements of the vapour pressures and critical data of ammonium halides," Berichte der Bunsengesellschaft für physikalische Chemie **76**, 350–354 (1972).

[112] M. E. Fisher, "The story of coulombic critiality," J. Stat. Phys. **75**, 1–36 (1994).

[113] W. Schröer, "A Short History of Phase Transitions in Ionic Fluids," Contrib. Plasma Phys. **52**, 78–88 (2012).

[114] V. C. Weiss and W. Schröer, "Relevance of the local-density approximation to interfacial properties of ionic fluids within gradient theory," J. Phys. Condens. Matter **10**, L705–L710 (1998).

[115] B. Groh, R. Evans, and S. Dietrich, "Liquid-vapor interface of an ionic fluid," Phys. Rev. E **57**, 6944–6954 (1998).

[116] A. Patrykiejew, S. Sokołowski, and O. Pizio, "The liquid-vapor interface of the restricted primitive model of ionic fluids from a density functional approach," Condens. Matter Phys. **14**, 1–12 (2011).

[117] M. M. Telo Da Gama, R. Evans, and T. J. Sluckin, "The structure and surface tension of the liquid-vapour interface of a model of a molten salt," Mol. Phys. **41**, 1355–1372 (1980).

[118] V. C. Weiss and W. Schröer, "The liquid-vapour interface of the restricted primitive model (RPM) of ionic fluids," J. Phys. Condens. Matterr **12**, 2637–2655 (2000).

[119] B. P. Lee and M. E. Fisher, "Density fluctuations in an electrolyte from generalized debye-hückel theory," Phys. Rev. Lett. **76**, 2906–2909 (1996).

[120] N. R. Agrawal and R. Wang, "Electrostatic Correlation Induced Ion Condensation and Charge Inversion in Multivalent Electrolytes," J. Chem. Theory Comput. **18**, 6280 (2022).

[121] J. M. Caillol, D. Levesque, and J. J. Weis, "A monte carlo finite size scaling study of charged hard-sphere criticality," J. Chem. Phys. **107**, 1565–1575 (1997).

[122] G. Orkoulas and A. Z. Panagiotopoulos, "Free energy and phase equilibria for the restricted primitive model of ionic fluids from Monte Carlo simulations," J. Chem. Phys. **101**, 1452–1459 (1994).

[123] R. Wang and Z.-G. Wang, "Effects of ion solvation on phase equilibrium and interfacial tension of liquid mixtures," J. Chem. Phys. **135**, 014707 (2011).

[124] C. E. Sing, J. W. Zwanikken, and M. O. de la Cruz, "Interfacial behavior in polyelectrolyte blends: Hybrid liquid-state integral equation and self-consistent field theory study," Phys. Rev. Lett. **111**, 168303 (2013).

[125] K. J. Hou and J. Qin, "Solvation and Entropic Regimes in Ion-Containing Block Copolymers," Macromolecules **51**, 7463–7475 (2018).

[126] P. Y. Hsiao, "Overcharging, charge inversion, and reentrant condensation: Using highly charged polyelectrolytes in tetravalent salt solutions as an example of study," J. Phys. Chem. B **112**, 7347–7350 (2008).

[127] I. Semenov, S. Raafatnia, M. Sega, V. Lobaskin, C. Holm, and F. Kremer, "Electrophoretic mobility and charge inversion of a colloidal particle studied by single-colloid electrophoresis and molecular dynamics simulations," Phys. Rev. E **87**, 022302 (2013).

[128] K. Lin, C. Y. Lin, J. W. Polster, Y. Chen, and Z. S. Siwy, "Charge Inversion and Calcium Gating in Mixtures of Ions in Nanopores," J. Am. Chem. Soc. **142**, 2925–2934 (2020).

[129] S. Buyukdagli, R. Blossey, and T. Ala-Nissila, "Ionic current inversion in pressure-driven polymer translocation through nanopores," Phys. Rev. Lett. **114**, 088303 (2015).

[130] Y. He, D. Gillespie, D. Boda, I. Vlassiouk, R. S. Eisenberg, and Z. S. Siwy, "Tuning transport properties of nanofluidic devices with local charge inversion," J. Am. Chem. Soc. **131**, 5194–5202 (2009).

[131] B. Luan and A. Aksimentiev, "Control and reversal of the electrophoretic force on dna in a charged nanopore," J. Phys. Condens. Matter **22**, 454123 (2010).

[132] S. Buyukdagli and T. Ala-Nissila, "Controlling polymer translocation and ion transport via charge correlations," Langmuir **30**, 12907–12915 (2014).

[133] P. L. Felgner, "Nonviral Strategies for as therapies and as vaccines Gene Therapy," Sci. Am. **276**, 102–106 (1997).

[134] K. Besteman, K. Van Eijk, and S. G. Lemay, "Charge inversion accompanies DNA condensation by multivalent ions," Nat. Phys. **3**, 641–644 (2007).

[135] H. Schiessel, "The physics of chromatin," J. Phys. Condens. Matter **15**, R699 (2003).

[136] J. Lyklema, "Overcharging, charge reversal: Chemistry or physics?" Colloids Surf., A **291**, 3–12 (2006).

[137] W. M. de Vos and S. Lindhoud, "Overcharging and charge inversion: Finding the correct explanation(s)," Adv. Colloid Interface Sci. **274**, 102040 (2019).

[138] A. Diehl and Y. Levin, "Smoluchowski equation and the colloidal charge reversal," J. Chem. Phys. **125**, 054902 (2006).

[139] A. Diehl and Y. Levin, "Colloidal charge reversal: Dependence on the ionic size and the electrolyte concentration," J. Chem. Phys. **129**, 124506 (2008).

[140] A. Martín-Molina, C. Rodríguez-Beas, R. Hidalgo-Álvarez, and M. Quesada-Pérez, "Effect of surface charge on colloidal charge reversal," J. Phys. Chem. B **113**, 6834–6839 (2009).

[141] A. A. Kornyshev, "Double-layer in ionic liquids: Paradigm change?" J. Phys. Chem. B **111**, 5545–5557 (2007).

[142] M. Mezger, H. Schröder, H. Reichert, S. Schramm, J. S. Okasinski, S. Schöder, V. Honkimäki, M. Deutsch, B. M. Ocko, J. Ralston, M. Rohwerder, M. Stratmann, and H. Dosch, "Molecular layering of fluorinated ionic liquids at a charged sapphire (0001) surface," Science **322**, 424–428 (2008).

[143] J. P. de Souza, Z. A. H. Goodwin, M. McEldrew, A. A. Kornyshev, and M. Z. Bazant, "Interfacial layering in the electric double layer of ionic liquids," Phys. Rev. Lett. **125**, 116001 (2020).

[144] P. Y. Hsiao and E. Luijten, "Salt-induced collapse and reexpansion of highly charged flexible polyelectrolytes," Phys. Rev. Lett. **97**, 148301 (2006).

[145] O. Lenz and C. Holm, "Simulation of charge reversal in salty environments: Giant overcharging?" Eur. Phys. J. E **26**, 191–195 (2008).

[146] M. Quesada-Pérez, A. Martín-Molina, and R. Hidalgo-Álvarez, "Simulation of electric double layers undergoing charge inversion: Mixtures of mono- and multivalent ions," Langmuir **21**, 9231–9237 (2005).

[147] A. Martín-Molina, M. Quesada-Pérez, F. Galisteo-González, and R. Hidalgo-Álvarez, "Electrophoretic mobility and primitive models: Surface charge density effect," J. Phys. Chem. B **106**, 6881–6886 (2002).

[148] T. T. Nguyen, A. Y. Grosberg, and B. I. Shklovskii, "Macroions in salty water with multivalent ions: giant inversion of charge," Phys. Rev. Lett. **85**, 1568–1571 (2000).

[149] T. T. Nguyen, I. Rouzina, and B. I. Shklovskii, "Reentrant condensation of DNA induced by multivalent counterions," J. Chem. Phys. **112**, 7298 (2000).

[150] B. I. Shklovskii, "Wigner crystal model of counterion induced bundle formation of rodlike polyelectrolytes," Phys. Rev. Lett. **82**, 3268–3271 (1999).

[151] A. G. Moreira and R. R. Netz, "Strong-coupling theory for counter-ion distributions," Europhys. Lett. **52**, 705–711 (2000).

[152] F. Jiménez-Ángeles and M. Lozada-Cassou, "A model macroion solution next to a charged wall: Overcharging, charge reversal, and charge inversion by macroions," J. Phys. Chem. B **108**, 7286–7296 (2004).

[153] Y.-X. Yu, J. Wu, and G.-H. Gao, "Density-functional theory of spherical electric double layers and ζ potentials of colloidal particles in restricted-primitive-model electrolyte solutions," J. Chem. Phys. **120**, 7223–7233 (2004).

[154] J. Wu and Z. Li, "Density-functional theory for complex fluids," Annu. Rev. Phys. Chem. **58**, 85–112 (2007).

[155] D. Gillespie, W. Nonner, and R. S. Eisenberg, "Coupling poisson–nernst–planck and density functional theory to calculate ion flux," J. Phys. Condens. Matter **14**, 12129 (2002).

[156] D. Gillespie, "A review of steric interactions of ions: Why some theories succeed and others fail to account for ion size," Microfluid. Nanofluidics **18**, 717–738 (2015).

[157] M. Tanaka and A. Y. Grosberg, "Electrophoresis of a charge-inverted macroion complex: Molecular-dynamics study," Eur. Phys. J. E **7**, 371–379 (2002).

[158] A. Naji, M. Kanduč, J. Forsman, and R. Podgornik, "Perspective: Coulomb fluids—weak coupling, strong coupling, in between and beyond," J. Chem. Phys. **139**, 150901 (2013).

[159] A. Voukadinova and D. Gillespie, "Energetics of counterion adsorption in the electrical double layer," J. Chem. Phys. **150**, 154706 (2019).

[160] Z. Y. Wang and Y. Q. Ma, "Insights from Monte Carlo simulations on charge inversion of planar electric double layers in mixtures of asymmetric electrolytes," J. Chem. Phys. **133**, 224703 (2010).

[161] N. R. Agrawal, C. Duan, and R. Wang, "Nature of overcharging and charge inversion in electrical double layers," J. Phys. Chem. B **128**, 303–311 (2024).

[162] V. Lobaskin, B. Dünweg, M. Medebach, T. Palberg, and C. Holm, "Electrophoresis of colloidal dispersions in the low-salt regime," Phys. Rev. Lett. **98**, 176105 (2007).

[163] J. B. Freund, "Electro-osmosis in a nanometer-scale channel studied by atomistic simulation," J. Chem. Phys. **116**, 2194–2200 (2002).

[164] R. Qiao and N. R. Aluru, "Ion concentrations and velocity profiles in nanochannel electroosmotic flows," J. Chem. Phys. **118**, 4692–4701 (2003).

[165] M. Z. Bazant, M. S. Kilic, B. D. Storey, and A. Ajdari, "Towards an understanding of induced-charge electrokinetics at large applied voltages in concentrated solutions," Adv. Colloid Interface Sci. **152**, 48–88 (2009).

[166] M. Von Smoluchowski, "Contribution à la théorie de l'endosmose électrique et de quelques phénomènes corrélatifs," Bull. Akad. Sci. Krakow. **8**, 182–200 (1903).

[167] J.-P. Hansen and H. Löwen, "Effective interactions between electric double layers," Annu. Rev. Phys. Chem **51**, 209–242 (2000).

[168] J. Wu, D. Bratko, and J. M. Prausnitz, "Interaction between like-charged colloidal spheres in electrolyte solutions," Proc. Natl. Acad. Sci. U.S.A **95**, 15169–15172 (1998).

[169] V. Lobaskin and K. Qamhieh, "Effective macroion charge and stability of highly asymmetric electrolytes at various salt conditions," J. Phys. Chem. B **107**, 8022–8029 (2003).

[170] L. Guldbrand, B. Jönsson, H. Wennerström, and P. Linse, "Electrical double layer forces. A Monte Carlo study," J. Chem. Phys **80**, 2221–2228 (1984).

[171] R. J. Pellenq, J. M. Caillol, and A. Delville, "Electrostatic attraction between two charged surfaces: A (N,V,T) Monte Carlo simulation," J. Phys. Chem. B **101**, 8584–8594 (1997).

[172] N. Ise, "Like likes like: counterion-mediated attraction in macroionic and colloidal interaction," Phys. Chem. Chem. Phys. **12**, 10279–10287 (2010).

[173] E. Raspaud, M. Olvera De La Cruz, J. L. Sikorav, and F. Livolant, "Precipitation of DNA by polyamines: A polyelectrolyte behaviour," Biophys. J **74**, 381–393 (1998).

[174] M. Olvera De La Cruz, L. Belloni, M. Delsanti, J. P. Dalbiez, O. Spalla, and M. Drifford, "Precipitation of highly charged polyelectrolyte solutions in the presence of multivalent salts," J. Chem. Phys **103**, 5781–5791 (1995).

[175] G. N. Patey, "The interaction of two spherical colloidal particles in electrolyte solution. An application of the hypernetted-chain approximation," J. Chem. Phys **72**, 5763 (1980).

[176] R. Kjellander, S. Marčelja, R. M. Pashley, and J. P. Quirk, "Double-layer ion correlation forces restrict calcium-clay swelling," J. Phys. Chem. **92**, 6489–6492 (1988).

[177] R. Kjellander and S. Marčelja, "Surface interactions in simple electrolytes," J. phys. **49**, 1009–1015 (1988).

[178] I. Rouzina and V. A. Bloomfield, "Macroion attraction due to electrostatic correlation between screening counterions. 1. Mobile surface-adsorbed ions and diffuse ion cloud," J. Phys. Chem. **100**, 9977–9989 (1996).

[179] X. Chu and D. T. Wasan, "Attractive interaction between similarly charged colloidal particles," J. Colloid Interface Sci **184**, 268–278 (1996).

[180] B.-Y. Ha and A. J. Liu, "Counterion-mediated attraction between two like-charged rods," Phys. Rev. Lett. **79**, 1289–1292 (1997).

[181] J. J. Arenzon, J. F. Stilck, and Y. Levin, "Simple model for attraction between like-charged polyions," Eur. Phys. J. B **12**, 79–82 (1999).

[182] A. Diehl, M. N. Tamashiro, M. C. Barbosa, and Y. Levin, "Density-functional theory for attraction between like-charged plates," Phys. A: Stat. Mech. **274**, 433–445 (1999).

[183] A. Kudlay and M. Olvera de la Cruz, "Precipitation of oppositely charged polyelectrolytes in salt solutions," J. Chem. Phys. **120**, 404–412 (2003).

[184] A. Naji and R. R. Netz, "Attraction of like-charged macroions in the strong-coupling limit," Eur. Phys. J. E **13**, 43–59 (2004).

[185] K. Suda, A. Suematsu, and R. Akiyama, "Lateral depletion effect on two-dimensional ordering of bacteriorhodopsins in a lipid bilayer: A theoretical study based on a binary hard-disk model," J. Chem. Phys. **154** (2021).

[186] R. P. Misra, J. P. De Souza, D. Blankschtein, and M. Z. Bazant, "Theory of Surface Forces in Multivalent Electrolytes," Langmuir **35**, 11550–11565 (2019).

[187] X. Chen, E.-Q. Chen, and S. Yang, "Multivalent counterions induced attraction between dna polyelectrolytes," RSC Adv. **10**, 1890–1900 (2020).

[188] L. Šamaj and E. Trizac, "Counter-ions at charged walls: Two-dimensional systems," Eur. Phys. J. E **34**, 20 (2011).

[189] V. Lobaskin, A. Lyubartsev, and P. Linse, "Effective macroion-macroion potentials in asymmetric electrolytes," Phys. Rev. E **63**, 020401 (2001).

[190] L. Šamaj and E. Trizac, "Counterions at highly charged interfaces: From one plate to like-charge attraction," Phys. Rev. Lett. **106**, 078301 (2011).

[191] N. R. Agrawal and R. Wang, "Self-consistent description of vapor-liquid interface in ionic fluids," Phys. Rev. Lett. **129**, 228001 (2022).

[192] E. Allahyarov, G. Gompper, and H. Löwen, "Attraction between dna molecules mediated by multivalent ions," Phys. Rev. E **69**, 041904 (2004).

[193] S. C. Bukosky and W. D. Ristenpart, "Simultaneous Aggregation and Height Bifurcation of Colloidal Particles near Electrodes in Oscillatory Electric Fields," Langmuir **31**, 9742–9747 (2015).

[194] T. J. Woehl, B. J. Chen, K. L. Heatley, N. H. Talken, S. C. Bukosky, C. S. Dutcher, and W. D. Ristenpart, "Bifurcation in the steady-state height of colloidal particles near an electrode in oscillatory electric fields: Evidence for a tertiary potential minimum," Phys. Rev. X **5**, 011023 (2015).

[195] A. Ajdari, "Pumping liquids using asymmetric electrode arrays," Phys. Rev. E **61**, R45–R48 (2000).

[196] E. M. Itskovich, A. A. Kornyshev, and M. A. Vorotyntsev, "Electric current across the metal–solid electrolyte interface I. Direct current, current–voltage characteristic," Phys. Status Solidi A **39**, 229–238 (1977).

[197] G. Cevc, "Membrane electrostatics," Biochim. Biophys. Acta - Biomembr. **1031**, 311–382 (1990).

[198] M. M. Kozlov, F. Campelo, N. Liska, L. V. Chernomordik, S. J. Marrink, and H. T. McMahon, "Mechanisms shaping cell membranes," Curr. Opin. Cell Biol. **29**, 53–60 (2014).

[199] S. Zhou, "Effective electrostatic potential between two oppositely charged cylinder rods in primitive model and extended primitive model electrolytes," J. Stat. Mech. Theory Exp. **2019**, 033213 (2019).

[200] H. Aranda-Espinoza, Y. Chen, N. Dan, T. C. Lubensky, P. Nelson, L. Ramos, and D. A. Weitz, "Electrostatic repulsion of positively charged vesicles and negatively charged objects," Science **285**, 394–397 (1999).

[201] B. J. Pieters, M. B. Van Eldijk, R. J. Nolte, and J. Mecinović, "Natural supramolecular protein assemblies," Chem. Soc. Rev. **45**, 24–39 (2015).

[202] N. R. Agrawal, R. Kaur, C. Carraro, and R. Wang, "Ion correlation-driven like-charge attraction in multivalent salt solutions," J. Chem. Phys. **159**, 244905 (2023).

[203] C. Duan, N. R. Agrawal, and R. Wang, "Ion correlation induced non-monotonic height change and microphase separation of polyelectrolyte brushes," arXiv , 2404.09103 (2024).

[204] A. Mani and K. M. Wang, "Electroconvection near electrochemical interfaces: Experiments, modeling, and computation," Annu. Rev. Fluid Mech. **52**, 509–529 (2020).

[205] S. Shim, "Diffusiophoresis, diffusioosmosis, and microfluidics: Surface-flow-driven phenomena in the presence of flow," Chem. Rev. **122**, 6986–7009 (2022).

[206] B. Roux, T. Allen, S. Bernèche, and W. Im, "Theoretical and computational models of biological ion channels," Q. Rev. Biophys. **37**, 15–103 (2004).

[207] E. Flood, C. Boiteux, B. Lev, I. Vorobyov, and T. W. Allen, "Atomistic simulations of membrane ion channel conduction, gating, and modulation," Chem. Rev. **119**, 7737–7832 (2019).

[208] Y. Levin, "Charge reversal at 0 k," J. Phys.: Condens. Matter **16**, S2149–S2152 (2004).

[209] M. A. Gebbie, M. Valtiner, X. Banquy, E. T. Fox, W. A. Henderson, and J. N. Israelachvili, "Ionic liquids behave as dilute electrolyte solutions," Proc. Natl. Acad. Sci. U. S. A. **110**, 9674–9679 (2013).

[210] G. Feng, M. Chen, S. Bi, Z. A. H. Goodwin, E. B. Postnikov, N. Brilliantov, M. Urbakh, and A. A. Kornyshev, "Free and bound states of ions in ionic liquids, conductivity, and underscreening paradox," Phys. Rev. X **9**, 021024 (2019).